

# Galactic Rings Revisited. II. Dark Gaps and the Locations of Resonances in Early-to-Intermediate Type Disk Galaxies

Ronald J. Buta<sup>★</sup>

*Department of Physics & Astronomy, University of Alabama, Box 870324, Tuscaloosa, AL 35487*

Accepted XXX. Received YYY; in original form ZZZ

## ABSTRACT

Dark gaps are commonly seen in early-to-intermediate type barred galaxies having inner and outer rings or related features. In this paper, the morphologies of 54 barred and oval ringed galaxies have been examined with the goal of determining what the dark gaps are telling us about the structure and evolution of barred galaxies. The analysis is based mainly on galaxies selected from the Galaxy Zoo 2 database and the Catalogue of Southern Ringed Galaxies. The dark gaps between inner and outer rings are of interest because of their likely association with the  $L_4$  and  $L_5$  Lagrangian points that would be present in the gravitational potential of a bar or oval. Since the points are theoretically expected to lie very close to the corotation resonance (CR) of the bar pattern, the gaps provide the possibility of locating corotation in some galaxies simply by measuring the radius  $r_{gp}$  of the gap region and setting  $r_{CR}=r_{gp}$ . With the additional assumption of generally flat rotation curves, the locations of other resonances can be predicted and compared with observed morphological features. It is shown that this “gap method” provides remarkably consistent interpretations of the morphology of early-to-intermediate type barred galaxies. The paper also brings attention to cases where the dark gaps lie inside an inner ring, rather than between inner and outer rings. These may have a different origin compared to the inner/outer ring gaps.

**Key words:** galaxies: general – galaxies: structure – galaxies: spiral

## 1 INTRODUCTION

Barred galaxies are well-known not only for their ubiquity, but also for the distinctive ring morphologies they often display. The characteristic rings have been described by Buta & Combes (1996=BC96) and include nuclear (or circumnuclear) rings, inner rings, and outer rings in order of increasing linear and relative size. The rings are often made of tightly-wrapped spiral arms (“pseudorings”), and each type has its own unique set of morphological attributes.

Rings continue to be of interest in galactic studies because of their strong sensitivity to internal galaxy dynamics and because the features are likely to be intimately connected with secular evolutionary processes in galactic disks (e.g., Kormendy 1979, 2012; BC96; Knapen 2010; Buta 2012, 2013). The most popular view is that the features are related to specific orbital resonances with the pattern speed of a bar or oval. Buta (1995) used distributions of *apparent* ring axis ratios and relative bar-ring position angles for a large sample of southern galaxies to infer the *intrinsic* axis ratios and orientations of the rings, and determined that these were consistent with the predictions of barred galaxy models such

as those of Schwarz (1981, 1984a), Simkin, Su, & Schwarz (1980) and Byrd et al. (1994). Rautiainen & Salo (2000) further examined the link using more sophisticated  $n$ -body bar models. Comerón et al. (2014) carried out a similar study to Buta (1995) using deprojected mid-infrared images from the Spitzer Survey of Stellar Structure in Galaxies (S<sup>4</sup>G, Sheth et al. 2010). Although Comerón et al. confirmed that inner SB rings are generally aligned parallel to bars, these authors also identified a population of inner rings in late-type galaxies having random alignments with respect to bars.

The possible connection between galactic rings and orbital resonances in galaxies perturbed by a bar, oval, or a strong global spiral has been considered since Lindblad (1941) first proposed a density wave view of the nature of spiral structure. This view, later developed further by Lindblad (1955) and Lindblad & Lindblad (1958), highlighted the importance of the appropriately-named Lindblad resonances. The expanded density wave theory of Lin & Shu (1964) confined a self-consistent spiral between the inner and outer Lindblad resonances (ILR and OLR, respectively) of the wave, and indeed expected that the spiral could not pass through the ILR. Lin (1970) considered rings to be among the general features of galaxies to be explained by the quasi-stationary spiral structure (QSSS) hypothesis. Lin, Yuan,

<sup>★</sup> E-mail: rbuta@ua.edu

and Shu (1969) linked the “3 kpc” arm in the Milky Way to the ILR, and argued that “According to the theory, the pattern ends here as a ring.” This would likely be a ring of star formation, and indeed Lin (1970) pointed to NGC 5364 as an example of a spiral with a bright inner ring of star formation where no HII regions lie inside the ring.

Although the morphology of galactic rings has long suggested a link to resonances, studies of individual cases have been sparse, and there is clearly more to learn about these rings than can be gleaned from classification and morphology alone. The Sloan Digital Sky Survey (SDSS, Gunn et al. 1998; York et al. 2000) provides the opportunity to examine the photometric structure of large numbers of ringed galaxies with unprecedented homogeneity and effectiveness, and is the basis for most of the analysis presented in this paper. The resonance idea is also not the only theory that has been used to describe the types of ring features discussed here. The manifold theory reviewed by Athanassoula et al. (2011) and Romero-Gómez (2012) provides a remarkably different view that has had success in explaining many aspects of the morphology of rings and spirals. This theory will be discussed further in section 10.

In the first paper in this series (Buta 2017 = Paper I), the Galaxy Zoo 2 citizen science project (Willett et al. 2013; GZ2 hereafter) was used to extract a large sample of galactic rings within the SDSS footprint. Zoo volunteers used a set of buttons to classify galaxies within broad, but somewhat more finely detailed categories than had been used in Galaxy Zoo 1 (Lintott et al. 2008). One button asked if there was “anything odd” about a galaxy, and if answered “yes”, then “Is the odd feature a ring?” Using the sophisticated weighting scheme described by Willett et al. (2013), an average probability of having a ring could be derived for the 300,000 galaxies in the GZ2 sample. Restricting to those relatively nearby cases most likely to have a ring yielded 3962 galaxies, a sample comparable in size to that compiled for the Catalogue of Southern Ringed Galaxies (CSRG, Buta 1995).

The analysis in this paper is based in part on interpretations of a subset of these 3962 GZ2 galaxies in the Comprehensive de Vaucouleurs revised Hubble-Sandage (CVRHS) galaxy classification system (Buta et al. 2015). CVRHS classifications are ideally suited to studies of ring phenomena because the system recognizes in a consistent manner all normal inner, outer, and nuclear rings, pseudorings, and lenses, as well as cataclysmic rings such as those seen in ring galaxies, polar ring galaxies, inclined ring galaxies, and accretion ring galaxies. Paper I provides CVRHS classifications based on the same SDSS colour images used by the Galaxy Zoo 2 participants. One of the main results from paper I is that the types of rings that caused GZ2 participants to select “yes” for “Is the odd feature a ring” are basically identical to those selected for the CSRG. It is thus fair to intermingle the two catalogues and combine an analysis of the same kinds of galaxies in both catalogues.

This paper is focussed mainly on 50 galaxies having outer rings and pseudorings showing the distinctive morphologies thought to be characteristic of the outer Lindblad resonance, based on early barred galaxy models (Schwarz 1981; Byrd et al. 1994). These are classified as types ( $R_1$ ), ( $R'_1$ ), ( $R'_2$ ), and ( $R_1R'_2$ ) by Buta (1995) and are known as “OLR subclasses.” The primes refer to pseudorings. In pa-

per I, additional subclasses are recognized including ( $R_2$ ), ( $R_1R_2$ ), and ( $R'_1R'_2$ ). Of particular interest are the characteristic dark spaces or gaps seen in the morphology of OLR subclass galaxies. It is argued here that the location of these dark gaps/zones and their shapes favour the idea that the gaps are linked to the region of the  $L_4$ ,  $L_5$  Lagrangian points in the gravitational potential of a bar or oval. It is suggested that the surface brightness minima within the dark gaps can be used to trace the radius of the corotation resonance (CR), which can be viewed as the most important resonance governing the morphology and dynamics of a disk-shaped galaxy.

The objective of this paper is to examine the implications of using dark gaps to define the location of corotation in a sample of early-to-intermediate type barred galaxies. The theoretical basis for applying this “gap method” is described more fully in section 3. With the location of the CR determined, the radii of other resonances are predicted assuming flat rotation curves. It is shown that with this scaling, the morphology of OLR subclass galaxies is remarkably consistent and favours the idea that these are largely single pattern speed systems. The analysis also suggests that the outer 4:1 resonance plays a more important role in galaxy morphology than previously thought, which may necessitate a renaming of the “OLR subclasses” to “outer resonant subclasses.”

The paper also considers rarer cases where the dark spaces lie *inside an inner ring* rather than between inner and outer rings. If the dark spaces in these galaxies are interpreted in the same manner as for the inner/outer ring gap galaxies, then either the existence of extremely high pattern speed (“superfast”) barred galaxies would have to be acknowledged, or another mechanism for forming dark gaps that has nothing to do with Lagrangian points would have to be hypothesized. The possible role of internal extinction in making dark gaps is examined in Section 9 but considered unlikely.

A recent study by Kim et al. (2016) has independently touched on the issues of barred galaxy dark spaces, which are called “inner disc light deficits” by these authors. This paper uses numerical simulations and bar major and minor axis light profiles to examine the evolution of the inner regions of barred galaxies that might lead to these light deficits. Their Figure 1 also highlights the same two types of dark space morphologies as are discussed here, and their Figure 5 shows the same kinds of profiles as are used in Figures 5 and 10 of the present paper. The implications of Kim et al.’s work on the present study are examined in section 10.

Section 2 describes the OLR subclasses in more detail. Section 3 describes the types of “dark-spacer” morphologies recognized from the GZ2 sample, and makes the case for interpreting the dark zones in terms of the  $L_4$  and  $L_5$  Lagrangian points. Section 4 describes the processing of SDSS and other images used for this paper. Section 5 illustrates the application of the gap method to two dissimilar cases, UGC 4596 and NGC 5335, as examples. A summary of the full procedure is provided in section 6 and the results of its application to the remaining galaxies in the sample is described in section 7. Section 8 presents an analysis of the derived resonance radii, while section 9 examines the colours of the dark gaps. A discussion is presented in section 10. Conclusions are presented in section 11.

## 2 OUTER RESONANT MORPHOLOGIES

The morphological categories  $R_1$ ,  $R'_1$ ,  $R'_2$ , and  $R_1R'_2$  are singled out of the general ring population by their distinctive resemblance to model outer Lindblad resonance rings (Schwarz 1981; Buta & Crocker 1991=BC91; Buta 1995). The subclasses are believed to be tied to two families of periodic orbits near the OLR of a bar or oval (Schwarz 1981). Type  $R'_1$  (Figure 1, top) is an outer pseudoring defined by an  $\approx 180^\circ$  winding of the main spiral arms from near one end of the bar to the other, forming a characteristic figure eight pattern with “dimples” (indicated by the two horizontal arrows in Figure 1, top right) which pinch in towards the bar axis. This type may also appear in a more closed form, called  $R_1$ .

In contrast to  $R'_1$  outer pseudorings,  $R'_2$  pseudorings are defined by an  $\approx 270^\circ$  winding of the spiral arms relative to the bar (Figure 1, bottom). The defining characteristic in this case is a doubling of the spiral arms in two opposing quadrants (indicated by the pairs of arrows in Figure 1, bottom right). Although closed  $R_2$  rings are not ruled out, they would be harder to recognize than  $R_1$  without the clear arm-doubling.

Most interesting is how some galaxies show a combination of these types called  $R_1R'_2$ ,  $R'_1R'_2$ , or  $R_1R_2$ . In these cases, both families of OLR periodic orbits appear to be manifested in the morphology (Figure 1, middle). This combined ring/pseudoring morphology, which had not been predicted by Schwarz (1981), strongly supports the outer resonant interpretation of the features.

Based on a detailed analysis of CSRG galaxies, Buta (1995) concluded that  $R_1$  and  $R'_1$  rings are more abundant than  $R'_2$  rings, in the relative proportion 0.64:0.36. In the GZ2 catalogue,  $R'_1$  and  $R'_2$  are present in approximately equal numbers, with  $R_1R'_2$  being less abundant than either (paper I).

The CVRHS types of the 54 sample galaxies examined in this paper are listed in Table 1. The GZ2 sample types are from the catalogue in paper I, while those from the CSRG and a few others are from different sources, mainly BC91, the de Vaucouleurs Atlas of Galaxies (Buta et al. 2007=deVA), BC96, and a special supplementary table in RC3 (de Vaucouleurs et al. 1991). OLR subclassifications of outer rings and pseudorings are also recognized in the SDSS-based morphological catalogues of Nair & Abraham (2010) and Bailard et al. (2011), and in the mid-infrared classifications of Buta et al. (2015).

## 3 DARK GAPS IN THE LUMINOSITY DISTRIBUTION AND THE DYNAMICS OF BARRED GALAXIES

A dark-spacer is a galaxy having well-defined and organized low surface brightness regions that appear darker than their surroundings. In GZ2 galaxies, there are two main types of dark-spacer morphologies: (1) the radial zone (gap) between an inner and outer ring appears dark, either continuously or in 2-4 distinct sections [“(rR) dark-spacer”], and (2) the interior of an inner ring appears darker than outside the ring [“(r) dark-spacer”]. Only four examples of the latter type are included in the sample (NGC 4608, NGC 5335, NGC 5686,

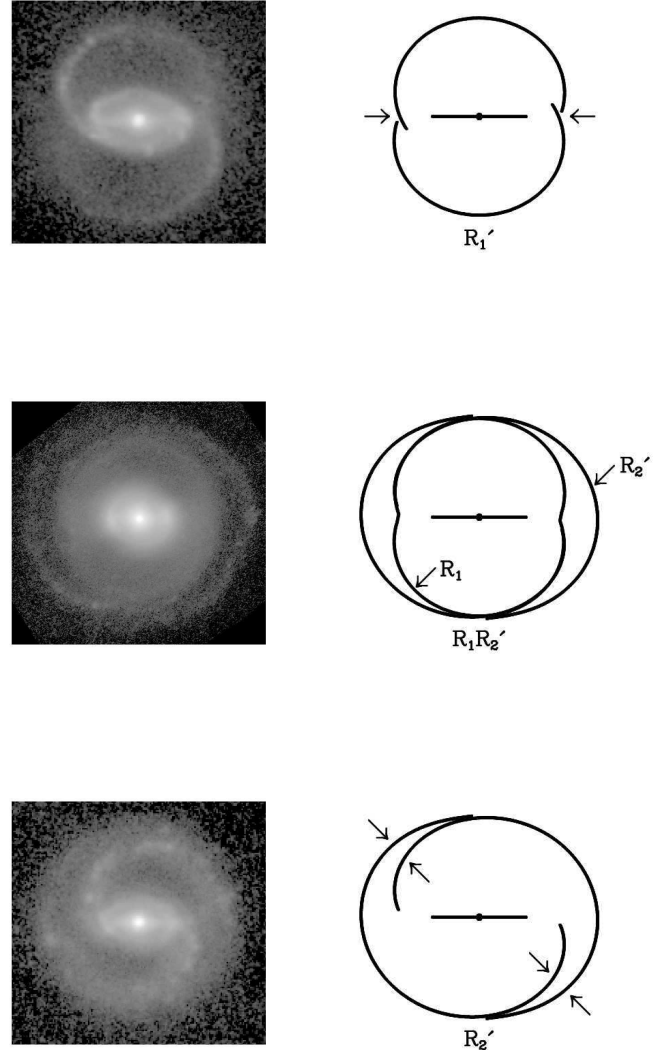


**Figure 1.** Schematics of the outer resonant ring/pseudoring morphologies. The arrows point to the characteristic features of each type shown: dimples for  $R'_1$  outer pseudorings (top right); arm-doubling in two opposing quadrants for  $R'_2$  outer pseudorings (bottom right); and the double ring/pseudoring morphology of type  $R_1R'_2$  (middle right). The left panels show an example of each type. From top to bottom these are: UGC 12646, NGC 1079, and ESO 325-28. The structure of these morphologies can be connected to two major families of OLR periodic orbits shown by Schwarz (1981). The horizontal line in each case is the theoretical orientation of the bar relative to the ring structures.

and UGC 5380). Section 5 describes both types, which have been recognized or at least alluded to in previous studies. For example, Gadotti & de Souza (2003) noted the existence of “empty regions” around some bars that stand out in a map of the residuals of the intensity distribution after subtraction of a two-dimensional decomposition model. Two examples Gadotti & de Souza noted, NGC 4608 and NGC 5701, also independently made it into our sample here. These authors consider that the bars in these galaxies may have destroyed

**Table 1.** CVRHS classifications. Col. 1: galaxy name; col. 2: source of classification; col. 3: full classification. Sources: BC91=Buta and Crocker 1991; BC96=Buta and Combes 1996; RC3=de Vaucouleurs et al. 1991, Appendix 3; deVA= Buta et al. 2007; B17=paper I; TP= this paper

| Name<br>1   | Source<br>2 | Type<br>3   | Name<br>1   | Source<br>2 | Type<br>3   |
|-------------|-------------|---|-------------|-------------|---|
| CGCG 8-10   | B17         | (R' <sub>1</sub> R' <sub>2</sub> )SAB(r)a                           | NGC 2665    | BC91        | (R' <sub>1</sub> )SAB(rs)a                                  |
| CGCG 13-75  | B17         | (R' <sub>2</sub> )SAB(r'l)ab  | NGC 2766    | B17         | (R <sub>1</sub> R' <sub>2</sub> )SAB(r)a                    |
| CGCG 65-2   | B17         | (R <sub>1</sub> )SB <sub>a</sub> (rs,bl)ab                          | NGC 3081    | BC96,deVA   | (R <sub>1</sub> R' <sub>2</sub> )SAB(r,nr,nb)0/a            |
| CGCG 67-4   | B17         | (R <sub>1</sub> L)SB <sub>a</sub> (s,bl,nl)0/a                      | NGC 3380    | B17         | (R <sub>1</sub> L)SAB(l,rs,bl)ab                            |
| CGCG 73-53  | B17         | (R <sub>1</sub> R' <sub>2</sub> )SAB <sub>a</sub> (l)0 <sup>+</sup> | NGC 4113    | B17         | (R' <sub>1</sub> )SAB(rs,nr)ab                              |
| CGCG 185-14 | B17         | (R <sub>1</sub> R' <sub>2</sub> )SAB <sub>a</sub> (rs)ab            | NGC 4608    | B17         | (RL)SB(r'l,bl)0/a   |
| CGCG 263-22 | B17         | (R' <sub>1</sub> )SAB(rs,rs)a                                       | NGC 4736    | deVA,TP     | (R)SAB(r'l,rs)ab  |
| ESO 325-28  | BC91        | (R' <sub>2</sub> )SB(r)b  | NGC 4935    | B17         | (R' <sub>2</sub> )SAB <sub>a</sub> (rs)b                    |
| ESO 365-35  | BC91,TP     | (R' <sub>2</sub> )SAB(l)0/a   | NGC 5132    | B17         | (R' <sub>1</sub> )SB(rs,bl,nr)a                             |
| ESO 426-2   | BC91        | (R <sub>1</sub> R' <sub>2</sub> )SB(r)0/a                           | NGC 5211    | B17         | (R' <sub>2</sub> )SA(rs)b                                   |
| ESO 437-33  | BC91        | (R' <sub>1</sub> R' <sub>2</sub> )SAB(rs,nr)ab                      | NGC 5335    | B17         | SB(rs,bl)ab   |
| ESO 437-67  | BC91        | (R' <sub>1</sub> )SB(rs,nr)ab                                       | NGC 5370    | B17         | (R <sub>1</sub> L)SB <sub>a</sub> (rs,bl)0/a                |
| ESO 566-24  | deVA        | (R)SB(r)b   | NGC 5686    | B17         | SB <sub>a</sub> (r,bl)0 <sup>o</sup>                        |
| ESO 575-47  | BC91        | (R' <sub>1</sub> )SB(rs)ab  | NGC 5701    | RC3,TP      | (R <sub>1</sub> R' <sub>2</sub> )SB(r'l,bl)a                |
| IC 1223     | B17         | (R')SB(rs,rs,bl)a   | NGC 6782    | deVA,BC96   | (R' <sub>1</sub> )SB(r,nr,nb)a                              |
| IC 1438     | RC3,TP      | (R <sub>1</sub> R' <sub>2</sub> )SAB(r,nr)a                         | NGC 7098    | deVA,TP     | (R <sub>1</sub> R' <sub>2</sub> )SAB <sub>a</sub> (rs,nb)ab |
| IC 2473     | B17         | (R' <sub>1</sub> )SB(r,bl)ab  | PGC 54897   | B17         | (R' <sub>1</sub> )SAB <sub>a</sub> (r'l)ab                  |
| IC 2628     | B17         | (R <sub>1</sub> R' <sub>2</sub> )SAB(l)a                            | PGC 1857116 | B17         | (R' <sub>1</sub> )SAB <sub>a</sub> (rs)a                    |
| IC 4214     | RC3         | (R <sub>1</sub> )SA(rs,nr)a   | PGC 2570478 | B17         | (R')SB(s)a  |
| MCG 6-32-24 | B17         | (R <sub>1</sub> )SAB(r)0/a  | UGC 4596    | B17         | (R <sub>1</sub> R' <sub>2</sub> )SA(rr)b                    |
| MCG 7-18-40 | B17         | (R' <sub>2</sub> )SB <sub>a</sub> (l)b                              | UGC 4771    | B17         | (R' <sub>2</sub> )SAB <sub>a</sub> (l)b                     |
| NGC 210     | deVA,TP     | (R' <sub>1</sub> R' <sub>2</sub> )SAB(l,nr)b                        | UGC 5380    | B17         | (L)SB(r,bl)0/a  |
| NGC 1079    | RC3,TP      | (R <sub>1</sub> R' <sub>2</sub> )SAB <sub>a</sub> (r'l,bl)a         | UGC 5885    | B17         | (R' <sub>1</sub> )SAB <sub>a</sub> (rs,nr)ab                |
| NGC 1291    | RC3,deVA    | (R <sub>1</sub> R' <sub>2</sub> )SAB(l,nb)0/a                       | UGC 9418    | B17         | (R' <sub>2</sub> )SAB <sub>a</sub> (r'l)b                   |
| NGC 1326    | BC96        | (R <sub>1</sub> )SAB(r,nr)0/a                                       | UGC 10168   | B17         | (R <sub>1</sub> R' <sub>2</sub> )SAB <sub>a</sub> (r'l)a    |
| NGC 1398    | B95,TP      | (R',R <sub>1</sub> )SB(rs)ab  | UGC 10712   | B17         | (R <sub>1</sub> R' <sub>2</sub> )SAB(r'l)b                  |
| NGC 1433    | BC96,TP     | (R' <sub>1</sub> )SB(p,rs,nr,nb)ab                                  | UGC 12646   | RC3         | (R' <sub>1</sub> )SB(r)ab                                   |

their disks through a secular evolutionary process. Based on mid-infrared images from the S<sup>4</sup>G, Laurikainen et al. (2013) note “Sometimes an inner ring is seen mainly because of dark space around the sides of the bar.” In some cases the dark regions have a distinct banana shape, especially if an average background is subtracted (as in the disk-subtracted image for NGC 3081 from Buta & Purcell 1998). The critical issue with dark-spacer morphology is that the dark-looking regions are *not* a result of dust extinction but are in many cases plateaus or genuine minima in surface brightness. This is examined further in section 9.

The consistency in the appearance of the dark regions in (rR) dark-spacers suggests a link to dynamics rather than dust extinction. Here we make the following hypothesis: the dark gaps between the inner and outer rings of OLR subclass galaxies are tied to the  $L_4$  and  $L_5$  Lagrangian points in the gravitational potential of a bar or bar-like oval. These points lie on a line perpendicular to the perturbation major axis and, unlike the  $L_1$ ,  $L_2$  points, may be stable or unstable (Binney & Tremaine 1987=BT87, 2008=BT08).  $L_1$  and  $L_2$  may lie at a different radius from  $L_4$  and  $L_5$ , and a circle through each pair of points defines what BT87 call the “region of corotation.”

A useful potential for analytically deriving the location of these points is the logarithmic potential  $\Phi_L$  (equation 3.103 of BT08), which is defined by an axis ratio  $q$ , a core radius  $R_c$ , and which has a rotation curve which rises quickly near  $R_c$  and then asymptotes to  $v = v_0 = \text{constant}$  at radii  $r \gg R_c$ . The bar pattern speed is  $\Omega_p$  such that the radius

of corotation  $r_{CR} = v_0/\Omega_p$ . If the bar is oriented horizontally, then the  $L_4$  and  $L_5$  points lie at  $y_L = \pm r_{CR} \sqrt{1 - q^2 \left(\frac{R_c}{r_{CR}}\right)^2}$  (BT08, equation 3.131). This equation shows that if  $q^2 \left(\frac{R_c}{r_{CR}}\right)^2 \ll 1$ , then  $r_{CR} = |y_L|$ . Such a situation would occur if the rotation curves of OLR subclass galaxies are generally flat, and if  $r_{CR} \gg R_c$ . From known rotation curves of several outer resonant subclass cases [NGC 1433 (Buta et al. 2001); NGC 3081 (Buta & Purcell 1998); NGC 6782 (Lin et al. 2008); IC 4214 (Salo et al. 1999); ESO 566–24 (Rautiainen et al. 2004)], and from the analysis in this paper, these conditions are likely to be satisfied.

The logarithmic potential is mostly an ovally-distorted disk (meaning there is a flattening in the planar potential which affects the entire disk, not just a part of the disk). Athanassoula (1992) examined the locations of  $L_1$ ,  $L_2$ ,  $L_4$ , and  $L_5$  for a more realistic model barred galaxy having a bulge, a disk, and a Ferrers ellipsoid bar. She found the radius of the  $L_4$  and  $L_5$  points to be slightly inside the radius of the  $L_1$  and  $L_2$  points, and that  $r_{CR}$  was between these radii.

An important question is, on what basis should we identify the dark zones in (rR) dark-spacers as being linked to Lagrangian points? Why should the area of such points be dark? The reason could be linked to the stability of orbits around these points. According to Pfenniger (1990; see also Contopoulos and Papayannopoulos 1980), “if the  $L_4$  and  $L_5$  points are stable, they must trap high-energy orbits ... while if unstable, they generate chaotic motion around them, which might tend to depopulate these regions.” Pre-



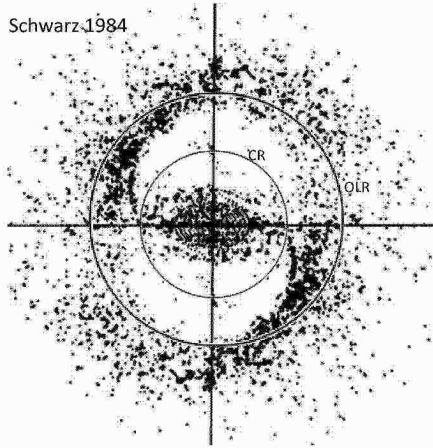


**Figure 2.** A test-particle frame from a simulation (Schwarz 1984a, Figure 6) of a strongly-barred disk galaxy showing the depopulation of the broad zones around the  $L_4$  and  $L_5$  Lagrangian points. The CR and OLR circles for the model are superposed. Reprinted with the permission of the author.

sumably, depopulation could lead to a lower surface mass density around these points, and therefore a lower surface brightness.

In the case of stability, the high energy orbits are the long period orbits (LPOs; Contopoulos & Grosbol 1989), which tend to be banana-shaped orbits representing “a slow tangential wallowing in the weak non-axisymmetric component of  $\Phi_L$ ” (BT87). Stars would be trapped in these orbits circulating around the  $L_4$  and  $L_5$  points as seen from the reference frame rotating with the bar. Additionally, short-period orbits (SPOs; Contopoulos & Grosbol 1989) would also be circulating around these points with smaller excursions (BT87).

Numerical simulations have shown that the  $L_4$  and  $L_5$  points can be unstable in the presence of a strong bisymmetric perturbation. In his early test-particle models of barred galaxies, Schwarz (1981) noted how the region between CR and OLR became increasingly depopulated as bar strength increased. He states: “As the bar strength is increased, the region becomes larger and takes on the same appearance as the holes which are common in almost all SB galaxies – the spaces in the ‘ $\theta$ ’ shape.” Contopoulos (1981) noted that this happens because all the periodic orbits between CR and OLR become unstable, and therefore are unable to trap any non-periodic orbits around them.

Schwarz (1984a) shows a strong bar model where the regions around  $L_4$  and  $L_5$  are unstable for the cases of a collisionless disk and a disk with test-particle clouds allowed to collide. In both cases, the area around these points is strongly depleted. Figure 2 selects the frame of the collisional case after 10 bar rotations. Superposed on the particle plot are circles having the radius of CR and OLR. This shows how CR lies roughly in the middle of the gap between the inner structure and an  $R_1'$  outer pseudoring. Similar results were found by Byrd et al. (1994) and Salo et al. (1999).

We interpret the dark spaces in ( $rR$ ) dark-spacer galaxies to be the locations of such unstable  $L_4$  and  $L_5$  points, and that the average radius  $r_{gp}$  of the minima of surface

brightness or residual intensity in these regions, based on parabolic fits to bar minor axis profiles, traces the location of corotation, i. e.,  $r_{gp} = r_{CR}$ . We also expect that the more unstable the orbits around  $L_4$  and  $L_5$  are, the darker and better-defined the gaps will be. This can be seen comparing the models of Schwarz (1981) with those of Schwarz (1984a), where the bar strength for the former models was only half that used in Figures 4 and 6 of Schwarz (1984a).

#### 4 SURFACE PHOTOMETRY

For each GZ2 galaxy selected for photometry, the SDSS DAS Query form was used to download Data Release 7 (DR7; Abazajian et al. 2009) fpC images in the filters  $u$ ,  $g$ ,  $r$ , and  $i$ . Although SDSS  $u$ -band images are not as well-exposed as the  $gri$  images,  $u$  is still an extremely useful filter for examining star formation in a galaxy, which is very relevant to galactic rings. From these images, a smaller area (512x512 or 256x256 pixels) centred on the galaxy was extracted. Each filter image was then cleaned of contaminating foreground and background objects using IRAF routine IMEDIT. The background was subtracted by fitting a plane to either pixels in a specified border region or pixels in specified squares in the corners of the images. The fitted plane was then subtracted from both the cleaned and uncleaned images. Filter alignments were made using IRAF routine IMALIGN.

The above procedure was applied mainly to objects that had only a single field to download. In some cases, 2-3 fields were available, allowing an improved signal-to-noise ratio for surface photometry at fainter light levels. To combine multiple images after background subtractions, IRAF routines IMALIGN, IMSHIFT and, where needed, IMCOMBINE, were used to remove small shifts and rotations.

Image calibrations were taken from the tsfield fits tables that accompany the fpC images. The zero points were derived as

$$zp = -(a + kx) + 2.5 \log(A_{pix}t)$$

where  $a$  is the zero point for 1 second,  $k$  is the extinction coefficient,  $x$  is the airmass, and  $A_{pix}$  is the area of a single pixel in square arcsec, where 1 pix =  $0''.396$ . The uniform exposure time for all SDSS images is  $t = 53.907$  seconds.

The IRAF routine ELLIPSE was used to fit ellipses to the isophotes of each galaxy. The main goal of these fits was an estimate of the orientation parameters of the disks, meaning the inclination through the mean projected disk axis ratio  $q_d$  and the line of nodes through the photometric major axis position angle  $\phi_d$ . These are compiled in Table 2. To insure that the faintest outer isophotes are used for this purpose, the ellipse fits were generally performed on 2x2 or 4x4 block-averaged images. With estimates of the orientation parameters of the galaxies, the IRAF routine IMLINTRAN was used to deproject the galaxies. All images illustrated in this paper are deprojected and largely cleaned of foreground stars except where noted.

For each GZ2 galaxy, we derived (a)  $ugri$  azimuthally-averaged luminosity profiles; (b) the deprojected radius and position angle of the bar or oval; (c) luminosity profiles parallel and perpendicular to the bar axis; and (d) relative Fourier amplitudes and phases. No photometric decompositions of

the luminosity profiles are presented in this paper. The emphasis instead is on profile shapes, feature contrasts, and morphology.

The GZ2 subsample accounts for 33 of the sample of 54 galaxies. The remaining 21 cases are mainly from the CSRG and involve Johnson-Cousins *BVI* CCD images from the author's private image library. Many of these images were illustrated in the study of BC91. Although most of these images are of high quality, they lack the homogeneity of the SDSS images. Zero points were determined either from published *BVI* photoelectric photometry (e.g., Buta and Crocker 1992; Buta et al. 1995; Buta and Williams 1995), or standard star transformations, with image scales ranging from  $0''.19$  to  $0''.6 \text{ pix}^{-1}$ . The final cleaned and background-subtracted *BVI* images were used to derive the same kinds of profiles and parameters as were derived for the GZ2 galaxies.

We focus first on two GZ2 examples with exceptionally dark but very regular spaces flanking a bar or oval, to show the photometric information we have derived for each galaxy, and to illustrate our procedure for deriving  $r_{gp}$ .

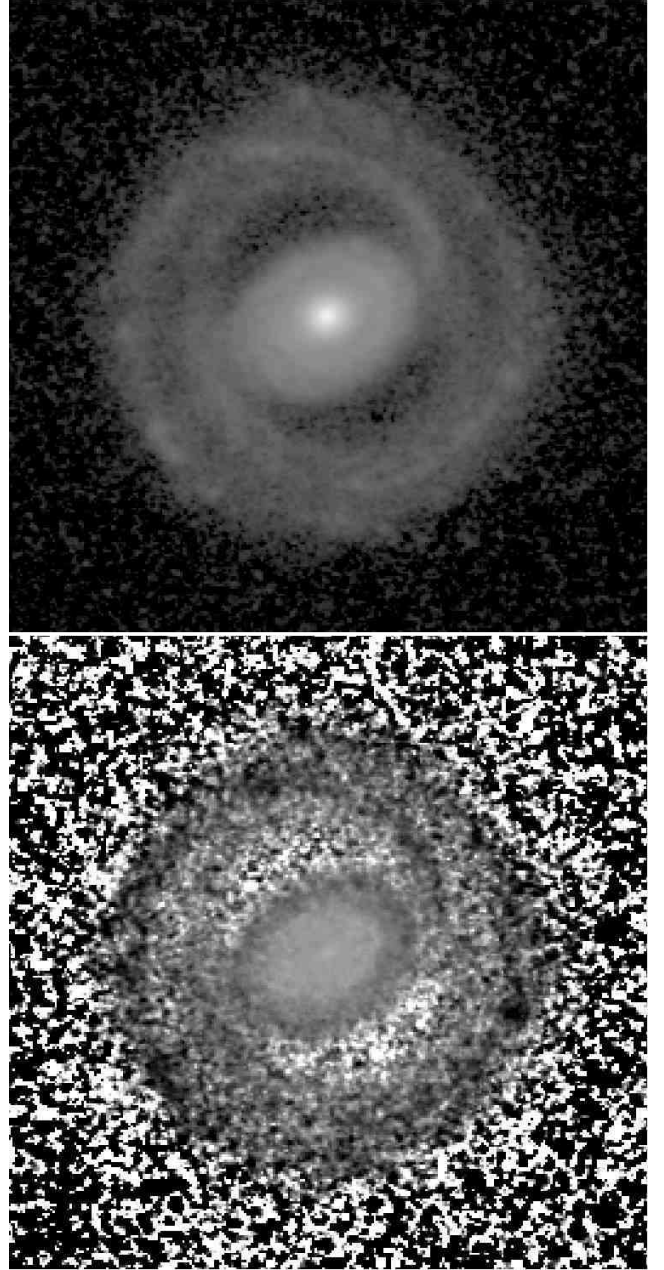
## 5 TWO EXAMPLES

### 5.1 UGC 4596

UGC 4596 (Figure 3) is a strong (rR) dark-spacer having four well-defined ring or pseudoring features. Its CVRHS classification is  $(R_1R'_2)SA(rr)b$ . Although there is no conventional bar, the two inner rings lie in the outer regions of a massive oval, which must act as the bar of the system. Based on ellipse fits to *gri* isophotes in the radius range  $31''$ – $48''$ , the average disk axis ratio and major axis position angle are  $0.855 \pm 0.014$  and  $130^\circ.1 \pm 3^\circ.8$ , respectively. These parameters were used to derive azimuthally-averaged luminosity profiles and to deproject the *ugri* images.

Figure 4 shows the *ugri* azimuthally-averaged surface brightness and colour index profiles of UGC 4596. The galaxy is an exceptional example where a strong  $R_1R'_2$  morphology causes two clear “bumps” in the outer plateau. The profiles in all four filters show a steep decline beyond the second outer bump. Figure 5 compares *g*- and *i*-band profiles along axes parallel and perpendicular to the deprojected oval. The vertical lines show the radial positions where the difference between the two profiles is maximum (see also section 10). In the *g*-band, this difference amounts to 2.03 mag, but in the *i*-band, the difference amounts to only 1.32 mag. The parallel and perpendicular profiles show that the gaps in UGC 4596 are redder than much of the rest of the disk. The explanation for this is likely to be that recent star formation extends over much of the disk (as seen in both the *g*–*i* colour index map and in the azimuthally-averaged *u*-band surface brightness profile), except for the gaps which are red most likely because their light is dominated by older stars (section 9). The redness of the gaps is still present but subdued in the azimuthally-averaged colour index profiles.

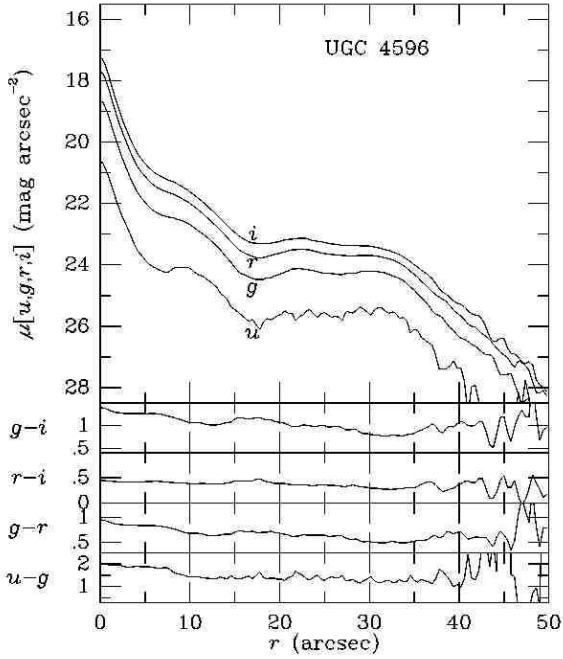
Figure 6 shows relative  $m = 2, 4$ , and 6 Fourier intensity amplitudes and the phase of the  $m = 2$  component as a function of radius, based on the deprojected *i*-band image. In spite of the lack of an apparent bar, the maximum  $m = 2$  relative amplitude is  $A_2 = 0.66$ , with much lower  $m = 4$  and 6 amplitudes.



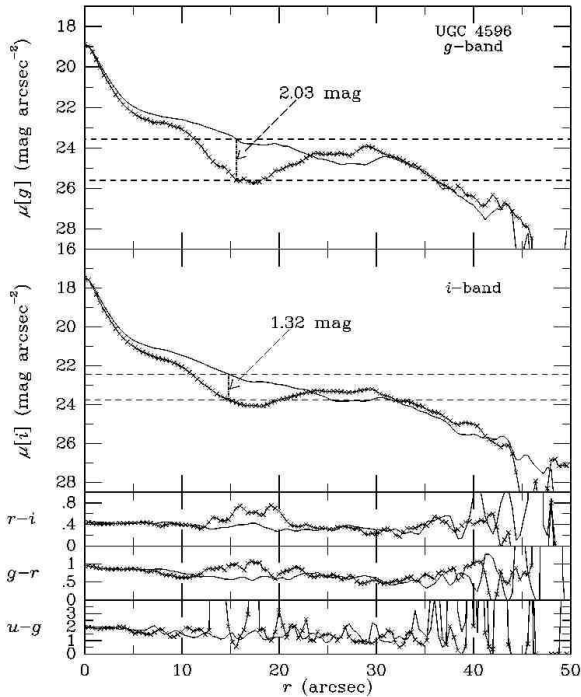
**Figure 3.** Deprojected *g*-band image (top) and *g*–*i* colour index map of UGC 4596, type  $(R_1R'_2)SA(rr)b$ . Both images are in units of  $\text{mag arcsec}^{-2}$ . The *g*–*i* colour index map is coded such that redder features are light and bluer features are dark. The field shown is  $1'.69$  arcminutes square.

Figure 7 shows how  $r_{gp}$  is derived. In this case, for each filter we fitted a parabola to the surface brightnesses in the gap region. An uncertainty was assigned to the derived radius using the standard deviation of the data points around the fitted parabola. This gave  $r_{gp} = 17''.2 \pm 1''.2$ ,  $17''.5 \pm 1''.1$ , and  $17''.5 \pm 0''.8$ , for the *g*, *r*, and *i* filters, respectively. The final value,  $\langle r_{gp} \rangle = 17''.4 \pm 0''.6$ , is a weighted average over the three filters using the estimated uncertainties  $\sigma_g = 1''.2$ ,  $\sigma_r = 1''.1$ , and  $\sigma_i = 0''.8$  as weights  $w = 1/\sigma^2$ .

The above procedure to get  $r_{gp}$  works well for UGC 4596 because its oval minor axis gaps are dark and well-defined.



**Figure 4.** Azimuthally-averaged *ugri* surface brightness and colour index profiles of UGC 4596



**Figure 5.** Profiles of UGC 4596 parallel (solid curve) and perpendicular (solid curve marked with crosses) to the deprojected massive oval

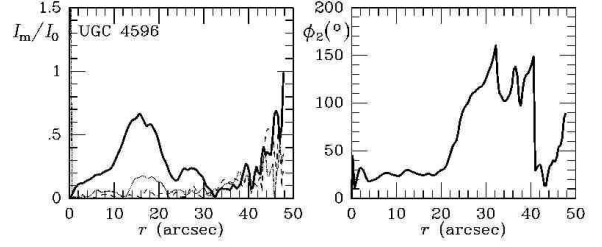


**Figure 6.** Fourier intensity analysis of UGC 4596: (left) *i*-band relative Fourier amplitudes as a function of radius, for  $m = 2$  (solid curve), 4 (dotted curve), and 6 (dashed curve); (right) Phase of  $m = 2$  Fourier component. This phase is in the arbitrary units of the deprojected images.

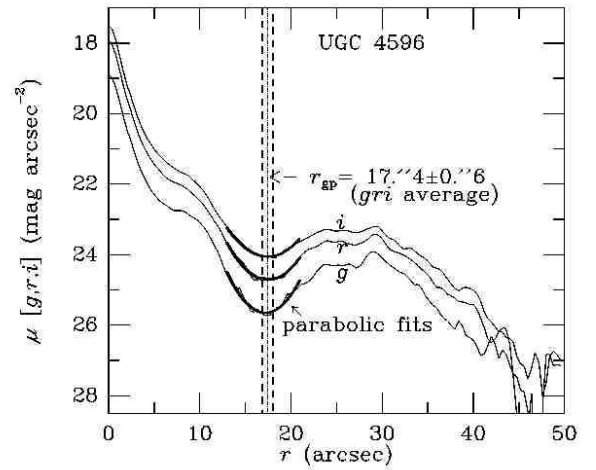


**Figure 7.** Illustration of the method used to determine  $r_{gp}$ , the radius in the gap region where the surface intensity along the bar minor axis is a minimum, for UGC 4596 and other similar examples of (rR) dark-spacers where the gaps are especially well-defined. The parabolic fits to the  $\mu$  values in these regions are indicated by the darker points.

In some cases, however, the apparent gaps are subtle, such that in profiles the gap minima are difficult to measure reliably in a regular surface brightness profile. In such cases, we subtracted a heavily median-smoothed background from the intensity images and fitted parabolas to the intensity residuals in the enhanced gap region. This is illustrated and discussed further in the Appendix.

## 5.2 NGC 5335

NGC 5335 provides a remarkable contrast to UGC 4596. The dark zones in UGC 4596 are located in the transition region between the galaxy's multiple rings, while the dark zones in NGC 5335 lie inside a conspicuous inner ring, the only ring in that system. NGC 5335 is the strongest (r) dark-spacer in the GZ2 catalog and it suggests that dark spaces inside inner rings are not merely contrast effects but are actually dynamical in nature.

Figures 8– 11 show deprojected images, azimuthally-



averaged profiles, bar major and minor axis profiles, and relative Fourier intensity profiles for NGC 5335. The CVRHS classification of the galaxy is SB(rs,bl)ab, and the deprojection is based on a disk axis ratio of 0.856 and a disk major axis position angle of  $109^\circ.4$ . Both the  $g$ -band image and the  $g-i$  colour index map show a considerable amount of noise in the dark spaces. The colour index maps are in fact so noisy in this region that it is difficult to decide what the colours of the dark spaces are. This is definitively clarified by the azimuthally-averaged colour index profiles, all of which are nearly constant across the bar region. *The colours of the dark spaces are nearly identical to those of the bar.* This suggests that a dynamical effect associated with the bar has caused the dark spaces.

The deprojected bar major and minor axis profiles in Figure 10 show that both the  $g$ - and  $i$ -band surface brightnesses of NGC 5335 are about 2.4 mag fainter at radii of  $15''$ – $16''$  compared to the bar axis, and that the surface brightness inside the ring is not achieved again until a radius of nearly  $59''$  in  $g$  and  $53''$  in  $i$ . The shapes of the  $u-g$ ,  $g-r$ , and  $r-i$  colour index profiles is nearly identical along the two axes, except for the increased noise level between  $10''$  and  $20''$  due to the drastic difference in surface brightness between the bar major and minor axis profiles in this range.

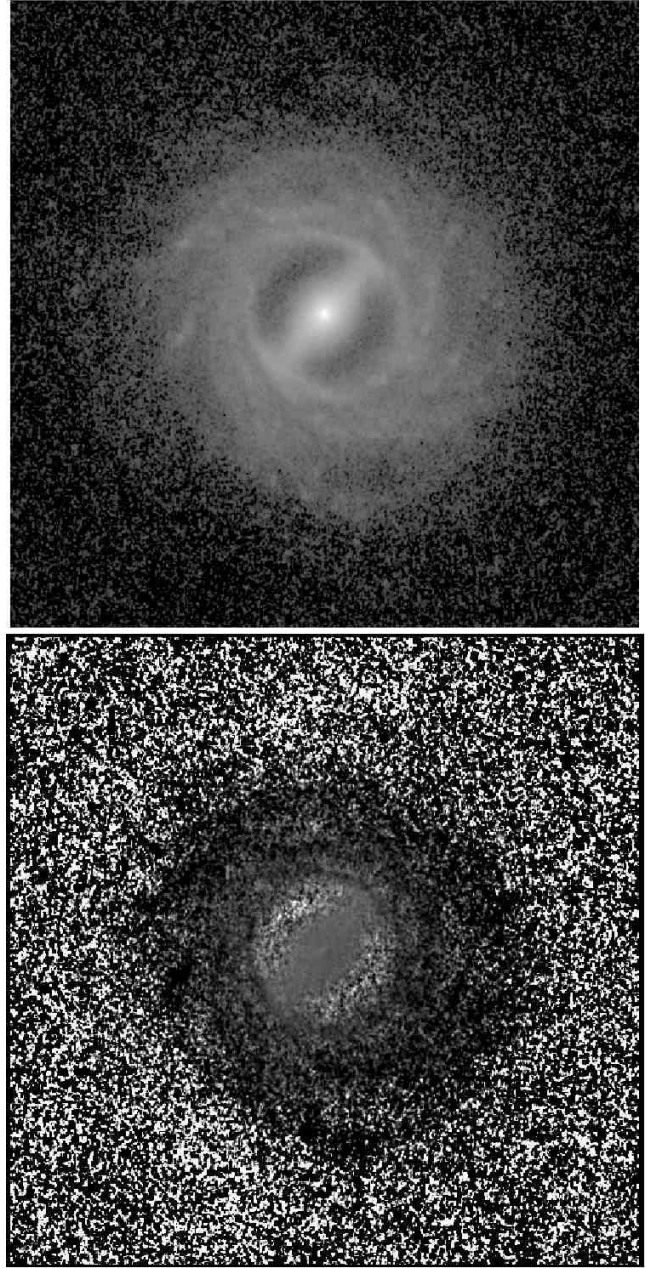
The inner ring of NGC 5335 is also somewhat unusual. The average inner ring in an SB galaxy is intrinsically oval (mean axis ratio =  $0.81 \pm 0.06$ ) and is aligned parallel to the bar (Buta 1995). The visually-mapped deprojected inner ring in NGC 5335 has an axis ratio of 0.893 and is oriented  $82^\circ$  to the deprojected bar axis. Thus, the inner ring of NGC 5335 is not a typical SB inner ring. When combined with a multi-armed outer spiral pattern as opposed to an outer ring or pseudoring, then NGC 5335 becomes even more atypical. The relative Fourier intensity profiles of NGC 5335 also show that  $A_2$  is 0.95, making the bar one of the strongest in our sample.

Figure 12 shows the derivation of  $r_{gp}$  for NGC 5335. As for UGC 4596, we fitted a parabola to the surface brightnesses in the dark gap region in each filter and then computed a weighted average. The resulting value,  $r_{gp} = 17''.1 \pm 1''.0$ , has a larger relative error than UGC 4596 because of the high noise level in the gap zone.

## 6 APPLICATION OF THE GAP METHOD TO THE SAMPLE

The gap method is a photometric/morphological approach to locating the corotation resonance. Other more sophisticated methods have been proposed and applied for the same purpose, including the Tremaine & Weinberg (1984) photometric/kinematic method, the Canzian (1993) geometric phase method, the potential-density phase shift method (Zhang & Buta 2007), and most recently the streaming phase reversal (kinematic) method (Font et al. 2011, 2014). In the remainder of this paper, the method is applied to a total sample of 50 (rR) dark-spacer galaxies and 4 (r) dark-spacer cases. The steps are:

1. Clean images of foreground and background objects, and then subtract off the sky level as a plane using IRAF routine IMSURFIT.
2. Using IRAF routine ELLIPSE, fit ellipses to faint outer



**Figure 8.** Deprojected  $g$ -band image (top) and  $g-i$  colour index map of NGC 5335, type SB(rs,bl)ab. The field shown is  $3'.38$  arcminutes square.

isophotes to get reliable orientation parameters, including the mean disk axis ratio  $q_d$  and the mean disk position angle  $\phi_d$ . The adopted values are listed in Table 2, including for the CSRG sample. The typical uncertainty in  $q_d$  is  $\pm 0.010$  or less, while that for  $\phi_d$  can be  $2^\circ$ – $20^\circ$  depending on how round the isophotes are.

3. For each galaxy, derive azimuthally-averaged luminosity and colour index profiles within the fixed ellipses defined by  $q_d$  and  $\phi_d$ , in order to highlight the homogeneity of the average structure of each galaxy. These profiles are shown in Figures 4 and 9 for UGC 4596 and NGC 5335, respectively, and for the remaining 52 sample galaxies in Figure 21 (see Appendix). Exponential extrapolations of the surface



**Table 2.** Orientation parameters and filters used for deriving  $r_{gp}$ . Col. 1: galaxy name; cols. 2 and 3: mean disk axis ratio and major axis position angle (degrees) based on ellipse fits to faint outer isophotes; col. 4: filters and method used to derive  $r_{gp}$ . “gri” means that  $r_{gp}$  is based on parabolic fits to surface brightnesses (mag arcsec<sup>-2</sup>) in SDSS filters *gri*. “intgri” means that  $r_{gp}$  is based on parabolic fits to residual intensities in *gri* after subtraction of a heavily median-smoothed background.

| Name        | $q_d$ | $\phi_d$ | filters | Name        | $q_d$ | $\phi_d$ | filters |
|-------------|-------|----------|---------|-------------|-------|----------|---------|
| 1           | 2     | 3        | 4       | 1           | 2     | 3        | 4       |
| CGCG 8-10   | 0.783 | 159.2    | gri     | NGC 2665    | 0.767 | 121.1    | BVI     |
| CGCG 13-75  | 0.870 | 108.6    | gri     | NGC 2766    | 0.403 | 127.0    | intgri  |
| CGCG 65-2   | 0.602 | 74.2     | intgri  | NGC 3081    | 0.850 | 89.0     | BI      |
| CGCG 67-4   | 0.792 | 39.7     | intgri  | NGC 3380    | 0.963 | 62.9     | intgri  |
| CGCG 73-53  | 0.825 | 98.3     | intgri  | NGC 4113    | 0.830 | 133.1    | gri     |
| CGCG 185-14 | 0.478 | 28.2     | intgri  | NGC 4608    | 0.873 | 110.5    | intgri  |
| CGCG 263-22 | 0.927 | 75.4     | intgri  | NGC 4736    | 0.865 | 116.0    | gi      |
| ESO 325-28  | 0.974 | 128.3    | intBVI  | NGC 4935    | 0.949 | 84.9     | intgri  |
| ESO 365-35  | 0.751 | 155.2    | BVI     | NGC 5132    | 0.800 | 102.8    | gri     |
| ESO 426-2   | 0.906 | 64.7     | BVI     | NGC 5211    | 0.772 | 175.0    | gri     |
| ESO 437-33  | 0.718 | 0.9      | BVI     | NGC 5335    | 0.856 | 109.4    | gri     |
| ESO 437-67  | 0.883 | 5.0      | BVI     | NGC 5370    | 0.885 | 76.1     | intgri  |
| ESO 566-24  | 0.749 | 69.1     | BVI     | NGC 5686    | 0.922 | 29.4     | intgri  |
| ESO 575-47  | 0.811 | 111.5    | BVI     | NGC 5701    | 0.960 | 49.2     | gri     |
| IC 1223     | 0.761 | 0.4      | intgri  | NGC 6782    | 0.894 | 34.9     | BVI     |
| IC 1438     | 0.898 | 143.1    | intBVI  | NGC 7098    | 0.557 | 70.1     | BVI     |
| IC 2473     | 0.739 | 32.3     | gri     | PGC 54897   | 0.847 | 84.2     | gri     |
| IC 2628     | 0.911 | 151.8    | intgri  | PGC 1857116 | 0.549 | 36.4     | intgri  |
| IC 4214     | 0.616 | 170.5    | BVI     | PGC 2570478 | 0.701 | 91.3     | intgri  |
| MCG 6-32-24 | 0.743 | 141.0    | intgri  | UGC 4596    | 0.855 | 130.1    | gri     |
| MCG 7-18-40 | 0.938 | 179.9    | intgri  | UGC 4771    | 0.634 | 30.2     | gri     |
| NGC 210     | 0.690 | 159.0    | intR    | UGC 5380    | 0.668 | 147.9    | intgri  |
| NGC 1079    | 0.592 | 81.3     | intBVI  | UGC 5885    | 0.332 | 136.5    | gri     |
| NGC 1291    | 1.000 | 0.0      | BVRI    | UGC 9418    | 0.972 | 54.4     | gri     |
| NGC 1326    | 0.750 | 73.4     | intBVI  | UGC 10168   | 0.725 | 167.5    | gri     |
| NGC 1398    | 0.702 | 95.9     | intBVI  | UGC 10712   | 0.960 | 84.2     | gri     |
| NGC 1433    | 0.850 | 17.0     | BI      | UGC 12646   | 0.909 | 28.0     | BV      |

brightness profiles were used to estimate total magnitudes and colour indices for the galaxies. These are provided in Table 3 for the GZ2 galaxies and Table 4 for the CSRG and other sample galaxies.

The last three lines in Table 3 compare the derived total *g*-band magnitudes, *g*–*i*, *g*–*r*, and *r*–*i* colours with the SDSS pipeline “modelMag” values described by Stoughton et al. (2002). In general, the Table 3 values are brighter than the modelMag values by an amount that increases with decreasing wavelength. The last three lines in Table 4 similarly compare the derived *BVI* parameters with published values based on mean growth curve fits to photoelectric multi-aperture photometry. Since this was the same photometry used to calibrate most of the non-GZ2 images, the good agreement on the colours is not surprising. However, the *B<sub>T</sub>* magnitudes in Table 4 are 0.08 mag fainter than the published values, most likely because of the different extrapolations used.

Also listed in both tables are the absolute magnitudes of the galaxies, ranging from –18.7 to –21.5 for the *g*-band and –19.2 to –21.3 for the *B*-band, in each case typical of intermediate to high mass disk galaxies. Distance moduli are taken from the NASA/IPAC Extragalactic Database (NED). The colours of the galaxies are further examined in section 9.

4. Deproject the galaxies using  $q_d$  and  $\phi_d$  with IRAF routine IMLINTRAN. From the deprojected *i*-band image of each GZ2 galaxy, and the deprojected *I*-band image of each CSRG

galaxy and other non-GZ2 cases, derive relative Fourier intensity amplitudes  $I_m/I_0$  as a function of radius. These profiles are shown in Figures 6 and 11 for UGC 4596 and NGC 5335, respectively, and for the remaining 52 galaxies in Figure 22 (see Appendix). Relative maximum amplitudes  $A_m = (I_m/I_0)_{\max}$  for  $m = 2, 4$ , and 6 are compiled in Table 5. The perturbation strengths range from relatively weak ( $A_2 = 0.25$ , CGCG 185-14) to very strong ( $A_2 = 1.39$ , NGC 4113).

5. Convert deprojected images into units of mag/arcsec<sup>2</sup>, allowing the morphology of each galaxy to be displayed as well as for making colour index maps.

6. Derive the deprojected radius  $a_{bar}$  and position angle  $\theta_{bar}$  of the bar/oval in the *i*-band (GZ2 galaxies) or the *I*-band (non-GZ2 galaxies, if available), using IRAF/STSDAS routine ELLIPSE. In most cases the radius of the bar isophote of maximum ellipticity provided a reasonable estimate of this parameter.

7. Visually map the ring, pseudoring, or spiral features in the *g*-band (GZ2 galaxies) or *B*-band (CSRG and other galaxies). The mappings (Figure 13) were made using IRAF routine TVMARK, and usually more than one mapping was needed to get the best representation of a feature. The major axis radius  $a$ , the minor axis radius  $b$ , and the major axis position angle  $\theta_f$  of each feature were derived from least squares ellipse fits to the mapped points.

8. Derive luminosity profiles along and perpendicular to the

**Table 3.** Integrated magnitudes and colours of 33 GZ2 sample galaxies plus 1 non-GZ2 case. Col. 1: galaxy name; cols. 2-6: integrated magnitude and colours, obtained by extrapolation of an exponential beyond the outer regions; col. 7: distance modulus with respect to the galactic standard of rest (GSR), from the NASA/IPAC Extragalactic Database (NED); col. 8: absolute g-band magnitude corrected for galactic extinction from NED. The last three lines compare the derived magnitudes and colours with SDSS DR9 “modelMag” values (Stoughton et al. 2002) for the same galaxies, extracted through NED.

| Name<br>1             | $g_T$<br>2 | $(u-g)_T$<br>3 | $(g-i)_T$<br>4 | $(g-r)_T$<br>5 | $(r-i)_T$<br>6 | $m-M$<br>7 | $M_g^o$<br>8 |
|-----------------------|------------|----------------|----------------|----------------|----------------|------------|--------------|
| CGCG 8-10             | 15.24      | 1.74           | 1.25           | 0.80           | 0.45           | 35.91      | −20.8        |
| CGCG 13-75            | 14.62      | 1.47           | 1.09           | 0.70           | 0.40           | 35.07      | −20.6        |
| CGCG 65-2             | 15.05      | 1.31           | 1.01           | 0.66           | 0.35           | 34.36      | −19.5        |
| CGCG 67-4             | 15.43      | 1.36           | 1.04           | 0.65           | 0.39           | 36.20      | −20.8        |
| CGCG 73-53            | 14.96      | ....           | 1.14           | 0.75           | 0.40           | 34.90      | −20.0        |
| CGCG 185-14           | 14.87      | 1.47           | 1.05           | 0.68           | 0.37           | 35.13      | −20.3        |
| CGCG 263-22           | 14.96      | 1.58           | 1.31           | 0.87           | 0.45           | 35.61      | −20.8        |
| MCG 6-32-24           | 15.21      | 1.38           | 1.03           | 0.67           | 0.36           | 35.37      | −20.3        |
| MCG 7-18-40           | 15.86      | 1.41           | 1.10           | 0.71           | 0.40           | 37.24      | −21.5        |
| IC 1223               | 14.66      | 1.66           | 1.25           | 0.83           | 0.42           | 35.48      | −20.9        |
| IC 2628               | 15.20      | 1.46           | 1.08           | 0.70           | 0.38           | 36.18      | −21.1        |
| IC 2473               | 13.96      | 1.37           | 1.01           | 0.65           | 0.36           | 35.21      | −21.3        |
| NGC 2766              | 14.10      | 1.44           | 1.11           | 0.71           | 0.39           | 33.77      | −19.8        |
| NGC 3380              | 13.02      | 1.31           | 0.99           | 0.62           | 0.37           | 31.66      | −18.7        |
| NGC 4113              | 14.35      | 1.15           | 0.80           | 0.51           | 0.29           | 35.19      | −20.9        |
| NGC 4608              | 11.46      | 1.75           | 1.15           | 0.74           | 0.41           | 31.95      | −20.5        |
| NGC 4736 <sup>a</sup> | 8.32       | ....           | 1.04           | ....           | ....           | 28.47      | −20.2        |
| NGC 4935              | 13.69      | 1.28           | 0.95           | 0.60           | 0.35           | 34.71      | −21.1        |
| NGC 5132              | 13.52      | 1.56           | 1.21           | 0.79           | 0.42           | 35.00      | −21.6        |
| NGC 5211              | 13.01      | 1.42           | 1.10           | 0.73           | 0.37           | 33.50      | −20.6        |
| NGC 5335              | 13.09      | 1.27           | 1.00           | 0.64           | 0.36           | 34.00      | −21.0        |
| NGC 5370              | 13.49      | 1.66           | 1.13           | 0.73           | 0.40           | 33.20      | −19.8        |
| NGC 5686              | 14.62      | 1.64           | 1.12           | 0.72           | 0.40           | 33.83      | −19.2        |
| NGC 5701              | 11.43      | 1.55           | 1.12           | 0.69           | 0.43           | 31.58      | −20.3        |
| PGC 54897             | 14.59      | 1.31           | 1.00           | 0.64           | 0.36           | 34.94      | −20.5        |
| PGC 1857116           | 15.65      | 1.33           | 1.09           | 0.70           | 0.39           | .....      | .....        |
| PGC 2570478           | 15.57      | 1.83           | 1.29           | 0.88           | 0.41           | .....      | .....        |
| UGC 4596              | 14.67      | 1.54           | 1.10           | 0.72           | 0.39           | 35.54      | −21.0        |
| UGC 4771              | 14.67      | 1.61           | 1.13           | 0.74           | 0.39           | 35.88      | −21.3        |
| UGC 5380              | 14.39      | ....           | 1.19           | 0.78           | 0.41           | 34.60      | −20.4        |
| UGC 5885              | 14.91      | 1.35           | 1.12           | 0.71           | 0.41           | 35.59      | −20.8        |
| UGC 9418              | 14.45      | 1.54           | 1.05           | 0.68           | 0.37           | 35.66      | −21.3        |
| UGC 10168             | 13.71      | 1.74           | 1.22           | 0.80           | 0.42           | 34.64      | −21.0        |
| UGC 10712             | 15.01      | 1.49           | 1.05           | 0.68           | 0.37           | 35.89      | −21.0        |
| <mag,col-modelMag>    | −0.24      | −0.27          | −0.11          | −0.10          | −0.01          | .....      | .....        |
| $\sigma_1$            | 0.18       | 0.16           | 0.08           | 0.05           | 0.04           | .....      | .....        |
| $N$                   | 32         | 30             | 32             | 32             | 32             |            |              |

<sup>a</sup>not part of GZ2 subsample

bar/oval axis. Depending on how strong the dark gaps are, fit a parabola either to gap surface brightnesses  $\mu$  or to residual intensities  $\Delta$  after subtraction of a heavily median-smoothed version of the image, to get  $r_{gp}(j)$  in filter  $j$ . Do this for as many filters available as possible, and then take the weighted average of  $r_{gp}(j)$  from all the applicable filters. For GZ2 galaxies, all  $r_{gp}$  are based on *gri* images. For non-GZ2 galaxies, most are based on *BVI* images, with a few having only *BV* (UGC 12646), *BI* (NGC 1433, NGC 3081), or a red continuum image (NGC 210). Table 2 lists the filters used for each sample galaxy and the method (surface brightness versus residual intensities) used to get  $r_{gp}(j)$ .

9. set  $r_{CR} = \langle r_{gp} \rangle$

The determination of  $r_{CR}$  allows us to locate other important resonances if we can make a reasonable assumption about the shapes of the rotation curves of typical OLR sub-

class galaxies. Based on detailed studies of five well-observed examples: NGC 1433 (Buta et al. 2001), NGC 3081 (Buta & Purcell 1998; Buta et al. 2004), IC 4214 (Buta et al. 1999; Salo et al. 1999), ESO 566–24 (Rautiainen et al. (2004), and NGC 6782 (Lin et al. 2008), the most reasonable choice is that of a flat rotation curve. In this case, we can predict the locations of the likely major ring-forming resonances as (Athanasoulas et al. 1982):

$$\begin{aligned}
 r_{OLR} &= 1.71 \, r_{CR} \\
 r_{ILR} &= r_{OLR}/5.83 \\
 r_{OAR} &= r_{OLR}/1.26 \\
 r_{IAR} &= r_{OLR}/2.64
 \end{aligned}$$

In the vicinity of the inner Lindblad resonance (ILR), the flat rotation curve assumption is unlikely to be correct for most of our sample galaxies, and for this reason the dis-

**Table 4.** Integrated magnitudes and colours of 19 CSRG and other galaxies. Col. 1: galaxy name; cols. 2-5: integrated magnitude and colours, obtained by extrapolation of an exponential beyond the outer regions; col. 6: distance modulus with respect to the galactic standard of rest (GSR), from NED; col. 7: absolute  $B$ -band magnitude corrected for galactic extinction from NED. The last three lines compare the derived magnitudes and colours with published values from Buta & Crocker (1992) and RC3.

| Name<br>1     | $B_T$<br>2 | $(B-V)_T$<br>3 | $(V-I)_T$<br>4 | $(B-I)_T$<br>5 | $m-M$<br>6 | $M_B^o$<br>7 |
|---------------|------------|----------------|----------------|----------------|------------|--------------|
| ESO 325-28    | 14.17      | 0.77           | 1.06           | 1.83           | 34.95      | -21.1        |
| ESO 365-35    | 14.95      | 1.06           | 1.25           | 2.31           | 35.05      | -20.4        |
| ESO 426-2     | 14.42      | 0.95           | 1.21           | 2.16           | 34.76      | -20.5        |
| ESO 437-33    | 13.77      | 0.77           | 1.11           | 1.88           | 33.78      | -20.2        |
| ESO 437-67    | 13.54      | 0.83           | 1.18           | 2.01           | 33.06      | -19.8        |
| ESO 566-24    | 13.65      | 0.69           | 1.08           | 1.77           | 33.28      | -19.8        |
| ESO 575-47    | 13.78      | 0.88           | 1.21           | 2.09           | 34.07      | -20.6        |
| IC 1438       | 13.02      | 0.82           | 1.15           | 1.97           | 32.82      | -19.9        |
| IC 4214       | 12.30      | 0.88           | 1.15           | 2.03           | 32.36      | -20.3        |
| NGC 1079      | 12.26      | 0.91           | 1.10           | 2.01           | 31.38      | -19.2        |
| NGC 1291      | 9.51       | 0.88           | 1.09           | 1.97           | 29.95      | -20.5        |
| NGC 1326      | 11.47      | 0.86           | 1.14           | 2.00           | 31.15      | -19.7        |
| NGC 1398      | 10.61      | 0.92           | 1.22           | 2.14           | 31.24      | -20.7        |
| NGC 1433      | 10.79      | ....           | ....           | 1.82           | 30.52      | -19.8        |
| NGC 2665      | 13.02      | 0.70           | 1.11           | 1.81           | 31.61      | -19.0        |
| NGC 3081      | 12.88      | ....           | ....           | 2.06           | 32.38      | -19.7        |
| NGC 6782      | 12.83      | 0.89           | 1.22           | 2.12           | 33.61      | -21.0        |
| NGC 7098      | 12.44      | 1.02           | 1.18           | 2.20           | 32.45      | -20.3        |
| UGC 12646     | 14.15      | 0.83           | ....           | ....           | 35.26      | -21.3        |
| <mag,col-pub> | 0.08       | 0.01           | 0.00           | 0.01           | .....      | .....        |
| $\sigma_1$    | 0.09       | 0.03           | 0.04           | 0.06           | .....      | .....        |
| $N$           | 17         | 15             | 12             | 13             | .....      | .....        |

**Table 5.** Maximum relative Fourier amplitudes for terms  $m = 2, 4$ , and  $6$  for all 54 sample galaxies. Col. 1: name of galaxy; cols. 2-4: maximum relative Fourier intensity amplitude for  $m = 2, 4$ , and  $6$ , respectively. For the GZ2 galaxies, the amplitudes are based on the  $i$ -band, while for the non-GZ2 galaxies, the amplitudes are based on the  $I$ -band except for UGC 12646, where the  $V$ -band was used instead.

| Galaxy<br>1 | $A_2$<br>2 | $A_4$<br>3 | $A_6$<br>4 | Galaxy<br>1 | $A_2$<br>2 | $A_4$<br>3 | $A_6$<br>4 | Galaxy<br>1 | $A_2$<br>2 | $A_4$<br>3 | $A_6$<br>4 |
|-------------|------------|------------|------------|-------------|------------|------------|------------|-------------|------------|------------|------------|
| CGCG 8-10   | 0.70       | 0.29       | 0.14       | IC 4214     | 0.63       | 0.23       | 0.08       | NGC 5211    | 0.41       | 0.15       | 0.05       |
| CGCG 13-75  | 0.54       | 0.18       | 0.08       | MCG 6-32-24 | 0.61       | 0.16       | 0.05       | NGC 5335    | 0.95       | 0.55       | 0.33       |
| CGCG 65-2   | 0.62       | 0.34       | 0.18       | MCG 7-18-40 | 0.48       | 0.16       | 0.07       | NGC 5370    | 0.64       | 0.33       | 0.17       |
| CGCG 67-4   | 0.98       | 0.56       | 0.31       | NGC 210     | 0.53       | 0.14       | 0.06       | NGC 5686    | 0.31       | 0.17       | 0.10       |
| CGCG 73-53  | 0.42       | 0.11       | 0.04       | NGC 1079    | 0.65       | 0.26       | 0.12       | NGC 5701    | 0.49       | 0.20       | 0.09       |
| CGCG 185-14 | 0.25       | 0.07       | 0.04       | NGC 1291    | 0.48       | 0.16       | 0.07       | NGC 6782    | 0.64       | 0.28       | 0.13       |
| CGCG 263-22 | 0.56       | 0.10       | 0.07       | NGC 1326    | 0.62       | 0.21       | 0.09       | NGC 7098    | 0.68       | 0.23       | 0.11       |
| ESO 325-28  | 0.78       | 0.31       | 0.17       | NGC 1398    | 0.46       | 0.23       | 0.16       | PGC 54897   | 0.96       | 0.49       | 0.22       |
| ESO 365-35  | 0.51       | 0.12       | 0.10       | NGC 1433    | 0.97       | 0.40       | 0.21       | PGC 1857116 | 0.99       | 0.46       | 0.26       |
| ESO 426-2   | 0.74       | 0.36       | 0.23       | NGC 2665    | 1.06       | 0.62       | 0.45       | PGC 2570478 | 0.47       | 0.20       | 0.06       |
| ESO 437-33  | 0.60       | 0.19       | 0.07       | NGC 2766    | 0.40       | 0.18       | 0.11       | UGC 4596    | 0.66       | 0.18       | 0.07       |
| ESO 437-67  | 1.17       | 0.53       | 0.24       | NGC 3081    | 0.69       | 0.24       | 0.11       | UGC 4771    | 0.68       | 0.32       | 0.15       |
| ESO 566-24  | 0.61       | 0.36       | 0.22       | NGC 3380    | 0.81       | 0.34       | 0.15       | UGC 5380    | 0.74       | 0.43       | 0.25       |
| ESO 575-47  | 0.91       | 0.40       | 0.27       | NGC 4113    | 1.39       | 0.83       | 0.52       | UGC 5885    | 1.13       | 0.60       | 0.37       |
| IC 1223     | 0.48       | 0.20       | 0.10       | NGC 4608    | 0.71       | 0.43       | 0.27       | UGC 9418    | 0.72       | 0.30       | 0.15       |
| IC 1438     | 0.67       | 0.29       | 0.13       | NGC 4736    | 0.44       | 0.09       | 0.03       | UGC 10168   | 0.49       | 0.15       | 0.06       |
| IC 2473     | 1.04       | 0.49       | 0.26       | NGC 4935    | 0.57       | 0.21       | 0.09       | UGC 10712   | 0.71       | 0.28       | 0.10       |
| IC 2628     | 0.36       | 0.11       | 0.05       | NGC 5132    | 1.07       | 0.48       | 0.21       | UGC 12646   | 1.16       | 0.61       | 0.29       |

cussion will focus on the other major resonances. Table 6 summarizes the results for the 50 (rR) dark-spacers in the GZ2/CSRG sample, while Table 7 does the same for the 4 (r) dark-spacers in the sample. In both tables, the gap CR radii are in col. 2, the predicted radii of the inner and outer 4:1 resonances are in cols. 3 and 4, and the predicted radii of

the inner and outer Lindblad resonances are in cols. 5 and 6.

**Table 6.** Gap Corotation, Predicted Resonance, and Relative Bar Radii for (rR) dark-spacers. Col. 1: galaxy name; col. 2: radius of corotation resonance based on gap method; cols. 3-6: inferred radii of other resonances, assuming a flat rotation curve; col. 7: deprojected radius of bar based on ellipse of maximum ellipticity; cols. 8-9: relative radius of bar to corotation and inner 4:1 resonance radii, respectively.

| Name<br>1   | $r_{CR}$<br>2   | $r_{I4R}$<br>3 | $r_{O4R}$<br>4 | $r_{ILR}$<br>5 | $r_{OLR}$<br>6 | $a_{bar}$<br>7 | $a_{bar}/r_{CR}$<br>8 | $a_{bar}/r_{I4R}$<br>9 |
|-------------|-----------------|----------------|----------------|----------------|----------------|----------------|-----------------------|------------------------|
| CGCG 8-10   | $21.9 \pm 1.6$  | 14.2           | 29.7           | 6.4            | 37.4           | 12.7           | 0.58                  | 0.90                   |
| CGCG 13-75  | $12.6 \pm 0.6$  | 8.2            | 17.1           | 3.7            | 21.5           | 7.9            | 0.63                  | 0.97                   |
| CGCG 65-2   | $12.9 \pm 0.7$  | 8.3            | 17.5           | 3.8            | 22.0           | 9.5            | 0.74                  | 1.14                   |
| CGCG 67-4   | $13.5 \pm 0.9$  | 8.7            | 18.3           | 4.0            | 23.1           | 8.9            | 0.66                  | 1.02                   |
| CGCG 73-53  | $10.3 \pm 0.3$  | 6.7            | 14.0           | 3.0            | 17.6           | 5.9            | 0.57                  | 0.88                   |
| CGCG 185-14 | $11.4 \pm 0.2$  | 7.4            | 15.5           | 3.3            | 19.5           | 7.1            | 0.62                  | 0.96                   |
| CGCG 263-22 | $22.0 \pm 1.2$  | 14.2           | 29.7           | 6.4            | 37.5           | 23.0           | 1.05                  | 1.62                   |
| ESO 325-28  | $17.6 \pm 1.3$  | 11.4           | 23.8           | 5.1            | 30.0           | 13.1           | 0.75                  | 1.15                   |
| ESO 365-35  | $20.8 \pm 1.2$  | 13.4           | 28.1           | 6.1            | 35.5           | 12.6           | 0.61                  | 0.94                   |
| ESO 426-2   | $22.1 \pm 1.1$  | 14.3           | 30.0           | 6.5            | 37.8           | 18.1           | 0.82                  | 1.27                   |
| ESO 437-33  | $23.7 \pm 1.0$  | 15.3           | 32.1           | 6.9            | 40.4           | 13.7           | 0.58                  | 0.90                   |
| ESO 437-67  | $54.0 \pm 3.7$  | 34.9           | 73.1           | 15.8           | 92.1           | 37.2           | 0.69                  | 1.07                   |
| ESO 566-24  | $26.6 \pm 0.9$  | 17.2           | 36.0           | 7.8            | 45.3           | 19.4           | 0.73                  | 1.13                   |
| ESO 575-47  | $36.8 \pm 2.3$  | 23.8           | 49.8           | 10.8           | 62.7           | 31.2           | 0.85                  | 1.31                   |
| IC 1223     | $22.5 \pm 1.0$  | 14.5           | 30.5           | 6.6            | 38.4           | 12.7           | 0.56                  | 0.87                   |
| IC 1438     | $33.3 \pm 2.2$  | 21.6           | 45.2           | 9.8            | 56.9           | 21.8           | 0.65                  | 1.01                   |
| IC 2473     | $35.2 \pm 2.0$  | 22.8           | 47.7           | 10.3           | 60.1           | 24.1           | 0.68                  | 1.06                   |
| IC 2628     | $10.0 \pm 0.4$  | 6.5            | 13.6           | 2.9            | 17.1           | 5.5            | 0.55                  | 0.85                   |
| IC 4214     | $46.2 \pm 2.0$  | 29.9           | 62.6           | 13.5           | 78.8           | 44.4           | 0.96                  | 1.49                   |
| MCG 6-32-24 | $11.7 \pm 0.7$  | 7.5            | 15.8           | 3.4            | 19.9           | 5.0            | 0.43                  | 0.66                   |
| MCG 7-18-40 | $7.6 \pm 0.5$   | 4.9            | 10.3           | 2.2            | 12.9           | 5.2            | 0.69                  | 1.06                   |
| NGC 210     | $60.2 \pm 5.5$  | 38.9           | 81.6           | 17.6           | 102.8          | 33.8           | 0.56                  | 0.87                   |
| NGC 1079    | $83.5 \pm 6.5$  | 54.0           | 113.1          | 24.4           | 142.5          | 42.0           | 0.50                  | 0.78                   |
| NGC 1291    | $175.0 \pm 6.3$ | 113.1          | 237.0          | 51.2           | 298.7          | 90.5           | 0.52                  | 0.80                   |
| NGC 1326    | $62.5 \pm 4.9$  | 40.4           | 84.7           | 18.3           | 106.7          | 39.9           | 0.64                  | 0.99                   |
| NGC 1398    | $88.7 \pm 3.8$  | 57.3           | 120.1          | 26.0           | 151.4          | 54.8           | 0.62                  | 0.96                   |
| NGC 1433    | $132.8 \pm 8.4$ | 85.9           | 180.0          | 38.9           | 226.7          | 85.3           | 0.64                  | 0.99                   |
| NGC 2665    | $42.4 \pm 2.7$  | 27.4           | 57.5           | 12.4           | 72.4           | 33.4           | 0.79                  | 1.22                   |
| NGC 2766    | $21.3 \pm 0.4$  | 13.8           | 28.8           | 6.2            | 36.3           | 18.2           | 0.85                  | 1.32                   |
| NGC 3081    | $59.1 \pm 2.7$  | 38.2           | 80.1           | 17.3           | 100.9          | 25.7           | 0.43                  | 0.67                   |
| NGC 3380    | $31.6 \pm 2.3$  | 20.4           | 42.8           | 9.2            | 53.9           | 20.0           | 0.63                  | 0.98                   |
| NGC 4113    | $24.1 \pm 2.1$  | 15.6           | 32.6           | 7.1            | 41.1           | 18.4           | 0.76                  | 1.18                   |
| NGC 4736    | $246.1 \pm 8.6$ | 159.1          | 333.4          | 72.1           | 420.1          | 141.8          | 0.58                  | 0.89                   |
| NGC 4935    | $17.0 \pm 0.9$  | 11.0           | 23.1           | 5.0            | 29.1           | 9.5            | 0.56                  | 0.86                   |
| NGC 5132    | $42.0 \pm 2.3$  | 27.2           | 57.0           | 12.3           | 71.8           | 32.5           | 0.77                  | 1.20                   |
| NGC 5211    | $34.9 \pm 1.8$  | 22.6           | 47.3           | 10.2           | 59.6           | 18.8           | 0.54                  | 0.83                   |
| NGC 5370    | $31.9 \pm 1.6$  | 20.6           | 43.2           | 9.3            | 54.5           | 18.2           | 0.57                  | 0.88                   |
| NGC 5701    | $69.7 \pm 3.0$  | 45.1           | 94.4           | 20.4           | 118.9          | 39.0           | 0.56                  | 0.87                   |
| NGC 6782    | $44.5 \pm 2.7$  | 28.7           | 60.2           | 13.0           | 75.9           | 26.1           | 0.59                  | 0.91                   |
| NGC 7098    | $86.8 \pm 3.2$  | 56.1           | 117.6          | 25.4           | 148.2          | 48.3           | 0.56                  | 0.86                   |
| PGC 54897   | $17.7 \pm 1.2$  | 11.4           | 24.0           | 5.2            | 30.2           | 9.9            | 0.56                  | 0.87                   |
| PGC1857116  | $15.3 \pm 0.7$  | 9.9            | 20.8           | 4.5            | 26.2           | 10.7           | 0.70                  | 1.08                   |
| PGC2570478  | $13.6 \pm 0.9$  | 8.8            | 18.5           | 4.0            | 23.3           | 8.5            | 0.62                  | 0.96                   |
| UGC 4596    | $17.4 \pm 0.6$  | 11.3           | 23.6           | 5.1            | 29.8           | 9.5            | 0.54                  | 0.84                   |
| UGC 4771    | $18.2 \pm 1.0$  | 11.8           | 24.6           | 5.3            | 31.1           | 11.1           | 0.61                  | 0.94                   |
| UGC 5885    | $25.7 \pm 2.0$  | 16.6           | 34.9           | 7.5            | 43.9           | 22.2           | 0.86                  | 1.33                   |
| UGC 9418    | $14.7 \pm 0.9$  | 9.5            | 19.9           | 4.3            | 25.1           | 9.9            | 0.67                  | 1.04                   |
| UGC10168    | $27.4 \pm 1.3$  | 17.7           | 37.2           | 8.0            | 46.9           | 16.0           | 0.58                  | 0.90                   |
| UGC10712    | $11.5 \pm 0.6$  | 7.4            | 15.6           | 3.4            | 19.6           | 7.5            | 0.65                  | 1.01                   |
| UGC12646    | $32.2 \pm 3.9$  | 20.8           | 43.6           | 9.4            | 55.0           | 23.4           | 0.73                  | 1.12                   |
| means       | .....           | .....          | .....          | .....          | .....          | .....          | 0.65                  | 1.01                   |
| mean error  | .....           | .....          | .....          | .....          | .....          | .....          | 0.02                  | 0.03                   |
| $\sigma_1$  | .....           | .....          | .....          | .....          | .....          | .....          | 0.12                  | 0.19                   |
| $N$         | .....           | .....          | .....          | .....          | .....          | .....          | 50                    | 50                     |



**Table 7.** Gap Corotation, Predicted Resonance, and Relative Bar Radii for (r) dark-spacers. Col. 1: galaxy name; col. 2: radius of corotation resonance based on gap method; cols. 3-6: inferred radii of other resonances, assuming a flat rotation curve; col. 7: deprojected radius of bar based on ellipse of maximum ellipticity; cols. 8-9: relative radius of bar to corotation and inner 4:1 resonance radii, respectively.

| Name       | $r_{CR}$       | $r_{I4R}$ | $r_{O4R}$ | $r_{ILR}$ | $r_{OLR}$ | $a_{bar}$ | $a_{bar}/r_{CR}$ | $a_{bar}/r_{I4R}$ |
|------------|----------------|-----------|-----------|-----------|-----------|-----------|------------------|-------------------|
| 1          | 2              | 3         | 4         | 5         | 6         | 7         | 8                | 9                 |
| NGC 4608   | $36.8 \pm 1.4$ | 23.8      | 49.9      | 10.8      | 62.9      | 50.3      | 1.37             | 2.11              |
| NGC 5335   | $17.1 \pm 1.0$ | 11.1      | 23.2      | 5.0       | 29.2      | 24.2      | 1.41             | 2.19              |
| NGC 5686   | $4.7 \pm 0.1$  | 3.0       | 6.4       | 1.4       | 8.0       | 5.9       | 1.25             | 1.94              |
| UGC 5380   | $8.5 \pm 0.3$  | 5.5       | 11.5      | 2.5       | 14.5      | 14.7      | 1.73             | 2.67              |
| means      | .....          | .....     | .....     | .....     | .....     | .....     | 1.44             | 2.23              |
| mean error | .....          | .....     | .....     | .....     | .....     | .....     | 0.10             | 0.16              |
| $\sigma_1$ | .....          | .....     | .....     | .....     | .....     | .....     | 0.20             | 0.31              |
| $N$        | .....          | .....     | .....     | .....     | .....     | .....     | 4                | 4                 |

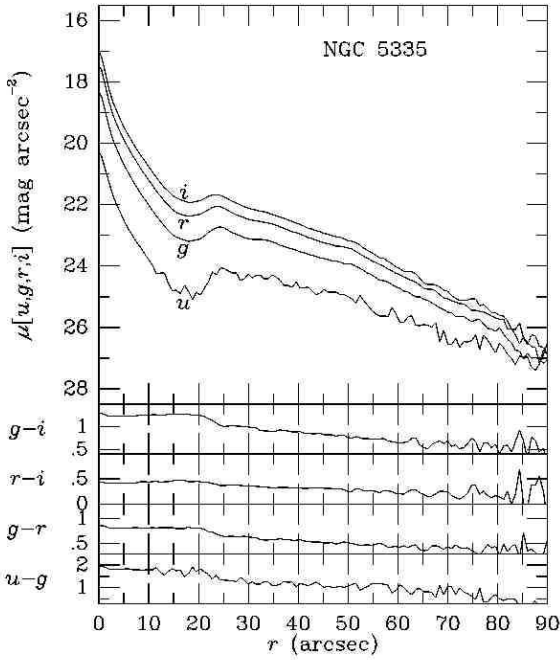


**Figure 9.** Azimuthally-averaged *ugri* surface brightness and colour index profiles of NGC 5335

## 7 DESCRIPTION OF INDIVIDUAL GALAXIES

The way the morphology of the sample galaxies is compared with the predicted locations of resonances from the gap method is in the form of schematic graphs where details of the ring and pseudoring features have been visually mapped (Figure 13). These schematics are useful because they highlight the spiral and dimpling characteristics of many outer rings; the spiral, cusping, and arc-ansae characteristics of many inner rings/lenses; and the limited extent of bars inside inner rings/lenses. In these schematics, partial ellipse

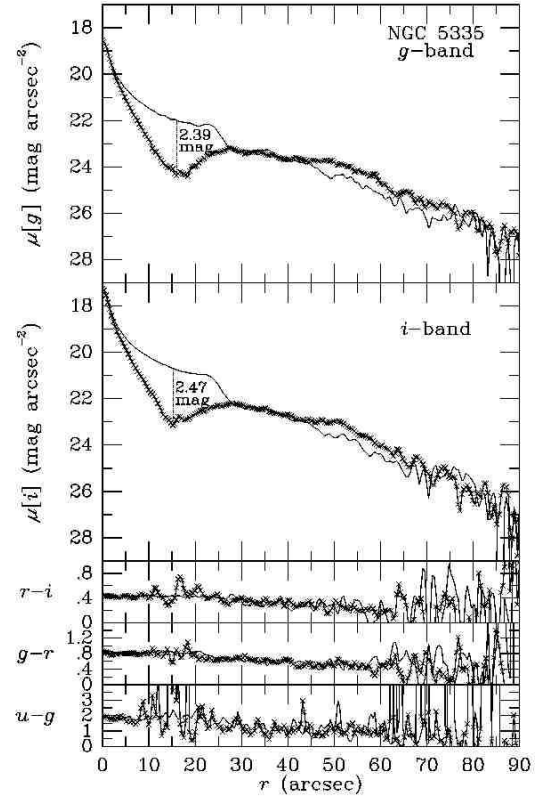


**Figure 10.** Profiles of NGC 5335 parallel (solid curve) and perpendicular (solid curve marked with crosses) to the deprojected bar axis

fits were used to map shapes where possible. For the outer arms that make up  $R_2'$  components, the radius  $r$  versus position angle  $\theta$  along each arm was fitted with a polynomial usually of order 5-7. Also, for each schematic, the bar has been rotated to a horizontal position for ease of comparison with other galaxies in the sample.

Figure 13 shows two frames per galaxy: The left frame is the *g* or *B*-band image (in units of  $\text{mag arcsec}^{-2}$ ) with the location of the CR (white circle) superposed, while the

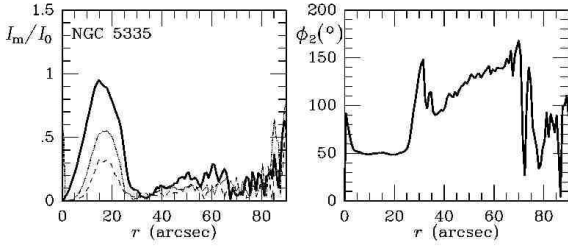


**Figure 11.** Fourier intensity analysis of NGC 5335: (left)  $i$ -band relative Fourier amplitudes as a function of radius, for  $m = 2$  (solid curve), 4 (dotted curve), and 6 (dashed curve); (right) Phase of  $m = 2$  Fourier component

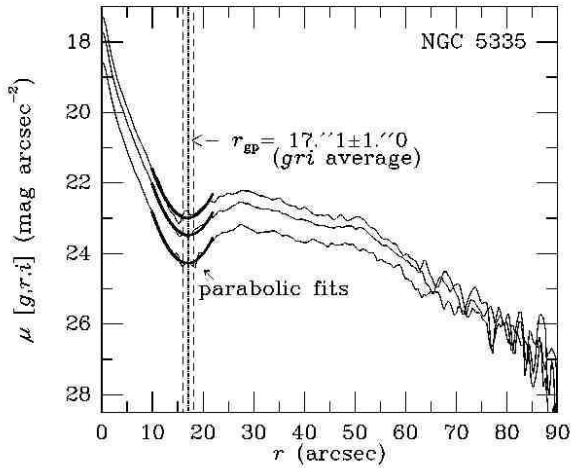


**Figure 12.** Illustration of the method used to determine  $r_{gp}$  for NGC 5335 and other similar examples of (r) dark-spacers.

right frame is the schematic showing the visually-mapped features which include all of the ring, lens, and bar features recognized in the CVRHS classification. The assumed locations of the  $L_4$  and  $L_5$  points are indicated. In a few cases, larger filled circles or ovals indicate the locations of strong bar ansae (as, for example, in the schematic of NGC 7098). Strong bars (mostly type SB in Table 1) are indicated by the horizontal solid lines, while weaker bars (mostly type SAB in Table 1) are indicated by light or dashed lines. No horizontal lines are used for the apparently weakest bars (mostly types SA and SAB in Table 1). Ovals are indicated in some cases by arc ansae. Also, bar-ring misalignment is highlighted in a few cases, such as NGC 5132 and IC 2473. In these cases, the bar line is not horizontal.

CGCG 8-10 - The galaxy is of type  $(R'_1 R'_2) \text{SAB}(r)a$ , where the SAB refers to arc ansae around the major axis of the inner ring, which are prominent in both  $g$  and  $i$ . This galaxy also displays a dichotomy first noted by Buta (1995) for IC 1438: the  $R_1$  component is a prominent dimpled feature in the  $i$ -band, while the  $R'_2$  component is most prominent in the  $g$ -band. This suggests that the  $R_1$  component formed first and left behind a mostly stellar remnant. Colour index maps show that most of the recent star formation in the galaxy is in the bright ansae arcs of the inner ring and the

bright opposing quadrants of the  $R'_2$  pseudoring. The gap corotation method places the  $R_1$  component between  $r_{CR}$  and  $r_{OLR}$ , and in fact the feature straddles  $r_{OAR}$ . The  $R'_2$  reaches but still is largely inside  $r_{OLR}$ , while the major axis of the inner ring and its ansae are very close to  $r_{IAR}$ . The small inner oval in the schematic refers to a possible nuclear lens at the resolution of the SDSS image.

CGCG 13-75 - The galaxy is of type  $(R'_2) \text{SAB}(r'l)ab$ . The gap method places the  $R'_2$  close to and slightly outside  $r_{OLR}$ , while both the  $r'l$  and the bar (defined by subtle ansae on the  $r'l$ ) just reach the  $r_{IAR}$ . The galaxy has some slight asymmetry, and the colour index maps indicate the gaps on both sides are red while the  $R'_2$  and the  $r'l$  are slightly bluish.

CGCG 65-2 - The galaxy is of type  $(R'_1) \text{SB}_a(rs,bl)ab$  and has a clear bar. The bl, which stands for “barlens,” refers to the rounder central zone (Laurikainen et al. 2011; see also paper 1). The galaxy has a well-defined  $R'_1$  outer pseudoring and clear dark gaps. The gap CR method places the  $R'_1$  entirely inside  $r_{OLR}$  and very close to the  $r_{OAR}$ . The schematic shows a four-part structure of the inner pseudoring, and that the bar and the inner pseudoring extend beyond the  $r_{IAR}$  but not beyond  $r_{CR}$ . In a colour index map, both the  $rs$  and the  $R'_1$  are slightly bluish. In the schematic, the  $R'_1$  is not displayed as a spiral because this aspect is very subtle.

CGCG 67-4 - This interesting case has the type  $(R_1 L) \text{SB}_a(s,bl,nl)0/a$  and is noteworthy for its strong blue bar ansae that do not appear to be merely the blue ends of an extremely elongated inner ring. The ansae are not arcs but roughly circular enhancements, and inside these features are both a barlens and a nuclear lens. The outer structure includes an  $R_1 L$  with only subtle gaps. The gap method places  $r_{CR}$  fully outside the bar ansae, which in fact just reach  $r_{IAR}$ . The  $R_1 L$  also is fully within  $r_{OLR}$ , and is closer to  $r_{OAR}$ .

CGCG 73-53 - This early-type galaxy is classified as  $(R_1 R_2) \text{SAB}_a(l)0^+$ , an example where the outer morphology is a subtle double ring where the  $R_2$  may not be a pseudoring. The gaps are still distinguishable, and the implied  $r_{CR}$  has the weak bar ending at  $r_{IAR}$ , the inner lens extending halfway between  $r_{IAR}$  and  $r_{CR}$ , the  $R_1$  straddling the  $r_{OAR}$ , and the  $R_2$  almost exactly coinciding with  $r_{OLR}$ . In spite of the apparent early type, colour index maps indicate slightly bluer colours in the  $(R_1 R_2)$  compared to the gaps.

CGCG 185-14 - This galaxy is highly-inclined, leading to strong bulge deprojection stretch in the bright central area (bright vertical oval). The type is  $(R_1 R'_2) \text{SAB}_a(rs)ab$ , and is a case where the two outer ring features are separated by well-defined gaps both parallel and perpendicular to the bar. If we take the gaps perpendicular to the line joining the weak bar ansae to set  $r_{CR}$ , then the inner pseudoring and the ansae extend to near  $r_{IAR}$ , the  $R_1$  ring straddles  $r_{OAR}$ , and the  $R'_2$  lies just beyond  $r_{OLR}$ . All of the recognized ring features show slightly enhanced blue colours in colour index maps.

CGCG 263-22 - The morphology of this galaxy is interesting in the sense that it has what appears to be an  $R'_1$  outer pseudoring surrounding a broad inner pseudoring/oval. Within this pseudoring/oval, a second large pseudoring is seen. The bright central region itself is slightly oval nearly perpendicular to the main inner pseudoring/oval. The classification is  $(R'_1) \text{SAB}(rs,rs)a$ , accounting for all the ring features. The well-defined gaps along the line perpendicular to the main inner pseudoring/oval place  $r_{CR}$  almost exactly around the

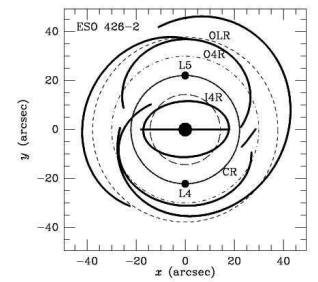
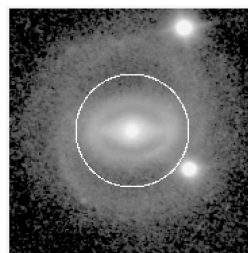
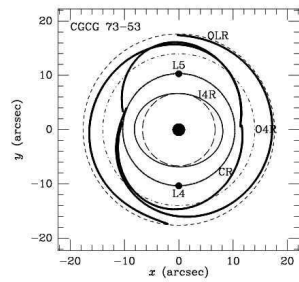
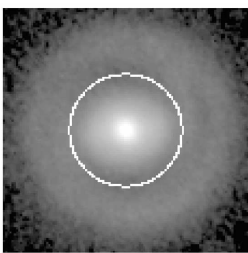
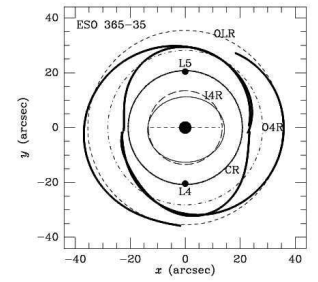
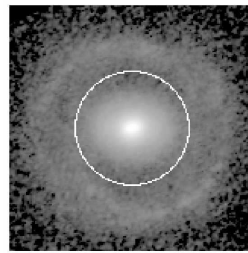
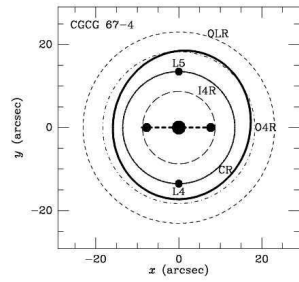
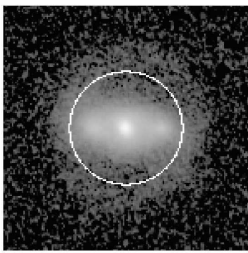
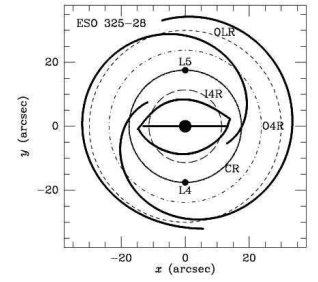
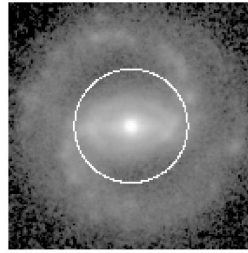
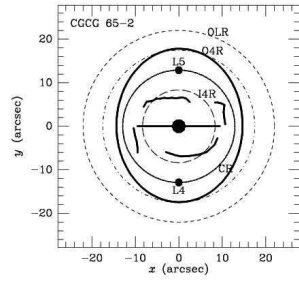
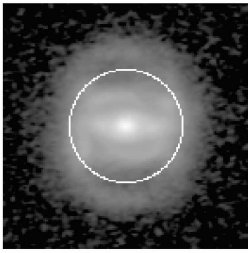
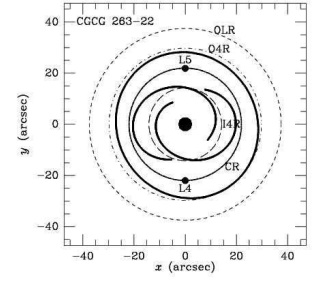
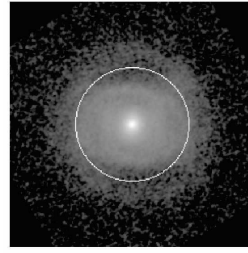
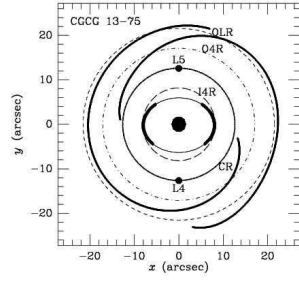
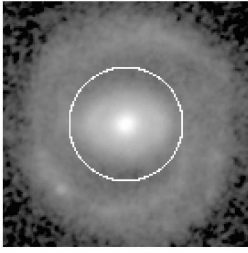
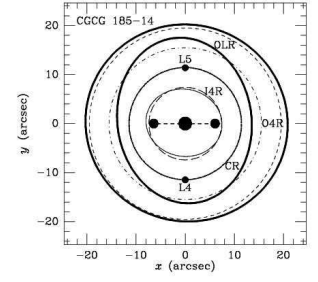
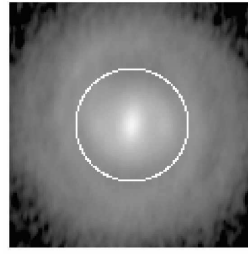
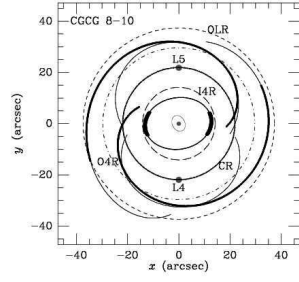
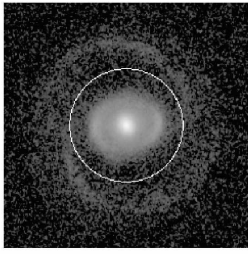


Figure 13.

Figure 13. (cont.)



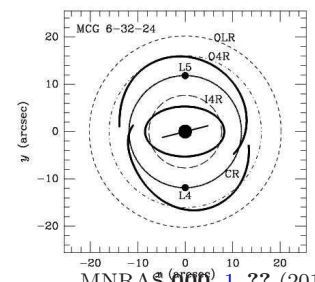
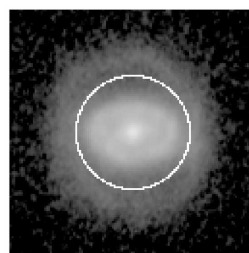
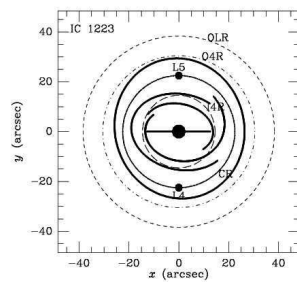
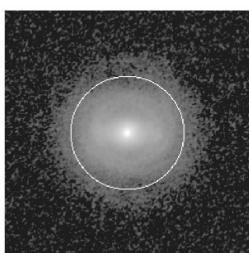
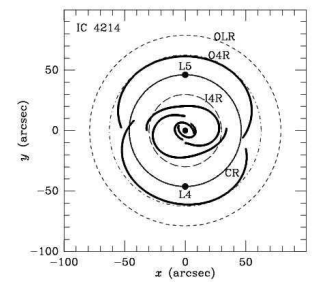
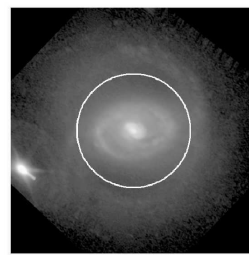
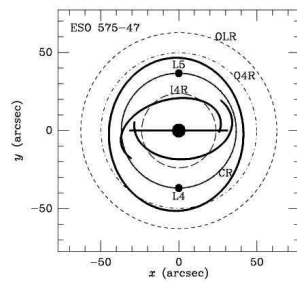
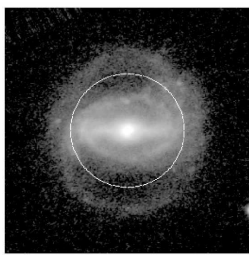
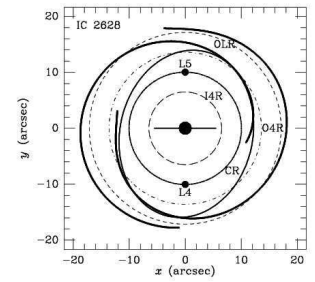
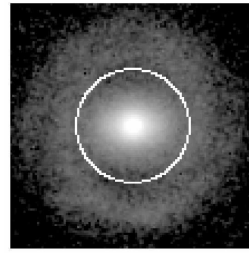
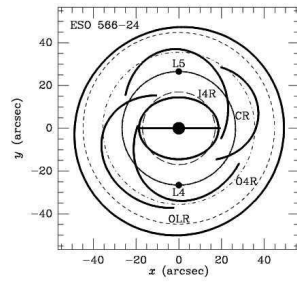
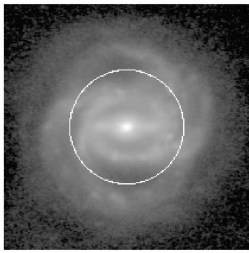
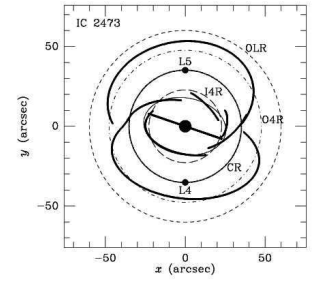
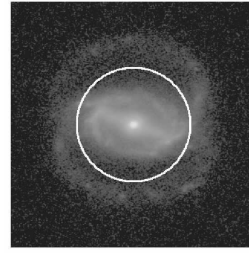
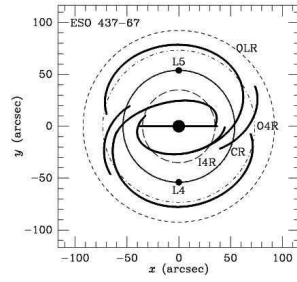
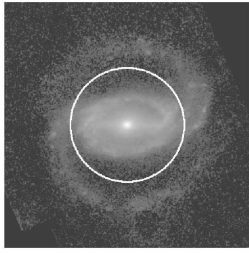
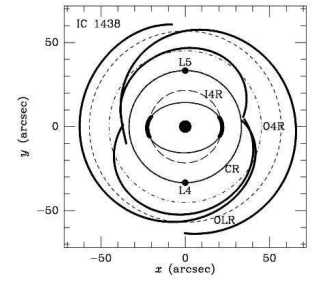
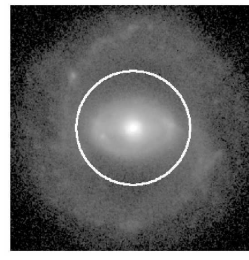
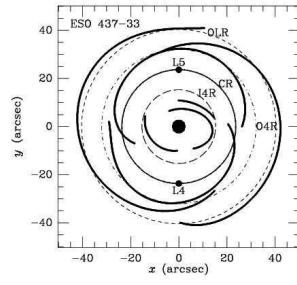
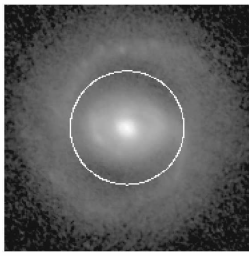


Figure 13. (cont.)

Figure 13. (cont.)



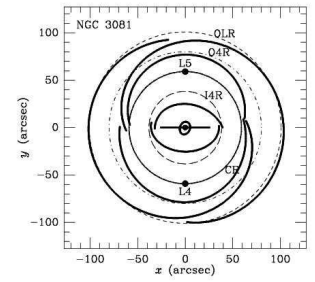
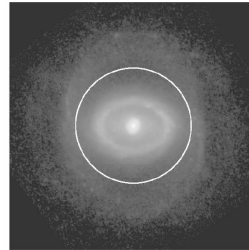
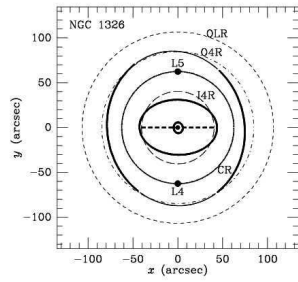
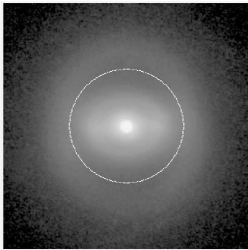
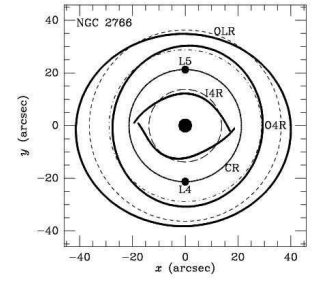
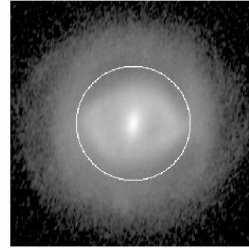
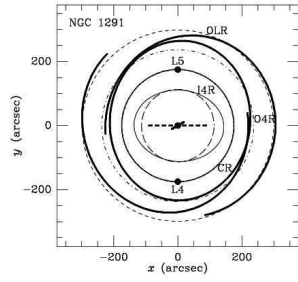
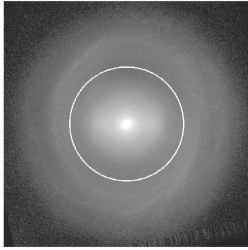
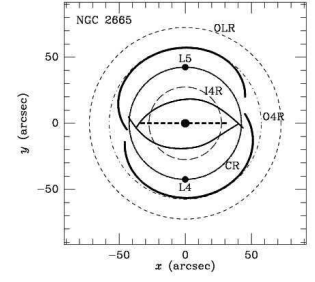
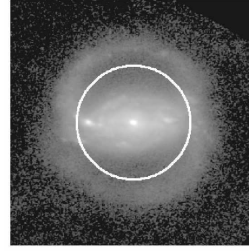
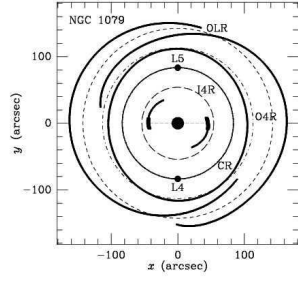
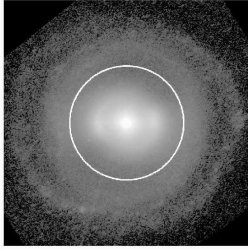
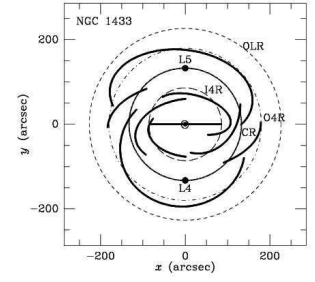
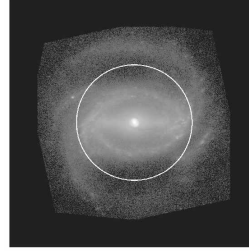
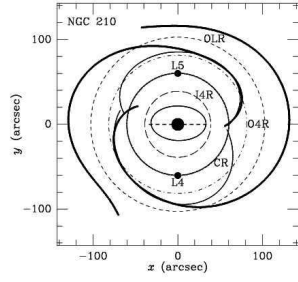
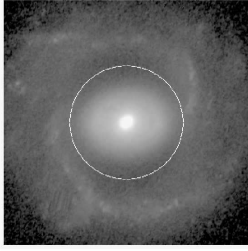
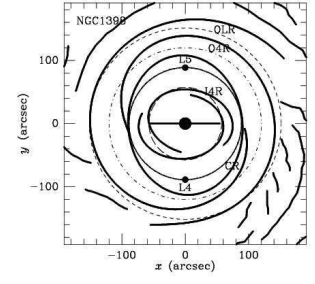
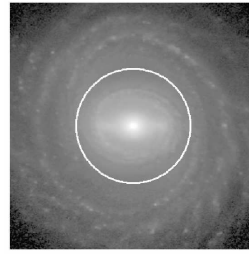
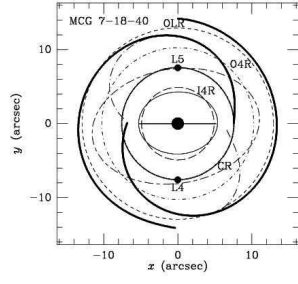
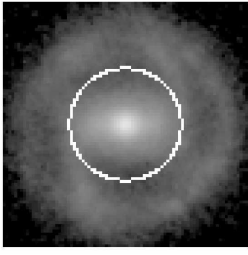


Figure 13. (cont.)

Figure 13. (cont.)

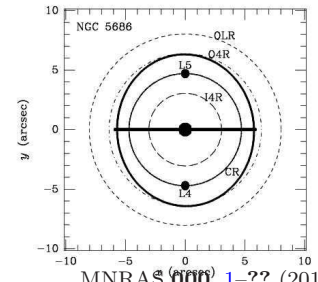
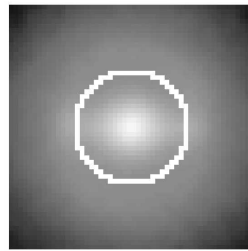
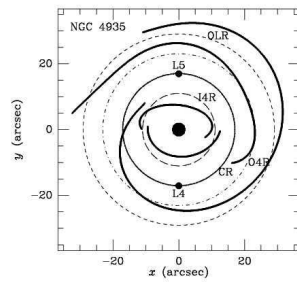
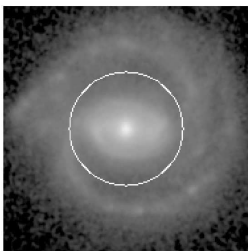
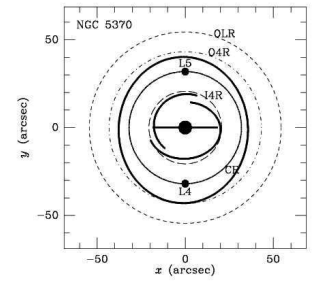
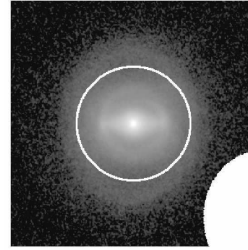
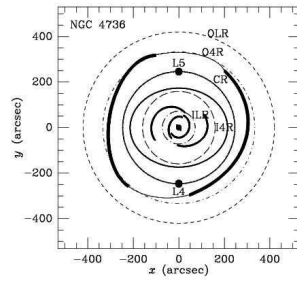
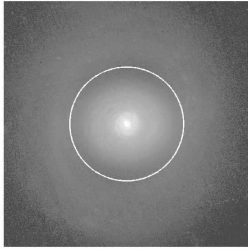
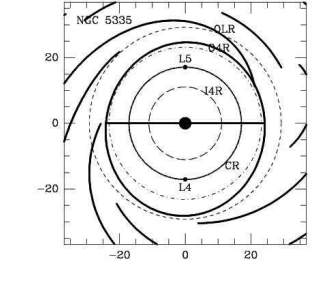
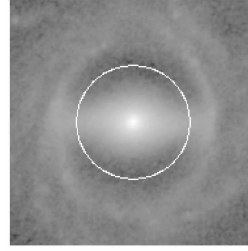
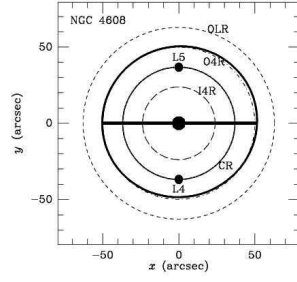
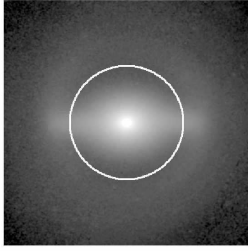
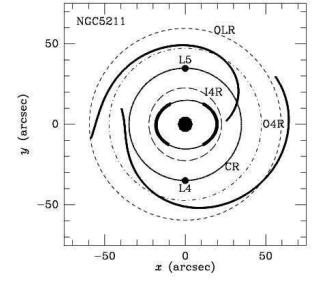
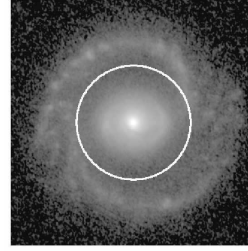
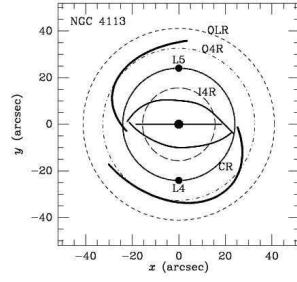
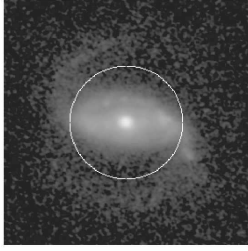
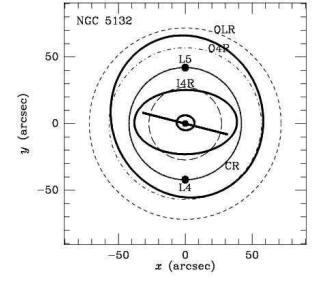
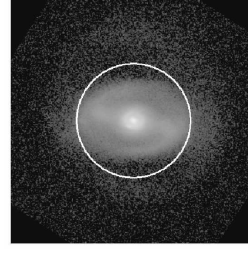
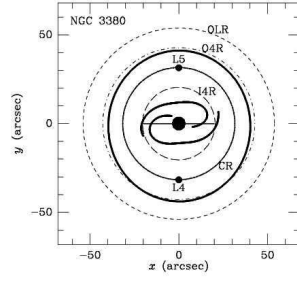
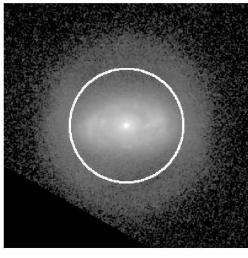
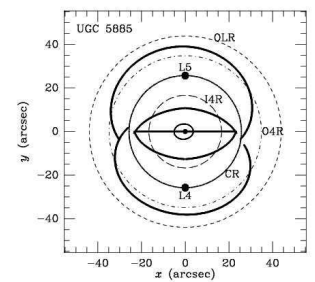
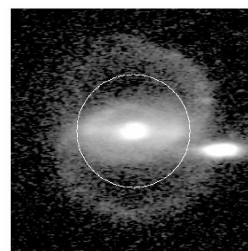
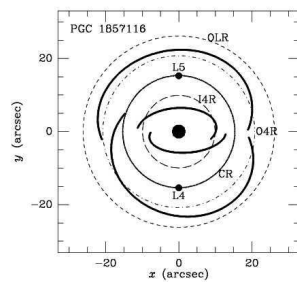
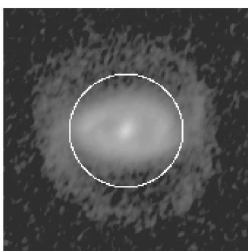
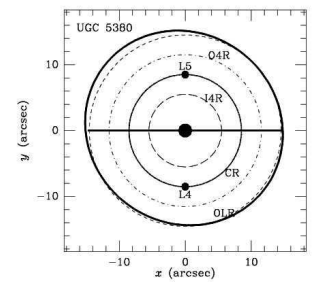
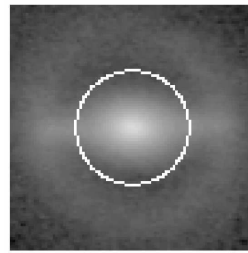
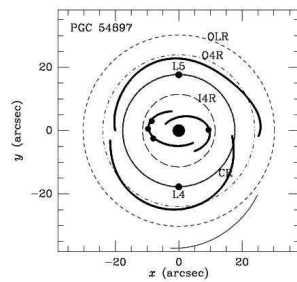
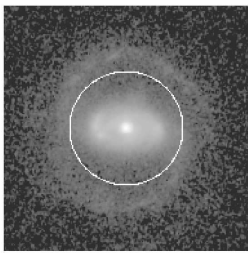
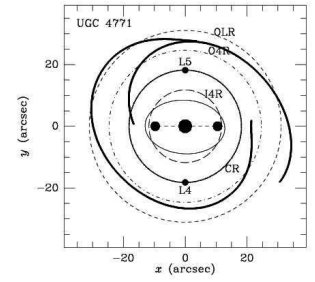
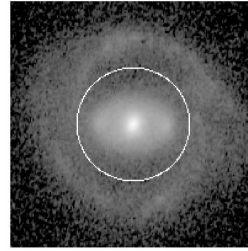
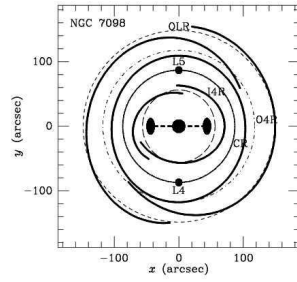
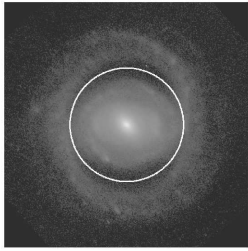
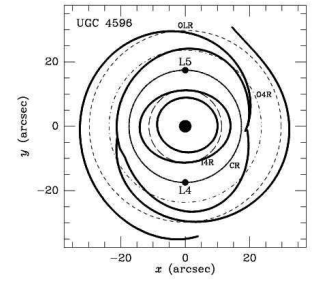
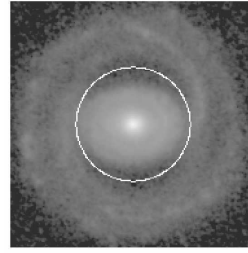
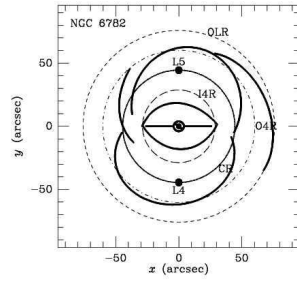
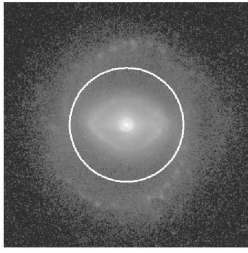
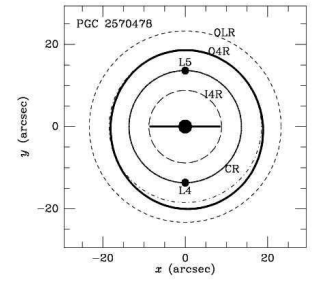
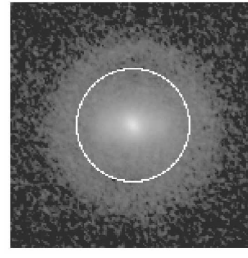
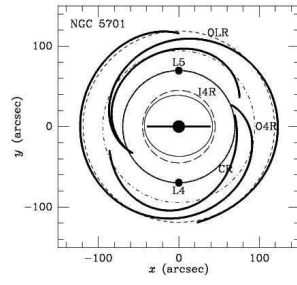
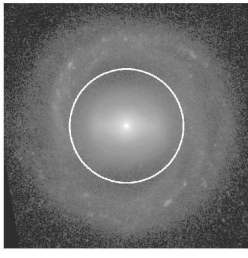
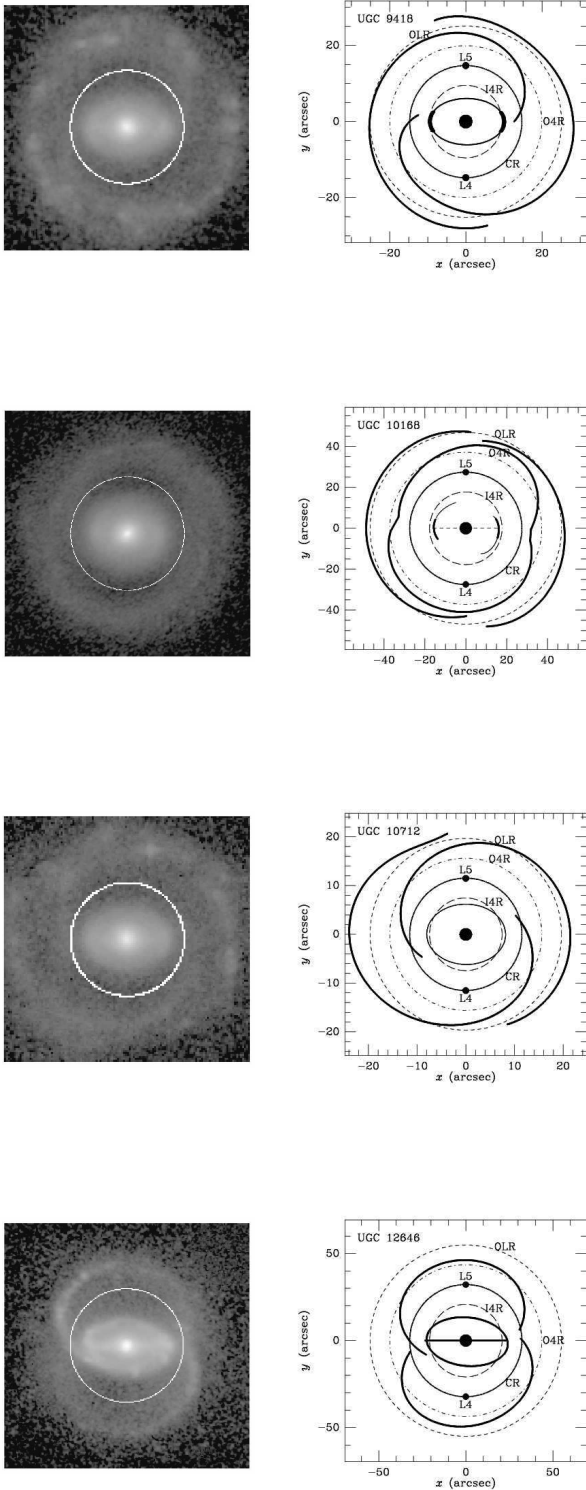


Figure 13. (cont.)

Figure 13. (cont.)







**Figure 13.** Images and Schematics: (left) Deprojected  $g$  or  $B$ -band image with corotation circle superposed; (right) schematic showing visually-mapped structures and their relation to corotation and other labeled resonance radii. Filled circles perpendicular to the bar axis on the CR circle are the interpreted locations of the  $L_4$ ,  $L_5$  points. In some cases, filled circles or ovals refer to bar ansae.

ends of the oval. The  $R'_1$  in this case just reaches the  $r_{O4R}$  well inside the predicted  $r_{OLR}$ . A  $g-i$  colour index map shows that the rim of the large inner pseudoring/oval is slightly bluer than the inside of the feature. The smaller rs shows no clear colour contrast.

ESO 325-28 - This CSRG galaxy has a type of  $(R'_2)SB(r)b$  (BC91) and is basically face-on. The galaxy has strong, dark gaps in the zones perpendicular to the obvious bar. The inner ring is extremely oval and in blue light seems underfilled by the bar. This is less apparent in the  $I$ -band. The gap method places  $r_{CR}$  such that the bar and the major axis of the inner ring slightly overextend  $r_{I4R}$ . The two main spiral arms lie largely outside  $r_{CR}$ , with the prominent but slightly asymmetric  $R'_2$  lying a little beyond  $r_{OLR}$ . The schematic shows also that the outer arms may begin between  $r_{I4R}$  and  $r_{CR}$ . A colour index map shown in BC91 reveals enhanced blue colours in the central region.

ESO 365-35 - This galaxy was classified by BC91 as  $(R'_2)SAB(l)0/a$ . However, a subtle  $R_1$  component is also recognizable, and we reclassify the galaxy as  $(R_1R'_2)SAB(l)0/a$ . The galaxy has strong gaps and only a very weak bar. The gap method places the ends of the weak bar as well as the major axis radius of the bright inner lens near  $r_{I4R}$ . The  $R_1$  straddles  $r_{O4R}$ , while the  $R'_2$  just reaches  $r_{OLR}$ . A colour index map in BC91 shows that most of the recent star formation in ESO 365-35 is confined to the  $R'_2$  outer pseudoring.

ESO 426-2 - The strongest features of this galaxy are its inner ring and bar. In blue light the latter appears to underfill the former, but in the  $I$ -band they are matched in size. The type is  $(R_1R'_2)SB(r)0/a$  (BC91). From the well-defined gaps,  $r_{CR}$  is placed such that the bar ends just beyond  $r_{I4R}$ , the inner ring straddles  $r_{I4R}$ , the  $R_1$  straddles  $r_{O4R}$ , and the  $R'_2$  extends just a little beyond  $r_{OLR}$ . The colour index map of ESO 426-2 in BC91 shows the inner ring to be a strong, smooth zone of recent star formation, with some recent star formation also in the  $R_1$  ring.

ESO 437-33 - The CVRHS type is  $(R'_1R'_2)SAB(rs,nr)ab$ . The gaps are strong in this case, and the gap method places  $r_{CR}$  such that the bar and the inner pseudoring extend to  $r_{I4R}$ , the strong  $R'_1$  straddles  $r_{O4R}$ , and the subtle  $R'_2$  straddles  $r_{OLR}$ . BC91 show a colour index map of this galaxy that reveals the  $R'_2$  outer pseudoring better than does the  $B$ -band image alone. This map shows considerable star formation in this feature as well as in the inner pseudoring and the nuclear ring.

ESO 437-67 - Classified as  $(R'_1)SB(rs,nr)ab$  by BC91, this galaxy has well-defined features. The gap method places  $r_{CR}$  such that the bar ends at  $r_{I4R}$ , while the major axis radius of the inner ring extends a little outside  $r_{I4R}$ . The two arms of the strong and large  $R'_1$  lie mostly outside  $r_{CR}$  but do not extend much beyond  $r_{O4R}$ . A subtle doubling of these arms in the regions just off the inner ring major axis is more strongly emphasized in the schematic. This doubling extends from between  $r_{I4R}$  and  $r_{CR}$  to between  $r_{O4R}$  and  $r_{OLR}$ . The galaxy strongly resembles NGC 1433.

ESO 566-24 - Classified as  $(R)SB(r)b$  in the deVA, the galaxy is remarkable for its strong inner four-armed spiral pattern. This zone is surrounded by a subtle outer ring that the schematic shows lies just outside  $r_{OLR}$ . The galaxy was studied in detail by Rautiainen et al. (2004) using numerical simulations. These authors suggested that the four-armed spiral is linked to the O4R with the strong bar. The gaps



in ESO 566-24 are strong enough to re-evaluate this possible connection. These give an  $r_{CR}$  such that the bar and the inner ring extend to  $r_{IAR}$ . If the entire four-armed pattern is used to define a pseudoring, the feature so defined is roughly circular and straddles  $r_{OAR}$ . This supports the conclusion of Rautiainen et al. (2004). The schematic shows how the four-armed pattern is largely confined between  $r_{IAR}$  and  $r_{OAR}$ .

ESO 575-47 - Classified as  $(R'_1)SB(rs)ab$  by BC91, this galaxy has strong features and well-defined gaps. The gap method places  $r_{CR}$  such that the bar extends to between  $r_{IAR}$  and  $r_{CR}$ , while the  $(rs)$  just reaches  $r_{CR}$ . The  $R'_1$  straddles  $r_{OAR}$  closely, and lies well inside  $r_{OLR}$ . The inner ring of this galaxy bears a strong resemblance to that seen in NGC 1433. IC 1223 - The type is  $(R')SB(rs,rs,bl)a$ . The most noteworthy feature is the doubled inner pseudoring. The bar fills the inner  $rs$ . The gap method  $r_{CR}$  places both the ends of the strong apparent bar and the inner  $rs$  within  $r_{IAR}$ . The larger  $rs$  overextends  $r_{IAR}$  but is entirely within  $r_{CR}$ . Surprisingly, the outer feature lies just outside  $r_{CR}$ , mostly inside  $r_{OAR}$ . The outer  $rs$  shows enhanced blue colours in a colour index map.

IC 1438 - The CVRHS classification is  $(R_1R'_2)SAB(r,nr)a$ . The gaps are well-defined and give  $r_{CR}$  such that the inner ring and bar (the latter shown in the schematic as arc ansae) extend to  $r_{IAR}$  and the slightly asymmetric  $R_1$  component straddles  $r_{OAR}$ . The  $R'_2$  is mostly outside  $r_{OLR}$ . The schematic shows how the subtle dimples in the  $R_1$  component lie near  $r_{CR}$ . Buta (1995) brought attention to the  $R_1$ ,  $R'_2$  dichotomy in this galaxy, where the  $R_1$  component is most prominent in the  $I$ -band while the  $R'_2$  component is most prominent in the  $B$ -band. A colour index map of the galaxy is shown in Buta (1995).

IC 2473 - This object [type  $(R'_1)SB(r,bl)ab$ ] strongly resembles ESO 437-67, except that the bar appears twisted away from the strong apparent dimples in the  $R'_1$  outer pseudoring. The displayed image rotates the dimples to the horizontal, instead of the bar, since the dimples define the axis of a massive inner oval. The gap method *relative to this oval* places both the bar ends and the major axis of the inner ring just outside  $r_{IAR}$ , while the asymmetric  $R'_1$  is entirely within  $r_{OLR}$ , mostly close to  $r_{OAR}$ . Central star formation, a circumnuclear dust ring, and enhanced blue colours in the inner ring and  $R'_1$  outer pseudoring are seen in a  $g-i$  colour index map.

The schematic shows how the  $L_4$  and  $L_5$  points would be twisted towards the ends of the prominent gaps if the axis perpendicular to the bar were used to get  $r_{CR}$ . The centre of the gaps is closer to the line perpendicular to the dimple axis (horizontal as shown). Either direction gives about the same value of  $r_{CR}$ .

IC 2628 - The type is  $(R_1R'_2)SAB(l)a$ . The dark gaps are clear in this case, and using the gap method,  $r_{CR}$  is placed such that the weak bar extends very close to  $r_{IAR}$ , the  $R_1$  straddles  $r_{OAR}$ , and the  $R'_2$  lies just outside  $r_{OLR}$ . The colour index map shows enhanced blue colours in the zone of the  $R_1R'_2$  feature.

IC 4214 - This well-studied object (Buta et al 1999; Salo et al. 1999) has a type of  $(R_1)SA(rs,nr)a$  (BC91). It has no clear bar, although the inner pseudoring defines a massive, bar-like oval. The gap method places  $r_{CR}$  such that the inner pseudoring extends to  $r_{IAR}$ . The  $R_1$  outer ring just reaches the  $r_{OAR}$ , well inside  $r_{OLR}$ .

MCG 6-32-24 - This galaxy has strong features. The type is  $(R_1)SAB(r)0/a$ , with the rings being much more obvious than the bar. The latter is a short feature inside the inner ring. The gaps are well-defined, and the gap method places  $r_{CR}$  such that the bar ends well inside  $r_{IAR}$ , the inner ring extends close to  $r_{IAR}$ , and the  $R_1$  outer ring extends just to  $r_{OAR}$ . A  $g-i$  colour index map shows strong star formation only in the highly-elliptical inner ring.

MCG 7-18-40 - This galaxy, type  $(R'_2)SB_a(l)b$ , shows four well-defined dark zones: two along the line perpendicular to the bar, and two along the line parallel to the bar. Each zone is distinct from each other zone, such that an  $R_1$  component (dot-long dash curves in schematic) can be recognized. If the gaps perpendicular to the bar (which has subtle ansae) are used to locate  $r_{CR}$ , then the inner lens and bar extend close to the  $r_{IAR}$ , while the  $R'_2$  lies almost exactly at  $r_{OLR}$ . The subtle  $R_1$  component also reaches  $r_{OLR}$ , which is different from most of the galaxies in the OLR subclass sample. With  $r_{CR}$  defined by the perpendicular gaps, the parallel gaps are at a larger radius, closer to  $r_{OAR}$ . The broad short-dash/long-dash oval in the schematic maps the rough midsections of the four dark areas, with a major axis extending between  $r_{OAR}$  and  $r_{OLR}$ , and the minor axis at  $r_{CR}$ .

NGC 210 - This galaxy is neither a GZ2 nor a CSRG case, but a large example from the deVA. Our analysis is based on a red continuum image (Crocker et al. 1996) rather than  $BVI$  or  $gri$ . The CVRHS classification is  $(R'_1R'_2)SAB(l,nr)b$ . The dark gaps are well-defined and give  $r_{CR}$  such that the bar extends very nearly to the  $r_{IAR}$ . The major axis of the  $R'_1$  extends nearly to  $r_{OLR}$ , while the  $R'_2$  is close to but mostly outside  $r_{OLR}$ . The gap method places most of the spiral structure of NGC 210 outside corotation, and the oval lens/bar inside  $r_{IAR}$ .

NGC 1079 - This galaxy is an excellent, large and mostly symmetric example having an  $R_1R'_2$  morphology. Its full type is  $(R_1R'_2)SAB_a(r'l,bl)a$ . The dark gaps are clear, and the implied  $r_{CR}$  places both the ends of the bar and the inner pseudoring-lens just within  $r_{IAR}$ . The bright and virtually complete  $R_1$  component lies mostly at  $r_{OAR}$  and shows little or no dimpling. The  $R'_2$  is predicted to lie outside but still near  $r_{OLR}$ . The structure of the galaxy is remarkably consistent with a single pattern speed model.

NGC 1291 - This large example of an early-type outer-ringed galaxy (de Vaucouleurs 1975) also falls neatly within the outer resonant subclass morphologies. Its CVRHS type is  $(R_1R'_2)SAB(l,nb)0/a$ . The well-defined gaps give  $r_{CR}$  such that the primary bar and inner lens extend close to  $r_{IAR}$ . The  $R_1$  component, which in this case is not dimpled, appears to straddle  $r_{OAR}$ , while the  $R'_2$  component closely straddles  $r_{OLR}$ . The  $R_1$  components of NGC 1079 and 1291 are similar, but the  $R'_2$  component of NGC 1291 is more diffuse than that in NGC 1079. The schematic also shows the prominent secondary bar.

NGC 1326 - This galaxy has a strong, well-defined outer ring. The type is  $(R_1)SAB(r,nr)0/a$ . The gaps are diffuse but give  $r_{CR}$  such that the bar extends to  $r_{IAR}$ , with the inner ring extending a little beyond  $r_{IAR}$ . The bright  $R_1$  outer ring straddles  $r_{OAR}$ , well inside  $r_{OLR}$ . The schematic also highlights an interesting characteristic of the  $R_1$  outer ring in this galaxy: the ring is brighter in arcs around the bar/oval major axis and weaker along the bar/oval minor axis.

NGC 1398 - This complex spiral, type  $(R',R_1)SB(rs)ab$ , has

subtle gaps in an outer  $R_1$  ring feature that appears almost “buried” within the strong multi-armed spiral pattern. The two strong spiral arms just outside the inner pseudoring form an unclosed outer pseudoring (the  $R'_1$  in the classification) breaking from the minor axis zones of the  $R_1$  component. The latter also looks much smoother than the former. When the gaps are taken to define  $r_{CR}$ , the strong bar and inner pseudoring are found to extend almost exactly to  $r_{IAR}$ , while the  $R_1$  extends from  $r_{CR}$  to just under  $r_{OAR}$ . The inner two-armed spiral interpreted as an unclosed  $R'_2$  just reaches  $r_{OLR}$ . Much of the pattern outside  $r_{OLR}$  is multi-armed and lies at radii where no bisymmetric resonances would exist if the system has only a single pattern speed.

NGC 1433 - This classic ringed barred spiral, type  $(R'_1)SB(p,rs,nr,nb)ab$  has well-defined gaps. When these are used to locate  $r_{CR}$ , the bar is found to extend exactly to  $r_{IAR}$ , while the inner ring extends a little further and is asymmetric. The distinct four-fold pattern of the inner ring (including the short arms off the bar ends) lies almost entirely within  $r_{CR}$ . The detached secondary arcs located just off the leading quadrants of the strong inner ring appear to be confined between  $r_{CR}$  and  $r_{OAR}$ . These features, which Buta (1984) called “plumes,” are recognized by the “p” in the classification. Also, the prominent  $R'_1$  outer pseudoring straddles  $r_{OAR}$ , well inside  $r_{OLR}$ . The identification of the  $R'_1$  feature in NGC 1433 with the O4R was also proposed by Treuthardt et al. (2008).

NGC 2665 - The BC91 classification is  $(R'_1)SAB(rs)a$ . The gaps are apparent but not deep. In this case, the gap method places both the major axis of the inner ring and the bar ends about halfway between  $r_{IAR}$  and  $r_{CR}$ . The bright, slightly asymmetric  $R'_1$  extends to  $r_{OAR}$ . The schematic emphasizes the symmetric aspects of this feature.

NGC 2766 - This interesting case has a type of  $(R_1R'_2)SAB(r)a$ . The system is highly-inclined, however, and the deprojected image shows significant bulge deprojection stretch. The galaxy is noteworthy for its extremely cuspy oval inner ring, a feature which also has strong azimuthal colour variations in the sense that the ring is bluer around the cusps. The galaxy has no clear bar, although the inner ring is bar-like. The gap method places  $r_{CR}$  such that the inner ring straddles  $r_{IAR}$ .  $r_{CR}$  lies outside the ring ends, while the  $R_1$  straddles  $r_{OAR}$  and the  $R'_2$  lies close to but outside  $r_{OLR}$ . The inner ring cusps are close to but inside  $r_{CR}$  in this case.

NGC 3081 - This well-studied object (Buta & Purcell 1998; Buta et al. 2004) is a prototype of the  $(R_1R'_2)$  morphology, and has a CVRHS type of  $(R_1R'_2)SAB(r,nr,nb)0/a$ . The galaxy strongly resembles models of barred galaxies (Schwarz 1981; 1984a; Buta & Purcell 1998). The gaps are subtle and best measured on residual intensity images. With this approach, the gap method places  $r_{CR}$  such that the bar ends a little inside  $r_{IAR}$ , while the major axis of the inner ring extends up to  $r_{IAR}$ . While in past studies both the  $R_1$  and  $R'_2$  components were considered linked to the OLR, the schematic gives a different interpretation. The  $R_1$  component extends to  $r_{OAR}$  while the  $R'_2$  extends to  $r_{OLR}$ .

NGC 3380 - Most of the star formation in this galaxy peculiarly lies within the bar/oval zone. Little or no star formation is detectable in the prominent outer ring/lens. The galaxy has a type of  $(R_1L)SAB(l,rs,bl)ab$ , where the inner pseudoring is one of the most highly-elongated cases known.

The gaps are subtle but definable in a median difference image. The  $r_{CR}$  so implied places the inner ring and the ends of the bar at  $r_{IAR}$ . The inner ring and bar are also embedded within an oval lens-like zone that extends to  $r_{CR}$ . The  $R_1L$  closely straddles  $r_{OAR}$ , and is well inside  $r_{OLR}$ . The bar-lens (bl) recognized in the classification is seen best in the  $i$ -band image. A  $g-i$  colour index map also reveals some central star formation.

NGC 4113 - This galaxy, type  $(R'_1)SAB(rs,nr)ab$ , has an extremely elongated, cuspy-oval inner ring. The ring and the bar are slightly misaligned. Although the  $R'_1$  is faint and the gaps are weak, the gap method is still applicable and yields an  $r_{CR}$  such that the bar and inner ring both extend between  $r_{CR}$  and  $r_{IAR}$ . The  $R'_1$  extends between  $r_{OAR}$  and  $r_{OLR}$ . A  $g-i$  colour index map reveals a small nuclear star-forming ring. The schematic shows that the cusps in the inner ring extend close to but just inside  $r_{CR}$ .

NGC 4608 - This galaxy, type  $(RL)SB(rl,bl)0/a$ , is not the same as any of the others described so far in the sense that there are no dark gaps between an inner ring and outer ring. Instead, the dark zones are *inside* an apparent inner ring. If these gaps are identified as the  $L_4$ ,  $L_5$  Lagrangian points, then both the inner ring and bar in this galaxy lie at  $r_{OAR}$ , outside  $r_{CR}$  (i. e., a region forbidden to support a bar in standard barred galaxy orbit theory). The faint structure outside the bar would then lie outside  $r_{OLR}$ . A  $g-i$  colour index map shows little or no recent star formation.

NGC 4736 - This large, nearly face-on object was selected from the deVA for its strong inner ring of star formation and a very broad and diffuse outer ring. The galaxy has no clear bar; instead, it has a broad oval bar-like structure. Lindblad (1960) and Schommer & Sullivan (1976) proposed that corotation would likely be in the prominent gap region between the massive oval (which is lens-like) and the outer ring. The CVRHS classification of NGC 4736 is  $(R)SAB(r'l,rs)ab$ , where the  $r'l$  refers to the boundary of the massive oval. Although the outer ring is very diffuse and extends well-beyond  $r_{OLR}$ , the main ridge of the feature straddles  $r_{OAR}$ . The best known feature of the galaxy is the bright inner pseudoring, which is defined by active star formation and a tightly-wrapped spiral character. This feature is an analogue of a nuclear ring in a barred spiral and is probably linked with an ILR. The schematic of this galaxy is the only one showing the predicted location of  $r_{ILR}$ , and it highlights how the  $rs$  lies just inside  $r_{ILR}$  for a perfectly flat rotation curve. The schematic also highlights how the outer ring is, like that in NGC 1326, weak along the axis perpendicular to the oval. The gap method gives  $r_{CR}$  such that the massive oval extends to between  $r_{IAR}$  and  $r_{CR}$ .

NGC 4935 - This somewhat asymmetric object, type  $(R'_2)SAB_a(rs)b$ , has a partial  $R'_2$  and does not appear to also have a trace of an  $R_1$ . The bar is mostly an oval having the same extent as the inner pseudoring. The gaps are not deep, but median difference images define the gaps well enough to measure  $r_{gp}$ . The resulting value of  $r_{CR}$  places the bar/oval/inner pseudoring as extending to  $r_{IAR}$  and the  $R'_2$  as extending close to and outside  $r_{OLR}$ . A  $g-i$  colour index map shows that both the inner pseudoring and the  $R'_2$  outer pseudoring are zones of enhanced blue colours, with no clear central star formation.

NGC 5132 - This galaxy, type  $(R'_1)SB(rs,bl,nr)a$ , has three well-defined ring features. A noteworthy characteristic of the

galaxy is the slight misalignment between the prominent bar and the major axis of the inner ring. In this case, the massive oval is used to define the locations of  $L_4$  and  $L_5$  in the schematic. In spite of the faintness of the  $R'_1$ , the gap method can still be used and gives  $r_{CR}$  such that the bar extends just past  $r_{I4R}$  and the inner ring extends to just inside  $r_{CR}$ . The  $R'_1$  outer pseudoring is asymmetric but appears to be confined between  $r_{O4R}$  and  $r_{OLR}$ . A  $g-i$  colour index map reveals star formation in the nuclear and inner rings, but little or no star formation in the  $R'_1$ .

NGC 5211 - This galaxy, type  $(R'_2)SA(rs)b$ , strongly resembles NGC 4935. The gaps are well-defined, and these give an  $r_{CR}$  such that the inner pseudoring and weak bar (which is clear in the  $i$ -band but less so in the  $g$ -band) extend to just short of  $r_{I4R}$ , and the two main spiral arms lie mostly outside  $r_{CR}$ . As for NGC 4935, the  $R'_2$  is slightly asymmetric, and extends to  $r_{OLR}$ . Although the galaxy has little conventional bar in  $g$ -band light, the schematic highlights broad arc ansae in the inner pseudoring.

NGC 5335 - As noted in section 5.2, this galaxy, classified as  $SB(rs,bl)ab$ , is the darkest (r) dark-spacer in the sample. As for NGC 4608, the gap method places the ends of the bar and the bright inner ring close to  $r_{O4R}$ . Much of the multi-armed outer spiral pattern would be located outside  $r_{OLR}$ , in an area where no bisymmetric resonances would exist, if the object has only a single pattern speed.

NGC 5370 - This galaxy, type  $(R_1L)SB_a(rs,bl)0/a$ , is unusual in having a strong bar and a relatively circular inner ring. The features are well-defined but the gaps are subtle. Using the median difference approach, the method gives  $r_{CR}$  such that the inner ring and bar extend close to but just inside  $r_{I4R}$ . The  $R_1L$ , which is non-dimpled, is confined mostly between  $r_{CR}$  and  $r_{O4R}$ . A  $g-i$  colour index map shows that the inner pseudoring and the  $R_1L$  have slightly enhanced blue colours, with no central star formation. The bar of NGC 5370 is also unusual in having a diamond shape and small ansae.

NGC 5686 - This interesting case, type  $SB_a(r,bl)0^0$ , has an excellent ansae-type bar and a faint, circular inner ring. The ring is a subtle (r) dark-spacer, and if the weak gaps are taken to define  $r_{CR}$ , then the inner ring and bar extend to  $r_{O4R}$ , with no further structure in a diffuse outer disk. A  $g-i$  colour index map reveals no active star formation in the galaxy.

NGC 5701 - This excellent large example, type  $(R_1R'_2)SB(r'l,bl)a$ , is nearly face-on and has strong dark gaps perpendicular to the bar. The gap method places  $r_{CR}$  such that the bar and  $r'l$  extend to just inside  $r_{I4R}$ . The  $R_1$  component straddles  $r_{O4R}$ , while the  $R'_2$  is either at or slightly larger than  $r_{OLR}$ . A  $g-i$  colour index map reveals star formation mainly in the  $R'_2$ , with a trace of bluer colours also on one side of the  $R_1$ . No star formation is associated with the  $r'l$  or in the central region.

NGC 6782 - This CSRG galaxy, type  $(R'_1)SB(r,nr,nb)a$ , has an excellent cuspy-oval inner ring, a strong nuclear ring and secondary bar, and a conspicuous knotty  $R'_1$ . The gaps are well-defined, and give an  $r_{CR}$  which places the bar ends and the major axis cusp points of the inner ring at  $r_{I4R}$ . The  $R'_1$  outer pseudoring straddles  $r_{O4R}$ , and seems well inside  $r_{OLR}$ . NGC 6782 is a well-studied object and has been the subject of sophisticated numerical simulations (Lin et al. 2008).

NGC 7098 - This exceptional large object, of type

$(R_1R'_2)SAB_a(rs,nb)ab$ , has strong dark, banana-shaped gaps between its inner and outer ring features. The gap method places  $r_{CR}$  such the bar extends to  $r_{I4R}$ , while the inner ring extends between  $r_{I4R}$  and  $r_{CR}$ . The  $R_1$  component, which is slightly dimpled, extends only to  $r_{O4R}$  while the  $R'_2$  component straddles  $r_{OLR}$ . A  $B-I$  colour index map (Buta 1995) shows that all three ring features in the galaxy have slightly enhanced blue colours and are zones of recent star formation, while the prominent linear ansae have no colour contrast. The nb in the classification refers to an inner secondary oval. The schematic emphasizes the strong, nearly linear bar ansae.

PGC 54897 - This galaxy, type  $(R'_1)SAB_a(r'l)ab$ , has an excellent  $R'_1$  with subtle gaps. The gap method places  $r_{CR}$  such that the inner pseudoring/bar-oval extend to  $r_{I4R}$  while the  $R'_1$  straddles  $r_{O4R}$ , well-inside  $r_{OLR}$ . A  $g-i$  colour index map reveals active star formation in both the  $r'l$  and the  $R'_1$ , in addition to some nuclear star formation (a partial nuclear ring).

PGC 1857116 - A small and distant object with strong features. The type is  $(R'_1)SAB(rs)a$ . The gaps are well-defined and give  $r_{CR}$  such that the inner pseudoring/bar-oval (which is a subtle ansae-type) extends to  $r_{I4R}$ . The prominent  $R'_1$  extends to between  $r_{O4R}$  and  $r_{OLR}$ .

PGC 2570478 - A small object, type  $(R')SB(s)a$ . The bar is boxy, and the gaps are well-defined. These give an  $r_{CR}$  such that the bar extends exactly to  $r_{I4R}$  while the  $R'$  straddles  $r_{O4R}$ . The bar is surrounded by a broad diffuse zone that cannot be characterized as an inner lens. A  $g-i$  colour index map reveals some enhanced star formation in the  $R'$ .

UGC 4596 - As described already in section 5, this galaxy, type  $(R_1R'_2)SA(rr)b$ , has strong dark gaps in spite of the lack of an apparent bar. Instead the inner zone is a bar-like oval rimmed by two inner rings. The  $R_1R'_2$  morphology is well-defined, and the gap method has the  $R_1$  component straddling  $r_{O4R}$  while the  $R'_2$  lies just outside  $r_{OLR}$ . The doubled inner ring straddles  $r_{I4R}$ .

UGC 4771 - This excellent case, type  $(R'_2)SAB_a(l)b$ , strongly resembles NGC 4935 and 5211. The gaps are well-defined and give  $r_{CR}$  such that the bar extends to  $r_{I4R}$  with the inner lens straddling  $r_{I4R}$ . The  $R'_2$  straddles  $r_{OLR}$ . A  $g-i$  colour index map indicates recent star formation in the  $R'_2$  and possibly also near the rim on one side of the inner lens.

UGC 5380 - A typical (r) dark-spacer, type  $(L)SB(r,bl)0/a$ . The gap method applied to this galaxy places  $r_{CR}$  such that the bar and inner ring straddle  $r_{OLR}$ . The outer disk has a sharp outer edge, but if the bar in UGC 5380 is in fact a superfast type, then the outer lens would not have a resonant origin. A  $g-i$  colour index map reveals little or no recent star formation in the galaxy.

UGC 5885 - This galaxy, type  $(R'_1)SAB_a(rs,nr)ab$ , is highly-inclined although the centre is likely to be a pseudobulge since it shows little deprojection stretch. The  $R'_1$  is an excellent example with strong dimpling. The gap method places  $r_{CR}$  such that the inner ring and bar extend close to but slightly inside corotation, one of the very few cases in the sample like this. The cusps of the inner ring lie close to  $r_{CR}$ . The  $R'_1$  mostly straddles  $r_{O4R}$ , although its major axis is halfway between  $r_{O4R}$  and  $r_{OLR}$ . All of the ring features in the galaxy show some trace of recent star formation.

UGC 9418 - This galaxy, type  $(R'_2)SAB_a(r'l)b$ , has a strong  $R'_2$  outer pseudoring. The gaps are well-defined, and there is

little evidence for an  $R_1$  component. The gap method places  $r_{CR}$  such that the bar and inner pseudoring-lens straddle  $r_{I4R}$ , while the  $R'_2$  lies close to but mostly outside  $r_{OLR}$ . The colour index map shows strong star formation in the  $R'_2$  and subtle blue colours along the rim of the inner pseudoring-lens. There is little or no central star formation.

UGC 10168 - This galaxy has strong features and is an excellent example of an  $R_1R'_2$  morphology. The full classification is  $(R_1R'_2)SAB_a(r'l)a$ . The gaps are strong, and give  $r_{CR}$  such that the bar and inner pseudoring-lens extend close to but just inside  $r_{I4R}$ . The  $R_1$  component straddles  $r_{O4R}$ , while the  $R'_2$  straddles  $r_{OLR}$ . A  $g-i$  colour index map shows enhanced blue colours in the  $R_1R'_2$ , but no star formation in the inner pseudoring-lens.

UGC 10712 - This excellent example, type  $(R_1R'_2)SAB(rl)b$ , has nearly circular isophotes at the faintest detectable light level and has been assumed to be face-on. The gaps are well-defined and give an  $r_{CR}$  such that the inner ring-lens and the bar straddle  $r_{I4R}$ . The major axis of the  $R_1$  component and the minor axis of the  $R'_2$  component lie almost exactly at  $r_{OLR}$  in the manner of the two families of OLR orbits shown by Schwarz (1981). A  $g-i$  colour index map shows strong enhanced blue colours in the  $R_1R'_2$  feature and in the inner ring-lens. There appears to be little or no central star formation. The schematic excludes the  $R_1$  component, which is very faint in the  $g$ -band.

UGC 12646 - This galaxy was selected from Appendix 3 of RC3 as an exceptional example of its type,  $(R'_1)SB(r)ab$ . The obviously dimpled  $R'_1$  outer pseudoring is well-defined. The gaps are clear and give an  $r_{CR}$  such that the bar extends to  $r_{I4R}$ , while the highly-elongated inner ring extends just outside  $r_{I4R}$ . The  $R'_1$  mostly straddles  $r_{O4R}$ , but on one side nearly reaches  $r_{OLR}$ . The  $R'_1$  is nevertheless entirely confined within  $r_{OLR}$ .

*Comparison of CR radii* - Numerical simulations have been used to model the structure of four of our sample galaxies: NGC 1433, NGC 6782, IC 4214, and ESO 566-24. A comparison between estimates of  $r_{CR}$  from these models and from the gap method is shown in Figure 14. For NGC 1433, two estimates of  $r_{CR}$  are available from simulations:  $121''$  from Buta et al. (2001) and  $165''$  from Treuthardt et al. (2008); these have been averaged and the average deviation between them is plotted in Figure 14 as the horizontal error bar. The same has been done for NGC 6782, which has  $r_{CR}$  estimates of  $47''.2$  from Lin et al. (2008) and  $37''.1$  from Rautiainen et al. (2008). The former paper explicitly used a flat approximation to an observed rotation curve, while latter used a rotation curve inferred from an  $H$ -band image augmented by a halo contribution, which made the rotation curve also nearly flat. In models similar to those used by Rautiainen et al. (2008), Salo et al. (1999) estimated  $r_{CR} = 39'' \pm 3''$  for IC 4214, while Rautiainen et al. (2004) estimated  $r_{CR} = 28''.5$  for ESO 566-24. In these cases, the authors used models of observed nearly flat rotation curves for their analysis. Figure 14 shows that the agreement between  $r_{CR}$  from the gap method and the corresponding values from simulations is fairly good.

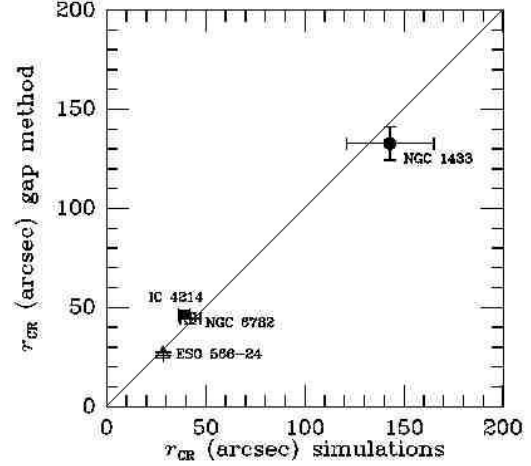


**Figure 14.** Graph of CR radii estimated from numerical simulations of four galaxies in our sample, and the CR radii estimated in this paper from the gap method.

## 8 ANALYSIS

Our analysis is based on the data in Tables 6–10. In these tables, the mean of any column is the average of the values in that column and  $\sigma_1$  is the standard deviation. The mean error is  $\sigma_1/\sqrt{N}$ , where  $N$  is the number of values used for the means.

### 8.1 (rR) dark-spacers

#### 8.1.1 Bar Extent

Let us begin by examining where the gap method places the bars in the sample galaxies relative to the main resonances. For the 50 (rR) cases in the combined GZ2/CSRG samples, Table 6 shows that  $\langle a_{bar}/r_{CR} \rangle = 0.65 \pm 0.02$  with a standard deviation of 0.12. Thus, the bars are predicted to lie on average well inside the CR radius. If we consider instead the ratio of the bar radius to the radius of the inner 4:1 resonance, the sample gives  $\langle a_{bar}/r_{I4R} \rangle = 1.01 \pm 0.03$  with a standard deviation of 0.19. The gap method therefore has the bars in the (rR) dark-spacer sample ending very close to the inner 4:1 resonance, on average.

The reciprocal of  $\langle a_{bar}/r_{CR} \rangle$  is the parameter  $\mathcal{R}$ , which was studied by Debattista & Sellwood (2000) who suggested that  $\mathcal{R} = 1.4$  divides bars into “fast” and “slow” types. For the sample analyzed here,  $\langle \mathcal{R} \rangle = 1.58 \pm 0.04$  with a standard deviation  $\sigma_1 = 0.28$ . Thus, the gap method as applied in this paper favours the apparent bars of OLR subclass galaxies to be relatively slow. This differs from other pattern speed studies (e.g., Rautiainen et al. 2008; Buta & Zhang 2009) which favour fast bars over slow bars. The only way for the gap method to give lower values of  $\mathcal{R}$  is for the bar radius to be defined as something larger than it appears to be, e.g., by including the full extent of the oval the bars are typically imbedded within.



Contopoulos (1980) used orbit theory of barred galaxies to conclude that a bar cannot extend beyond its CR radius. This is because the main periodic orbits supporting the elongated shape of the bar belong to the  $x_1$  family, all members of which lie inside the CR radius. Outside the CR radius, the main periodic orbits are aligned perpendicular to the bar (Contopoulos & Grosbol 1989). Also, Contopoulos (1985) concluded that one of the main limiting factors for the extent of bars is stochasticity of orbits of the  $x_1$  family. He concluded that bars could extend all the way to the CR radius until limited by such effects.

Contopoulos (1988) examined the inner 4:1 resonance in more detail but did not specifically link the ends of bars with the location of this resonance, only noting that 4:1 resonant orbits become increasingly more elongated as the resonance is approached. However, Contopoulos (1985) concluded that strong spirals end at the inner 4:1 resonance, with only weaker spirals extending to the CR radius.

### 8.1.2 Rings

For the OLR subclass rings, we have a few theoretical values to compare with our observed ratios:

1.  $R_1$  outer rings are aligned perpendicular to the bar and have  $a/r_{OLR} \approx 1$ . Such rings should be mostly within  $r_{OLR}$  (Schwarz 1981).
2.  $R'_2$  outer pseudorings are aligned parallel to the bar and have  $b/r_{OLR} \approx 1$ . Such rings should be mostly outside  $r_{OLR}$  (Schwarz 1981).
3. The average radius of an inner ring  $\approx r_{I4R}$ , but  $a/r_{CR} \leq 1$  (Simkin, Su & Schwarz 1980). Inner rings should be aligned parallel to the bar.

Table 8 summarizes the results for 36  $R_1$  and  $R'_1$  rings. These are found to have  $\langle a/r_{OLR} \rangle = 0.85 \pm 0.01$ , with a standard deviation of 0.05, significantly less than the expected value of 1.0. The mean ratios in columns 6 and 7 show that  $R_1$  and  $R'_1$  rings may be linked instead to the outer 4:1 resonance: the values “straddle” the outer 4:1 resonance in the sense that the major axis radii of these features are 9% larger than  $r_{O4R}$  and the minor axis radii are 10% smaller than  $r_{O4R}$ , on average. If we set  $r^* = \sqrt{ab}$ , the geometric mean radius, then  $\langle r^*/r_{O4R} \rangle = 0.99$ . Consistent with Schwarz (1981),  $R_1$  and  $R'_1$  rings lie entirely within the OLR radius, but their association with the outer 4:1 resonance was not predicted by Schwarz.

Table 9 summarizes the results for 25  $R'_2$  outer pseudorings. The mean ratios are  $\langle a/r_{OLR} \rangle = 1.08 \pm 0.01$  and  $\langle b/r_{OLR} \rangle = 1.00 \pm 0.01$ , with standard deviations of 0.07 and 0.06, respectively. Consistent with Schwarz (1981), the minor axis radii of these features are thus located closest to the OLR radius, and the features on the whole are outside the OLR radius.

Table 10 summarizes the results for the various inner features in the (rR) dark-spacer galaxies. The table lists 50 features, but only 47 galaxies are represented since three have double inner features. Cols. 5 and 6 show that inner features straddle the inner 4:1 resonance, an interpretation consistent with Schwarz (1984a) and Simkin, Su, & Schwarz (1980). The geometric mean radius of these features has on average  $\langle r^*/r_{I4R} \rangle = 0.91$ . However, the standard deviations of the ratios, 0.19 for  $a/r_{I4R}$  and 0.15 for  $b/r_{I4R}$ , reflects in part the wide range of intrinsic shapes of inner features.

Two other points of comparison between the (rR) dark-spacer sample galaxies and previous studies are the average minor-to-major axis ratios and relative bar/ring position angles of the different features. The deprojected values of these parameters are listed in the last two columns of Tables 8–10. It is important to note that the projected shapes of the rings themselves were not used to deproject the galaxies, only faint outer isophotes. The results show that  $R'_2$  outer pseudorings in the sample have a mean axis ratio of  $0.93 \pm 0.01$  and a mean bar-ring position angle of  $27^\circ 2 \pm 5^\circ 1$ . The standard deviation of the angle is large,  $25^\circ 4$ , but some of this is simply due to the difficulty of measuring major axis position angles when the feature is nearly circular.

For  $R_1$  and  $R'_1$  outer rings, the mean axis ratio is  $0.84 \pm 0.01$  and the mean bar/ring position angle is  $81^\circ 3 \pm 1^\circ 3$ , the latter with a standard deviation of  $7^\circ 6$ . Thus, these features deproject to a large angle to the bar, nearly perpendicular on average, and are more elongated intrinsically than are  $R'_2$  rings.

For the inner features in the sample, the average axis ratio and bar/ring position angle are  $0.72 \pm 0.02$  and  $7^\circ 5 \pm 2^\circ 0$ , respectively. Both parameters have large standard deviations: 0.12 for the axis ratio and  $13^\circ 9$  for the bar/ring position angle. Thus, inner features have the most elongated intrinsic shapes of all the rings in the sample. Subtle misalignments between bars and inner features, such as that seen in NGC 5132, are likely to be significant as a result.

These shape and alignment results are consistent with the predictions of Schwarz (1981, 1984a), and with previous studies of the shapes and orientations of galactic rings (Buta 1995; Comerón et al. 2014).

## 8.2 (r) dark-spacers

In contrast to the (rR) dark-spacers, Table 7 shows that under the same assumption about the nature of the dark gaps, the four (r) dark-spacers in the sample have  $\langle a_{bar}/r_{CR} \rangle = 1.44 \pm 0.10$  and  $\langle a_{bar}/r_{I4R} \rangle = 2.23 \pm 0.16$ , values that are higher by more than a factor of 2 than the means for (rR) dark-spacers. This shows that if the dark spaces in galaxies having  $R_1$  and  $R_2$  features and those in galaxies like NGC 5335, which lack such features, are viewed in the same manner, then the bars in (r) dark-spacers extend well beyond their CR radius, violating the rules established by Contopoulos (1980, 1985) which state that bars cannot extend beyond their CR radius. The fact that there is no outer ring in the outer disks of the four (r) dark-spacers studied here could indicate that no major even-order resonances exist in those regions. For example, most of the spiral structure in NGC 5335 would lie beyond its implied OLR radius from the gap method. Other aspects of (r) dark-spacers are discussed in section 10.2.

## 9 GAP COLOURS

The gap method assumes that dark spaces like those seen in (rR) dark-spacers are dynamical phenomena, not artifacts of an unusual dust distribution. To examine further the nature of dark gaps, the integrated colours of each sample galaxy were derived at four points, two within the dark gaps at the presumed  $L_4$  and  $L_5$  points, and two along the bar axis at



**Table 8.**  $R_1$  and  $R'_1$  Outer Rings and Pseudorings. Col. 1: galaxy name; col. 2: feature type; cols. 3,4: deprojected major and minor axis ring dimensions, respectively, in arcseconds; cols. 5-7: ratios of ring dimensions to outer 4:1 and outer Lindblad resonance radii; col. 8: deprojected ring minor to major axis ratio; col. 9: deprojected relative angle between the bar and the major axis of the ring.

| Name<br>1   | Feature<br>2 | $a$<br>3 | $b$<br>4 | $a/r_{OLR}$<br>5 | $a/r_{O4R}$<br>6 | $b/r_{O4R}$<br>7 | $q_0$<br>8 | $ \theta_{Bf} $<br>9 |
|-------------|--------------|----------|----------|------------------|------------------|------------------|------------|----------------------|
| CGCG 8-10   | $R_1$        | 32.5     | 25.7     | 0.87             | 1.10             | 0.87             | 0.79       | 84.4                 |
| CGCG 65-2   | $R_1$        | 17.6     | 14.5     | 0.80             | 1.01             | 0.83             | 0.82       | 89.6                 |
| CGCG 73-53  | $R_1$        | 15.6     | 11.7     | 0.88             | 1.11             | 0.83             | 0.75       | 89.3                 |
| CGCG 185-14 | $R_1$        | 16.9     | 13.7     | 0.87             | 1.09             | 0.88             | 0.81       | 82.1                 |
| CGCG 263-22 | $R'_1$       | 29.1     | 27.3     | 0.78             | 0.98             | 0.92             | 0.94       | 57.4                 |
| ESO 365-35  | $R_1$        | 31.2     | 23.8     | 0.88             | 1.11             | 0.84             | 0.76       | 85.3                 |
| ESO 426-2   | $R_1$        | 34.8     | 28.5     | 0.92             | 1.16             | 0.95             | 0.82       | 86.6                 |
| ESO 437-33  | $R'_1$       | 33.0     | 26.7     | 0.82             | 1.03             | 0.83             | 0.81       | 76.6                 |
| ESO 437-67  | $R'_1$       | 78.4     | 72.3     | 0.85             | 1.07             | 0.99             | 0.92       | 83.6                 |
| ESO 575-47  | $R'_1$       | 49.0     | 43.1     | 0.78             | 0.98             | 0.87             | 0.88       | 89.1                 |
| IC 1438     | $R_1$        | 50.9     | 41.6     | 0.89             | 1.13             | 0.92             | 0.82       | 82.7                 |
| IC 2473     | $R'_1$       | 52.2     | 47.8     | 0.87             | 1.09             | 1.00             | 0.92       | 65.8                 |
| IC 2628     | $R_1$        | 15.1     | 11.9     | 0.88             | 1.11             | 0.87             | 0.79       | 77.8                 |
| IC 4214     | $R_1$        | 63.4     | 54.8     | 0.80             | 1.01             | 0.88             | 0.86       | 88.5                 |
| MCG 6-32-24 | $R_1$        | 16.6     | 13.7     | 0.83             | 1.05             | 0.87             | 0.83       | 69.6                 |
| MCG 7-18-40 | $R'_1$       | 13.0     | 8.5      | 1.01             | 1.27             | 0.83             | 0.65       | 79.2                 |
| NGC 210     | $R_1$        | 93.6     | 73.6     | 0.91             | 1.15             | 0.90             | 0.79       | 88.3                 |
| NGC 1079    | $R_1$        | 114.1    | 104.5    | 0.80             | 1.01             | 0.92             | 0.92       | 86.8                 |
| NGC 1291    | $R_1$        | 249.3    | 218.9    | 0.83             | 1.05             | 0.92             | 0.88       | 84.4                 |
| NGC 1326    | $R_1$        | 86.5     | 76.4     | 0.81             | 1.02             | 0.90             | 0.88       | 79.0                 |
| NGC 1398    | $R_1$        | 110.6    | 90.1     | 0.73             | 0.92             | 0.75             | 0.81       | 83.2                 |
| NGC 1433    | $R'_1$       | 190.8    | 167.7    | 0.84             | 1.06             | 0.93             | 0.88       | 78.9                 |
| NGC 2665    | $R_1$        | 58.3     | 51.2     | 0.80             | 1.01             | 0.89             | 0.88       | 81.6                 |
| NGC 2766    | $R_1$        | 30.6     | 28.4     | 0.84             | 1.06             | 0.99             | 0.93       | 81.0                 |
| NGC 3081    | $R_1$        | 79.1     | 66.1     | 0.78             | 0.99             | 0.83             | 0.84       | 84.4                 |
| NGC 4113    | $R'_1$       | 35.1     | 28.6     | 0.85             | 1.08             | 0.88             | 0.82       | 80.4                 |
| NGC 5132    | $R_1$        | 61.4     | 56.4     | 0.86             | 1.08             | 0.99             | 0.92       | 69.4                 |
| NGC 5701    | $R_1$        | 104.6    | 88.0     | 0.88             | 1.11             | 0.93             | 0.84       | 87.6                 |
| NGC 6782    | $R'_1$       | 65.1     | 49.0     | 0.86             | 1.08             | 0.81             | 0.75       | 78.4                 |
| NGC 7098    | $R_1$        | 113.4    | 103.7    | 0.77             | 0.96             | 0.88             | 0.91       | 88.2                 |
| PGC 54897   | $R'_1$       | 24.4     | 20.1     | 0.81             | 1.02             | 0.84             | 0.82       | 83.1                 |
| PGC 1857116 | $R'_1$       | 23.8     | 20.7     | 0.91             | 1.14             | 1.00             | 0.87       | 73.2                 |
| UGC 4596    | $R_1$        | 25.4     | 20.7     | 0.85             | 1.07             | 0.88             | 0.82       | 84.7                 |
| UGC 5885    | $R'_1$       | 40.0     | 33.1     | 0.91             | 1.15             | 0.95             | 0.83       | 87.0                 |
| UGC 10168   | $R_1$        | 42.6     | 34.9     | 0.91             | 1.15             | 0.94             | 0.82       | 68.3                 |
| UGC 12646   | $R'_1$       | 48.6     | 41.8     | 0.88             | 1.11             | 0.96             | 0.86       | 89.6                 |
| mean        |              | .....    | .....    | 0.85             | 1.07             | 0.90             | 0.84       | 81.3                 |
| mean error  |              | .....    | .....    | 0.01             | 0.01             | 0.01             | 0.01       | 1.3                  |
| $\sigma_1$  |              | .....    | .....    | 0.05             | 0.07             | 0.06             | 0.06       | 7.6                  |
| $N$         |              | .....    | .....    | 36               | 36               | 36               | 36         | 36                   |

the same radius. The fluxes were integrated at these points within small circular apertures having sizes chosen to be approximately the apparent width of the gap. Each pair was combined to give average colours. The results, corrected for galactic extinction values from NED, are listed in Tables 11–13. These tables also give the radius of the circular aperture used for the integrations. The mean gap and bar axis point colours are summarized in Table 14. The combination of the GZ2 and CSRG samples allows us to derive this information in both the SDSS *ugri* system and in the Johnson-Cousins *BVI* system.

Figure 15 shows the resulting colour-colour plots  $(g-r)_o$  versus  $(r-i)_o$  and  $(u-g)_o$  versus  $(g-i)_o$  for the GZ2 galaxies, while Figure 16 shows  $(B-V)_o$  versus  $(V-I)_o$  for the non-GZ2 cases. The left panel in each pair shows the mean gap/bar colour points from Table 14 while the right panel

shows the same plot for the integrated colours of the galaxies from Tables 3 and 4 (open triangles). For comparison, each plot shows the mean colour-colour relation for normal galaxies of different types. For SDSS filters, the mean relation shown is from Shimasaku et al. (2001). For *BVI* filters, the relation shown is from Buta et al. (1994) and Buta & Williams (1995). All colours are corrected for Galactic extinction. The graphs show first that the total colours of the sample galaxies cluster around the redder half of the normal galaxy sequence, consistent with spirals of early-to-intermediate types. The graphs also show that the distribution of the points is nearly parallel to the reddening vector in each case, making it difficult to separate the effects of stellar population differences from reddening effects.

Figures 15 and 16 show that for all of the colours measured, the gap points are redder than the bar axis points.

**Table 9.**  $R_2$  and  $R'_2$  Outer Rings and Pseudorings. Col. 1: galaxy name; col. 2: feature type; cols. 3,4: deprojected major and minor axis ring dimensions, respectively, in arcseconds; cols. 5-6: ratios of ring dimensions to outer Lindblad resonance radii; col. 7: deprojected ring minor to major axis ratio; col. 8: deprojected relative angle between the bar and the major axis of the ring.

| Name<br>1   | Feature<br>2 | $a$<br>3 | $b$<br>4 | $a/r_{OLR}$<br>5 | $b/r_{OLR}$<br>6 | $q_0$<br>7 | $ \theta_{Bf} $<br>8 |
|-------------|--------------|----------|----------|------------------|------------------|------------|----------------------|
| CGCG 8-10   | $R'_2$       | 36.4     | 33.7     | 0.97             | 0.90             | 0.93       | 11.4                 |
| CGCG 13-75  | $R'_2$       | 23.8     | 22.0     | 1.10             | 1.02             | 0.93       | 73.8                 |
| CGCG 73-53  | $R_2$        | 17.0     | 16.7     | 0.96             | 0.95             | 0.98       | 3.7                  |
| CGCG 185-14 | $R'_2$       | 20.6     | 20.0     | 1.06             | 1.03             | 0.97       | 18.0                 |
| ESO 325-28  | $R'_2$       | 33.1     | 32.2     | 1.10             | 1.07             | 0.97       | 26.8                 |
| ESO 365-35  | $R'_2$       | 36.7     | 32.4     | 1.04             | 0.91             | 0.88       | 11.0                 |
| ESO 426-2   | $R'_2$       | 43.4     | 40.9     | 1.15             | 1.08             | 0.94       | 19.1                 |
| ESO 437-33  | $R'_2$       | 41.2     | 38.3     | 1.02             | 0.95             | 0.93       | 10.1                 |
| IC 1438     | $R'_2$       | 65.2     | 61.3     | 1.15             | 1.08             | 0.94       | 30.8                 |
| IC 2628     | $R'_2$       | 18.9     | 17.1     | 1.10             | 1.00             | 0.91       | 29.3                 |
| MCG 7-18-40 | $R'_2$       | 13.8     | 13.1     | 1.07             | 1.01             | 0.94       | 47.6                 |
| NGC 210     | $R'_2$       | 128.4    | 112.9    | 1.25             | 1.10             | 0.88       | 5.3                  |
| NGC 1079    | $R'_2$       | 162.9    | 151.5    | 1.14             | 1.06             | 0.93       | 10.1                 |
| NGC 1291    | $R'_2$       | 306.6    | 299.6    | 1.03             | 1.00             | 0.98       | 88.8                 |
| NGC 2766    | $R'_2$       | 40.7     | 36.5     | 1.12             | 1.01             | 0.90       | 0.4                  |
| NGC 3081    | $R'_2$       | 104.1    | 96.4     | 1.03             | 0.96             | 0.93       | 3.2                  |
| NGC 4935    | $R'_2$       | 29.6     | 27.6     | 1.02             | 0.95             | 0.93       | 0.1                  |
| NGC 5211    | $R'_2$       | 59.4     | 51.5     | 1.00             | 0.86             | 0.87       | 11.2                 |
| NGC 5701    | $R'_2$       | 125.5    | 120.4    | 1.06             | 1.01             | 0.96       | 18.9                 |
| NGC 7098    | $R'_2$       | 153.6    | 144.0    | 1.04             | 0.97             | 0.94       | 58.1                 |
| UGC 4596    | $R'_2$       | 33.6     | 31.5     | 1.13             | 1.06             | 0.94       | 41.3                 |
| UGC 4771    | $R'_2$       | 31.6     | 27.2     | 1.02             | 0.88             | 0.86       | 33.9                 |
| UGC 9418    | $R'_2$       | 27.5     | 26.4     | 1.10             | 1.05             | 0.96       | 79.7                 |
| UGC 10168   | $R'_2$       | 49.9     | 46.7     | 1.07             | 1.00             | 0.94       | 39.8                 |
| UGC 10712   | $R'_2$       | 23.0     | 19.5     | 1.17             | 0.99             | 0.85       | 7.4                  |
| means       |              | .....    | .....    | 1.08             | 1.00             | 0.93       | 27.2                 |
| mean error  |              | .....    | .....    | 0.01             | 0.01             | 0.01       | 5.1                  |
| $\sigma_1$  |              | .....    | .....    | 0.07             | 0.06             | 0.04       | 25.4                 |
| $N$         |              | .....    | .....    | 25               | 25               | 25         | 25                   |

However, the difference amounts to only  $\approx 0.1$  mag on average (Table 14). To evaluate what such a difference might mean, the CSRG *BVI* colours are compared in Figure 16 with the colours of synthetic galaxies (thin solid curves) calculated by Kennicutt et al. (1994). The latter are based on models having an age of 10 Gyr and a star formation rate that declines exponentially with an e-folding time  $\tau$ . The models are also characterized by a birthrate parameter, which is the current star formation rate relative to the past average, and an initial mass function (IMF), of which three different versions were used.

Irrespective of the IMF used, the comparison with the synthetic galaxies suggests that dark gaps are made of a stellar population with an e-folding time  $\tau$  approximately 1 Gyr less than for the bar axis points, implying a more rapidly declining star formation rate for the gap regions. This basically means that recent star formation is not a characteristic of dark gaps. Even if the rings and pseudorings have considerable star formation, the gaps tend to be devoid of such activity. This supports the idea that dark gaps are a purely stellar dynamical phenomenon, and that the colour difference between the gaps and the bar axis points is due mainly to stellar population differences, not to extinction. Examination of colour index maps of all of the sample galaxies do not show any evidence that recent star formation is ever found in the gaps of (rR)- or (r) dark-spacer galaxies. BC96

note: “When the bar is strong, most orbits perpendicular to the bar between CR and OLR become unstable. That is why this region is often depopulated and, in real galaxies, never includes recent star formation.”

## 10 DISCUSSION

### 10.1 Comparison with Manifold Theory

The outer ring/pseudoring subclasses  $R_1$ ,  $R'_1$ , and  $R'_2$  are remarkable not only because of their distinctive shapes, but also because they were predicted to exist before they were actually found. The early models of the gas flow in barred galaxies by Schwarz (1981, 1984a) showed that features resembling these morphologies can develop naturally in response to a bar perturbation. The implication of these models is that gas in a barred galaxy accumulates near resonances, under the continuous action of gravity torques from the bar pattern (BC96). On the basis of these models, the link of the  $R_1$ ,  $R'_1$ , and  $R'_2$  features to outer resonances like the O4R and the OLR seems strong, especially when the combined morphology,  $R_1R'_2$ , is added to the mix of types. Being able to recognize these features in real galaxies provides a direct link between morphology and dynamics, which makes further studies of these galaxies imperative as a stepping stone to understanding other galactic morphologies.

**Table 10.** Inner Rings, Pseudorings, Lenses, Ring-Lenses, and Pseudoring-Lenses. Col. 1: galaxy name; col. 2: type of feature (r=inner ring, rs=inner pseudoring, rl=inner ring-lens, r'l = inner pseudoring-lens, r<sub>i</sub>=inner-most of two inner rings, r<sub>o</sub>=outer-most of two inner rings; l=inner lens); cols. 3,4: deprojected major and minor axis ring dimensions, respectively, in arcseconds; cols. 5-6: ratios of ring dimensions to the inner 4:1 resonance radius; col. 7: feature minor-to-major axis ratio; col. 8: relative deprojected angle between the bar major axis and the major axis position angle of the feature.

| Name<br>1      | Feature<br>2    | <i>a</i><br>3 | <i>b</i><br>4 | <i>a</i> / <i>r</i> <sub>14R</sub><br>5 | <i>b</i> / <i>r</i> <sub>14R</sub><br>6 | <i>q</i> <sub>0</sub><br>7 | <i>θ</i> <sub>Bf</sub>  <br>8 |
|----------------|-----------------|---------------|---------------|---|---|----------------------------|-------------------------------|
| CGCG 8-10      | r               | 13.0          | 10.1          | 0.92                                    | 0.71                                    | 0.77                       | 8.7                           |
| CGCG 13-75     | r'l             | 8.0           | 6.1           | 0.98                                    | 0.75                                    | 0.77                       | 0.0                           |
| CGCG 65-2      | rs              | 11.5          | 6.9           | 1.38                                    | 0.83                                    | 0.60                       | 5.8                           |
| CGCG 73-53     | l               | 8.1           | 6.8           | 1.22                                    | 1.01                                    | 0.83                       | 3.4                           |
| CGCG 185-14    | rs              | 7.8           | 6.8           | 1.05                                    | 0.93                                    | 0.88                       | 11.1                          |
| CGCG 263-22    | rs <sub>i</sub> | 14.5          | 11.1          | 1.02                                    | 0.78                                    | 0.77                       | 87.0                          |
| CGCG 263-22    | rs <sub>o</sub> | 20.8          | 14.5          | 1.47                                    | 1.02                                    | 0.70                       | 0.8                           |
| ESO 325-28     | r               | 13.3          | 8.3           | 1.17                                    | 0.73                                    | 0.62                       | 3.7                           |
| ESO 365-35     | l               | 14.0          | 11.9          | 1.04                                    | 0.89                                    | 0.85                       | 2.5                           |
| ESO 426-2      | r               | 17.4          | 11.4          | 1.22                                    | 0.80                                    | 0.65                       | 3.1                           |
| ESO 437-33     | rs              | 14.2          | 9.7           | 0.93                                    | 0.64                                    | 0.68                       | 0.7                           |
| ESO 437-67     | rs              | 41.6          | 26.0          | 1.19                                    | 0.75                                    | 0.62                       | 2.3                           |
| ESO 566-24     | r               | 18.6          | 14.4          | 1.08                                    | 0.84                                    | 0.78                       | 6.7                           |
| ESO 575-47     | rs              | 29.3          | 19.6          | 1.23                                    | 0.83                                    | 0.67                       | 2.5                           |
| IC 1223        | rs <sub>i</sub> | 13.7          | 11.5          | 0.94                                    | 0.79                                    | 0.84                       | 16.2                          |
| IC 1223        | rs <sub>o</sub> | 18.9          | 16.0          | 1.30                                    | 1.10                                    | 0.84                       | 5.7                           |
| IC 1438        | r               | 22.3          | 15.0          | 1.03                                    | 0.69                                    | 0.67                       | 1.3                           |
| IC 2473        | r               | 26.7          | 17.8          | 1.17                                    | 0.78                                    | 0.67                       | 9.4                           |
| IC 4214        | rs              | 30.6          | 19.9          | 1.03                                    | 0.67                                    | 0.65                       | 4.2                           |
| MCG 6-32-24    | r               | 8.4           | 5.3           | 1.11                                    | 0.70                                    | 0.63                       | 0.0                           |
| MCG 7-18-40    | rl              | 5.3           | 4.2           | 1.09                                    | 0.86                                    | 0.79                       | 1.9                           |
| NGC 210        | rs              | 32.4          | 20.4          | 0.83                                    | 0.52                                    | 0.63                       | 1.4                           |
| NGC 1079       | r'l             | 45.4          | 37.9          | 0.84                                    | 0.70                                    | 0.84                       | 14.2                          |
| NGC 1291       | l               | 140.1         | 111.4         | 1.24                                    | 0.98                                    | 0.80                       | 3.5                           |
| NGC 1326       | r               | 43.3          | 30.7          | 1.07                                    | 0.76                                    | 0.71                       | 1.8                           |
| NGC 1398       | rs              | 58.7          | 54.4          | 1.02                                    | 0.95                                    | 0.93                       | 18.4                          |
| NGC 1433       | r               | 103.8         | 71.0          | 1.21                                    | 0.83                                    | 0.68                       | 1.9                           |
| NGC 2665       | rs              | 34.9          | 18.0          | 1.27                                    | 0.66                                    | 0.52                       | 4.9                           |
| NGC 2766       | r               | 16.5          | 12.3          | 1.20                                    | 0.89                                    | 0.74                       | 2.9                           |
| NGC 3081       | r               | 35.3          | 24.8          | 0.92                                    | 0.65                                    | 0.70                       | 1.1                           |
| NGC 3380       | rs              | 20.4          | 11.1          | 1.00                                    | 0.54                                    | 0.54                       | 2.6                           |
| NGC 4113       | rs              | 20.9          | 9.9           | 1.34                                    | 0.64                                    | 0.48                       | 8.3                           |
| NGC 4736       | rs              | 50.6          | 42.7          | 0.32                                    | 0.27                                    | 0.84                       | 49.9                          |
| NGC 4935       | rs              | 11.2          | 7.7           | 1.02                                    | 0.70                                    | 0.69                       | 13.3                          |
| NGC 5132       | rs              | 38.4          | 24.1          | 1.41                                    | 0.89                                    | 0.63                       | 0.7                           |
| NGC 5211       | rs              | 18.9          | 15.2          | 0.84                                    | 0.67                                    | 0.80                       | 2.1                           |
| NGC 5370       | r               | 19.3          | 17.9          | 0.94                                    | 0.87                                    | 0.93                       | 16.2                          |
| NGC 5701       | l               | 42.5          | 37.9          | 0.94                                    | 0.84                                    | 0.89                       | 5.4                           |
| NGC 6782       | r               | 27.6          | 17.6          | 0.96                                    | 0.61                                    | 0.64                       | 4.1                           |
| NGC 7098       | rs              | 69.1          | 58.6          | 1.23                                    | 1.04                                    | 0.85                       | 1.9                           |
| PGC 54897      | r'l             | 10.1          | 6.0           | 0.88                                    | 0.52                                    | 0.59                       | 6.0                           |
| PGC 1857116    | rs              | 11.5          | 6.5           | 1.16                                    | 0.65                                    | 0.56                       | 2.4                           |
| UGC 4596       | r <sub>i</sub>  | 9.4           | 8.5           | 0.83                                    | 0.75                                    | 0.90                       | 9.6                           |
| UGC 4596       | r <sub>o</sub>  | 14.1          | 11.2          | 1.25                                    | 0.99                                    | 0.80                       | 2.6                           |
| UGC 4771       | l               | 12.9          | 8.7           | 1.10                                    | 0.74                                    | 0.67                       | 3.1                           |
| UGC 5885       | r               | 21.8          | 11.3          | 1.31                                    | 0.68                                    | 0.52                       | 0.0                           |
| UGC 9418       | rl              | 9.8           | 6.1           | 1.03                                    | 0.64                                    | 0.62                       | 0.3                           |
| UGC 10168      | r'l             | 16.0          | 13.1          | 0.90                                    | 0.74                                    | 0.82                       | 11.3                          |
| UGC 10712      | rl              | 8.1           | 6.2           | 1.09                                    | 0.83                                    | 0.76                       | 0.7                           |
| UGC 12646      | r               | 23.4          | 13.9          | 1.12                                    | 0.67                                    | 0.60                       | 5.5                           |
| means          |                 | .....         | .....         | 1.08                                    | 0.77                                    | 0.72                       | 7.5                           |
| mean error     |                 | .....         | .....         | 0.03                                    | 0.02                                    | 0.02                       | 2.0                           |
| σ <sub>l</sub> |                 | .....         | .....         | 0.19                                    | 0.15                                    | 0.12                       | 13.9                          |
| <i>N</i>       |                 | .....         | .....         | 50                                      | 50                                      | 50                         | 50                            |



**Table 11.** Corrected  $g-r$  and  $r-i$  colours of Gap and Bar Axis Points. Col. 1: galaxy name; cols. 2-3: combined colours of the two gap points at  $r_{gp}$  within a circular aperture of radius  $A$ ; cols. 4-5: combined colours of the two points also at  $r_{gp}$  but along the axis defined by the bar; col. 6: radius of integrating aperture in arcseconds. All colours are corrected for galactic extinction values from NED (Schlafly & Finkbeiner 2011).

| Name        | $(g-r)_o$<br>gap | $(r-i)_o$<br>gap | $(g-r)_o$<br>bar axis | $(r-i)_o$<br>bar axis | A<br>(arcsec) |
|-------------|------------------|------------------|-----------------------|-----------------------|---------------|
| 1           | 2                | 3                | 4                     | 5                     | 6             |
| CGCG 8-10   | 0.91±0.03        | 0.43±0.03        | 0.71±0.02             | 0.41±0.02             | 5.94          |
| CGCG 13-75  | 0.68±0.04        | 0.53±0.03        | 0.58±0.02             | 0.39±0.02             | 1.98          |
| CGCG 65-2   | 0.64±0.04        | 0.43±0.03        | 0.44±0.02             | 0.27±0.02             | 1.98          |
| CGCG 67-4   | 0.88±0.05        | 0.36±0.05        | 0.55±0.03             | 0.28±0.03             | 1.98          |
| CGCG 73-53  | 0.74±0.04        | 0.41±0.03        | 0.68±0.03             | 0.34±0.02             | 1.98          |
| CGCG 185-14 | 0.67±0.03        | 0.38±0.02        | 0.58±0.02             | 0.34±0.02             | 1.98          |
| CGCG 263-22 | 0.75±0.05        | 0.70±0.04        | 0.66±0.02             | 0.42±0.02             | 2.97          |
| IC 1223     | 0.87±0.03        | 0.51±0.02        | 0.73±0.02             | 0.41±0.02             | 3.96          |
| IC 2473     | 0.71±0.02        | 0.34±0.02        | 0.46±0.01             | 0.26±0.01             | 7.92          |
| IC 2628     | 0.70±0.03        | 0.38±0.03        | 0.68±0.03             | 0.33±0.02             | 1.98          |
| MCG 6-32-24 | 0.66±0.04        | 0.42±0.03        | 0.64±0.02             | 0.28±0.02             | 1.98          |
| MCG 7-18-40 | 0.68±0.03        | 0.38±0.03        | 0.57±0.02             | 0.34±0.02             | 1.98          |
| NGC 2766    | 0.70±0.02        | 0.40±0.02        | 0.61±0.02             | 0.32±0.01             | 2.97          |
| NGC 3380    | 0.62±0.01        | 0.46±0.01        | 0.63±0.01             | 0.36±0.01             | 5.94          |
| NGC 4113    | 0.48±0.10        | 0.25±0.10        | 0.43±0.03             | 0.24±0.03             | 1.98          |
| NGC 4608    | 0.73±0.01        | 0.41±0.01        | 0.77±0.01             | 0.42±0.01             | 3.96          |
| NGC 4935    | 0.62±0.02        | 0.40±0.02        | 0.52±0.01             | 0.32±0.01             | 2.97          |
| NGC 5132    | 0.79±0.02        | 0.47±0.02        | 0.70±0.01             | 0.35±0.01             | 7.92          |
| NGC 5211    | 0.67±0.02        | 0.39±0.02        | 0.62±0.02             | 0.32±0.01             | 3.96          |
| NGC 5335    | 0.81±0.04        | 0.54±0.03        | 0.79±0.01             | 0.41±0.01             | 1.98          |
| NGC 5370    | 0.76±0.02        | 0.44±0.02        | 0.68±0.02             | 0.42±0.02             | 3.96          |
| NGC 5686    | 0.72±0.01        | 0.35±0.01        | 0.73±0.01             | 0.34±0.01             | 1.58          |
| NGC 5701    | 0.64±0.01        | 0.47±0.01        | 0.60±0.01             | 0.42±0.01             | 7.92          |
| PGC 54897   | 0.51±0.04        | 0.53±0.03        | 0.59±0.02             | 0.35±0.02             | 2.97          |
| PGC 1857116 | 0.87±0.04        | 0.34±0.04        | 0.57±0.02             | 0.34±0.02             | 3.96          |
| PGC 2570478 | 0.89±0.05        | 0.42±0.04        | 0.88±0.04             | 0.40±0.03             | 1.98          |
| UGC 4596    | 0.80±0.04        | 0.59±0.04        | 0.59±0.02             | 0.34±0.02             | 2.97          |
| UGC 4771    | 0.69±0.02        | 0.38±0.02        | 0.62±0.02             | 0.41±0.02             | 3.96          |
| UGC 5380    | 0.74±0.02        | 0.41±0.02        | 0.80±0.01             | 0.39±0.01             | 1.98          |
| UGC 5885    | 0.73±0.05        | 0.38±0.04        | 0.58±0.02             | 0.35±0.02             | 3.96          |
| UGC 9418    | 0.65±0.05        | 0.49±0.04        | 0.67±0.03             | 0.36±0.03             | 1.98          |
| UGC 10168   | 0.75±0.04        | 0.46±0.04        | 0.69±0.03             | 0.40±0.02             | 2.97          |
| UGC 10712   | 0.79±0.04        | 0.37±0.04        | 0.64±0.03             | 0.34±0.03             | 1.98          |

The analysis in this paper has shown that there is considerable homogeneity in the structure of outer resonant subclass galaxies. Many show characteristic double-humped azimuthally-averaged surface brightness profiles (Figure 21), and the ring features have characteristic intrinsic shapes and orientations with respect to bars and ovals (highlighted by the schematics in Figure 13). Dark gaps are a common theme in these galaxies, and this study has shown that linking these gaps to the corotation resonance provides consistent interpretations of the structure of these galaxies in terms of characteristic low-order bisymmetric resonances. This consistency suggests that the bars and the ring patterns by and large share the same pattern speed. This does not, however, mean that multiple pattern speeds are not present in these galaxies. Our analysis, for example, does not consider the role of the ILR in the structure of these galaxies.

Although the resonant idea seems to explain many of the features of the galaxies studied in this paper, the alternative “manifold theory” (Romero-Gómez et al. 2006, 2007; Athanassoula et al. 2009a,b; 2010) also can account for the  $R_1$ ,  $R'_1$ ,  $R'_2$ , and  $R_1R'_2$  morphologies. Rather than linking

these features to specific bisymmetric resonances, manifold theory is based around the behavior of particles in the vicinity of the  $L_1$  and  $L_2$  Lagrangian points of the bar gravitational potential. These points are located near the ends of the bar, and like the  $L_4$  and  $L_5$  points, have characteristic periodic orbits around them. Because  $L_1$  and  $L_2$  are saddle points in the effective potential, the periodic orbits around the points are generally unstable and chaotic, which would lead to a deficiency of light in these regions were it not for the existence of manifold tubes that confine the chaotic motions along specific trajectories called homoclinic and heteroclinic orbits. These orbits can account not only for the  $R_1$ ,  $R'_1$ ,  $R'_2$ , and  $R_1R'_2$  morphologies, but also  $rR_1$  morphologies consisting of a cuspy, elongated inner ring oriented perpendicular to a dimpled  $R_1$  outer ring, as well as pure spiral morphologies.

Of the sample of galaxies examined here, several with strong  $R_1$  components resemble the homoclinic manifold models, where particles emanate from the vicinity of  $L_1$  or  $L_2$ , and approach the opposite point at the other end of the bar. For example, the schematics of NGC 2665, ESO 437-67, NGC 6782, UGC 5885, and UGC 12646 in Figure 13

**Table 12.** Corrected  $u-g$  and  $g-i$  colours of Gap and Bar Axis Points. Col. 1: galaxy name; cols. 2-3: combined colours of the two gap points at  $r_{gp}$  within a circular aperture of radius  $A$ ; cols. 4-5: combined colours of the two points also at  $r_{gp}$  but along the axis defined by the bar; col. 6: radius of integrating aperture in arcseconds. All colours are corrected for galactic extinction values from NED (Schlafly & Finkbeiner 2011).

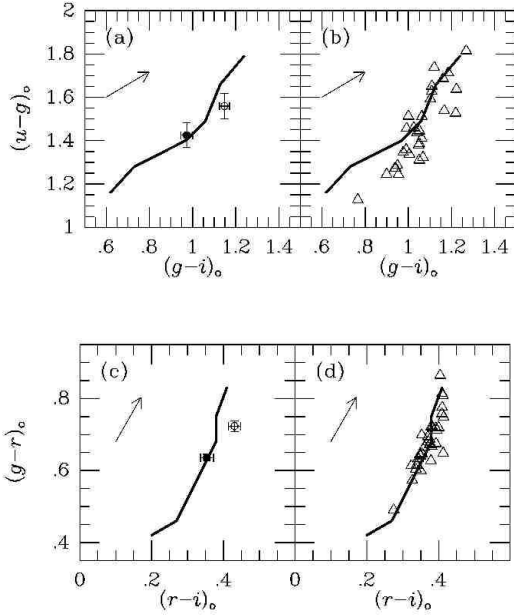
| Name        | $(u-g)_o$<br>gap | $(g-i)_o$<br>gap | $(u-g)_o$<br>bar axis | $(g-i)_o$<br>bar axis | $A$<br>(arcsec) |
|-------------|------------------|------------------|-----------------------|-----------------------|-----------------|
| 1           | 2                | 3                | 4                     | 5                     | 6               |
| CGCG 13-75  | 1.78±0.11        | 1.21±0.04        | 1.39±0.06             | 0.97±0.03             | 1.98            |
| CGCG 65-2   | 1.34±0.10        | 1.08±0.04        | 0.84±0.05             | 0.71±0.02             | 1.98            |
| CGCG 67-4   | 1.32±0.13        | 1.24±0.05        | 1.25±0.06             | 0.83±0.03             | 1.98            |
| CGCG 185-14 | 1.44±0.08        | 1.05±0.03        | 1.23±0.06             | 0.91±0.02             | 1.98            |
| CGCG 263-22 | 1.62±0.12        | 1.44±0.04        | 1.36±0.06             | 1.08±0.02             | 2.97            |
| IC 2473     | 1.70±0.05        | 1.05±0.02        | 1.11±0.02             | 0.72±0.01             | 7.92            |
| IC 2628     | 1.87±0.10        | 1.08±0.03        | 1.34±0.06             | 1.02±0.02             | 1.98            |
| MCG 6-32-24 | 2.36±0.13        | 1.09±0.04        | 1.49±0.06             | 0.92±0.03             | 1.98            |
| MCG 7-18-40 | 1.38±0.08        | 1.06±0.03        | 1.26±0.05             | 0.91±0.02             | 1.98            |
| NGC 2766    | 1.44±0.06        | 1.11±0.02        | 1.34±0.04             | 0.93±0.02             | 2.97            |
| NGC 3380    | 1.57±0.03        | 1.08±0.01        | 1.53±0.02             | 0.99±0.01             | 5.94            |
| NGC 4608    | 1.67±0.04        | 1.13±0.01        | 1.82±0.02             | 1.18±0.01             | 3.96            |
| NGC 4935    | 1.64±0.05        | 1.02±0.02        | 1.28±0.03             | 0.84±0.01             | 2.97            |
| NGC 5211    | 1.49±0.05        | 1.05±0.02        | 1.44±0.04             | 0.95±0.02             | 3.96            |
| NGC 5335    | 1.70±0.11        | 1.35±0.04        | 1.87±0.04             | 1.19±0.01             | 1.98            |
| NGC 5370    | 1.72±0.06        | 1.20±0.02        | 2.05±0.06             | 1.10±0.02             | 3.96            |
| NGC 5686    | 1.58±0.03        | 1.07±0.01        | 1.73±0.03             | 1.07±0.01             | 1.58            |
| NGC 5701    | 1.66±0.03        | 1.10±0.01        | 1.27±0.02             | 1.02±0.01             | 7.92            |
| PGC 54897   | 0.91±0.07        | 1.04±0.03        | 1.50±0.06             | 0.94±0.02             | 2.97            |
| PGC 1857116 | 1.10±0.09        | 1.21±0.04        | 1.27±0.03             | 0.90±0.02             | 3.96            |
| PGC 2570478 | 1.43±0.13        | 1.31±0.04        | 2.02±0.13             | 1.28±0.03             | 1.98            |
| UGC 4596    | 1.51±0.11        | 1.39±0.04        | 1.29±0.04             | 0.93±0.02             | 2.97            |
| UGC 4771    | 1.26±0.06        | 1.07±0.02        | 1.42±0.05             | 1.03±0.02             | 3.96            |
| UGC 5885    | 1.43±0.13        | 1.11±0.05        | 1.25±0.04             | 0.93±0.02             | 3.96            |
| UGC 10712   | 2.05±0.13        | 1.16±0.04        | 1.30±0.06             | 0.98±0.03             | 1.98            |

**Table 13.** Corrected  $B-V$  and  $V-I$  colours of Gap and Bar Axis Points. Col. 1: galaxy name; cols. 2-3: combined colours of the two gap points at  $r_{gp}$  within a circular aperture of radius  $A$ ; cols. 4-5: combined colours of the two points also at  $r_{gp}$  but along the axis defined by the bar; col. 6: radius of integrating aperture in arcseconds. All colours are corrected for galactic extinction values from NED (Schlafly & Finkbeiner 2011).

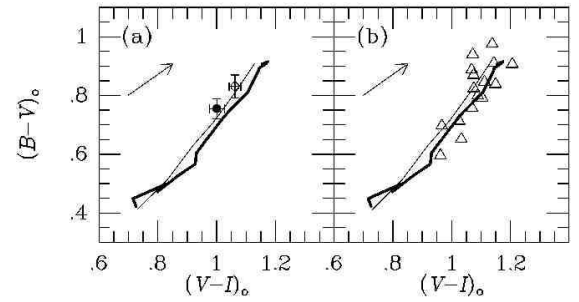
| Name       | $(B-V)_o$<br>gap | $(V-I)_o$<br>gap | $(B-V)_o$<br>bar axis | $(V-I)_o$<br>bar axis | $A$<br>(arcsec) |
|------------|------------------|------------------|-----------------------|-----------------------|-----------------|
| 1          | 2                | 3                | 4                     | 5                     | 6               |
| ESO 325-28 | 0.76±0.07        | 1.01±0.05        | 0.60±0.03             | 0.88±0.02             | 4.10            |
| ESO 365-35 | 1.00±0.15        | 1.09±0.03        | 0.98±0.03             | 1.04±0.03             | 4.10            |
| ESO 426-2  | 0.95±0.05        | 1.13±0.04        | 0.81±0.03             | 1.07±0.07             | 4.10            |
| ESO 437-33 | 0.70±0.02        | 0.96±0.05        | 0.69±0.03             | 0.95±0.04             | 4.10            |
| ESO 437-67 | 0.55±0.23        | 1.00±0.21        | 0.65±0.05             | 0.95±0.03             | 10.94           |
| ESO 566-24 | 0.66±0.02        | 1.03±0.07        | 0.59±0.01             | 0.92±0.02             | 4.10            |
| ESO 575-47 | 0.79±0.10        | 1.16±0.24        | 0.65±0.04             | 0.89±0.05             | 5.47            |
| IC 1438    | 0.84±0.04        | 1.15±0.06        | 0.76±0.04             | 1.06±0.06             | 8.70            |
| IC 4214    | 0.79±0.04        | 1.02±0.02        | 0.74±0.03             | 1.02±0.02             | 8.21            |
| NGC 1079   | 0.92±0.12        | 1.03±0.04        | 0.87±0.03             | 1.02±0.03             | 17.40           |
| NGC 1291   | 0.81±0.02        | 1.01±0.04        | 0.83±0.02             | 1.02±0.05             | 30.00           |
| NGC 1326   | 0.84±0.01        | 1.11±0.01        | 0.86±0.01             | 1.10±0.04             | 10.94           |
| NGC 1398   | 0.93±0.02        | 1.20±0.02        | 0.89±0.02             | 1.18±0.02             | 8.70            |
| NGC 2665   | 0.68±0.05        | 1.05±0.19        | 0.47±0.07             | 0.81±0.09             | 5.47            |
| NGC 6782   | 0.86±0.05        | 1.14±0.06        | 0.87±0.04             | 1.12±0.06             | 8.70            |
| NGC 7098   | 1.20±0.07        | 0.91±0.06        | 0.85±0.02             | 0.97±0.05             | 10.87           |

**Table 14.** Mean gap and bar axis colours. Eight of the GZ2 sample galaxies did not have a measureable  $u$ -band total magnitude.

| Points<br>1                      | $\langle (u-g)_o \rangle$<br>2 | $\langle (g-i)_o \rangle$<br>3 | $\langle (g-r)_o \rangle$<br>4 | $\langle (r-i)_o \rangle$<br>5 | $\langle (B-V)_o \rangle$<br>6 | $\langle (V-I)_o \rangle$<br>7 |
|----------------------------------|--------------------------------|--------------------------------|--------------------------------|--------------------------------|--------------------------------|--------------------------------|
| gap                              | 1.56                           | 1.15                           | 0.72                           | 0.43                           | 0.83                           | 1.06                           |
| mean error                       | 0.06                           | 0.02                           | 0.02                           | 0.01                           | 0.04                           | 0.02                           |
| $\sigma_1$                       | 0.29                           | 0.12                           | 0.10                           | 0.08                           | 0.15                           | 0.08                           |
| bar axis                         | 1.43                           | 0.97                           | 0.64                           | 0.35                           | 0.75                           | 1.00                           |
| mean error                       | 0.06                           | 0.03                           | 0.02                           | 0.01                           | 0.03                           | 0.02                           |
| $\sigma_1$                       | 0.28                           | 0.13                           | 0.10                           | 0.05                           | 0.14                           | 0.10                           |
| $\langle \text{gap-bar} \rangle$ | 0.13                           | 0.17                           | 0.09                           | 0.08                           | 0.08                           | 0.06                           |
| mean error                       | 0.07                           | 0.03                           | 0.02                           | 0.01                           | 0.03                           | 0.02                           |
| $\sigma_1$                       | 0.37                           | 0.13                           | 0.10                           | 0.07                           | 0.11                           | 0.09                           |
| $N$                              | 25                             | 25                             | 33                             | 33                             | 16                             | 16                             |

**Figure 15.** (a) and (c) show the colour-colour plots for the average colours of the gap (open circles) and bar axis points (filled circles) from Table 14, while (b) and (d) show the same plots for the total colours of the galaxies (open triangles) from Table 3. The solid curves are mean colour-colour relations for normal galaxies of different types in the SDSS filter system from Shimasaku et al. (2001). All colours are corrected for galactic extinction values from NED. The arrows indicate the reddening vectors.

strongly resemble the manifold morphology  $rR_1$ , described in detail by Romero-Gómez et al. (2006). To this category we could also add NGC 1326 and PGC 1857116. A possible point of disagreement is that the  $rR_1$  models place the cusps of the manifold inner ring as coincident with the dimples of the manifold  $R_1$  outer ring. This is not necessarily seen in all of these examples. In NGC 6782, for example, there is considerable distance between the strong inner ring cusps and the  $R_1$  dimples. Such a separation would be expected if the  $R_1$  outer ring begins outside  $r_{CR}$  and the inner ring ends

**Figure 16.** (a) Colour-colour plot for the gap (open circle) and the bar axis points (filled circle) in the non-GZ2 subsample. For comparison, the thin curve shows model galactic colours for a Salpeter initial mass function from Kennicutt et al. (1994), while the thick solid curve shows the colour-colour correlations for bright RC3 galaxies from Buta et al. (1994) and Buta & Williams (1995). (b) Same as (a) for the total colours of the non-GZ2 galaxies (open triangles). The arrows in both graphs indicate the reddening vectors.

near  $r_{I4R}$ , as is suggested by the resonance idea. Athanassoula et al. (2010) argue that if the cusps of the inner ring do not overlap the dimples of the  $R_1$  outer ring, then this just means that the  $L_1$  and  $L_2$  points lie between the cusps and dimples. Examination of the schematics in Figure 13 shows that the gap method in general places  $R_1$ -component dimples either close to or just outside  $r_{CR}$ .

Romero-Gómez et al. (2006) also make the interesting note that the  $R_1$  ring in the manifold  $rR_1$  morphology is not necessarily associated with the OLR, but instead the outer branches of the manifolds extend to  $0.86r_{OLR}$ . This actually agrees with our estimate of  $\langle a/r_{OLR} \rangle = 0.85$  for 36 galaxies with  $R_1$  components in Table 8, i.e., that  $R_1$  rings lie well inside  $r_{OLR}$ . Another issue is that inner rings like those seen in NGC 1433 and NGC 7098 have a tightly-wrapped spiral structure that suggests a link to the I4R. This is implied, for example, by the test-particle model illustrated by Simkin et al. (1980), which shows the development of a strong, cuspy



inner ring made of at least two and possibly four separate sections of spiral arms, developing in a relatively weak bar model.

Manifolds can also well explain the  $R_1R'_2$  as well as  $R_1R_2$  closed double outer ring morphologies. Athanassoula et al. (2009a) show that a different type of manifold orbit can account for these types: the heteroclinic type where particles emanate from  $L_1$  or  $L_2$  and return to the same point. Such manifolds do resemble objects like NGC 1079, 2766, 3081, and UGC 10168 in the present sample. Pure  $R'_2$  rings are interpreted differently. In the manifold theory, these are instead associated with “escaping” manifold orbits, where particles emanating from  $L_1$  or  $L_2$  do not go to either the same or the opposite Lagrangian point, but spiral outward. It is possible for these escaping manifolds to intersect on opposite sides of a galaxy roughly after winding about  $270^\circ$ . This would then form an  $R'_2$  outer pseudoring. In the present sample, the purest  $R'_2$  rings are found in CGCG 13-75, ESO 325-28, NGC 4935, NGC 5211, UGC 4771, and UGC 10712.

The case of ESO 566-24 and its strong four-armed spiral pattern is interesting from the manifold point of view. As shown in Figure 13, the gap method places the pattern largely between  $r_{I4R}$  and  $r_{O4R}$ , consistent with the numerical study of Rautiainen et al. (2004). Athanassoula et al. (2009b) state that the manifold theory most easily explains two-armed barred spirals, but to get a regular  $m=4$  manifold pattern in a barred galaxy would require more than two saddle points and a potential which is bar-like inside  $r_{CR}$  and spiral-like outside  $r_{CR}$ .

## 10.2 Dark Spaces and Bar Evolution

The recent study by Kim et al. (2016) touches on issues of dark spaces in barred galaxies from a somewhat different point of view. In this paper, the authors quantify light deficits in barred galaxies by comparing surface brightness profiles along the deprojected bar axis with those along an axis perpendicular to the bar. They find that the maximum difference between the profiles,  $\text{Max}(\Delta\mu) = \text{Max}[\mu(\text{bar minor axis}) - \mu(\text{bar major axis})]$ , correlates with bar length and bar-to-total luminosity ratio. Using numerical simulations, they show that  $\text{Max}(\Delta\mu)$  should increase with time as a bar grows stronger and longer by capturing disk stars in the vicinity of the bar.

The profiles shown in Figures 5 and 10 are the same kinds as those used by Kim et al. (2016; see also Buta et al. 2006). These figures give  $\text{Max}(\Delta\mu)$  in  $i$ -band light as 1.32 mag for UGC 4596 and 2.47 mag for NGC 5335. The Kim et al. study does not distinguish (r) dark-spacers from (rR) dark-spacers but nevertheless their Figure 1 shows an example of both: NGC 1015 and IC 1438. NGC 1015 would be interpreted here as an (r) dark-spacer, while IC 1438 is an (rR) dark-spacer in common with the present study.

As discussed in section 8, if the gaps in surface brightness or residual intensity between inner and outer ring features in (rR) dark-spacers are linked to the  $L_4$  and  $L_5$  Lagrangian points in a bar field, then a very consistent picture of the structure of galaxies having  $R_1$ ,  $R'_1$ ,  $R'_2$ , and  $R_1R'_2$  outer rings/pseudoring in terms of basic galactic resonances emerges. The analysis has suggested that, in general, the bars in (rR) dark-spacers extend to  $r_{I4R}$ , not  $r_{CR}$ . The inner rings in such galaxies also have a wide range of shapes,

from nearly circular to intrinsic axis ratios of  $\approx 0.5$  (see also Figure 5 of Buta 2014).

A very different interpretation of (r) dark-spacers follows from the Lagrangian points assumption. The bars of such galaxies would extend beyond their implied CR radii as shown in Table 7. While this may only signify a failure of the assumption in these cases, (r) dark-spacers have additional differences compared to (rR) dark-spacers that may have dynamical significance. First, Table 15 shows that the four examples of (r) dark-spacers in the GZ2 subsample have inner rings whose deprojected axis ratio averages much rounder than those in (rR) dark-spacer galaxies:  $\langle q_0 \rangle = 0.92 \pm 0.02$  versus  $0.72 \pm 0.02$ . This difference would be unchanged if NGC 1015 from Kim et al. (2016) were added to the subset. While this could be a selection effect if (r) dark-spacers are easier to recognize when a ring is intrinsically circular, it is interesting that Kim et al. (2016) show a model of an evolved barred galaxy which strongly resembles an (r) dark-spacer with a nearly circular inner ring.

Another difference is highlighted in Table 16, which lists the average  $m = 2, 4$ , and 6 relative Fourier intensity amplitudes for (rR) dark-spacers as compared to (r) dark-spacers, using the information from Table 5. Although the two types have about the same  $\langle A_2 \rangle$ , (r) dark-spacers tend to have bars with larger  $\langle A_4 \rangle$  and  $\langle A_6 \rangle$  amplitudes. This reflects how many of the (rR) dark-spacers in our sample have massive ovals as their main perturbation rather than conventional bars. Ovals would tend to have weaker higher-order Fourier terms than would conventional bars. From Figure 1 of Kim et al. (2016), adding NGC 1015 to our sample would not change this result. Also, their model after 9Gyr clearly shows a bar with significant higher-order Fourier terms.

Kim et al. (2016) further examine correlations between  $\text{Max}(\Delta\mu)$  and parameters such as the bar radius relative to the isophotal radius of the galaxy, the bar-to-total luminosity ratio, the bar Sérsic index  $n_{bar}$ , and the bar ellipticity  $\epsilon_{bar}$ . These parameters are based partly on decompositions. Table 17 lists  $\text{Max}(\Delta\mu)$  values for all 54 of the galaxies in the present sample, as well as the radii in arcseconds where these maxima occur. The values for filters  $g$  and  $B$ ,  $r$  and  $V$ , and  $i$  and  $I$  are listed in each separate column. Figure 17 first shows that  $\text{Max}(\Delta\mu)$  for the GZ2/CSRG sample correlates very well with the near-infrared relative  $m = 2$  Fourier amplitude  $A_2(i, I)$  (Table 5). The lines in the graph are least squares fits that force the lines to pass through the origin. The relations after two cycles of  $2\sigma$  rejection are

$$\text{Max}[\Delta\mu(g, B)] = (2.618 \pm 0.029)A_2(i, I)$$

$$\text{Max}[\Delta\mu(r, V)] = (2.394 \pm 0.021)A_2(i, I)$$

$$\text{Max}[\Delta\mu(i, I)] = (2.337 \pm 0.020)A_2(i, I)$$

These relations and Table 17 in addition show that  $\Delta\mu$  can vary with wavelength, being somewhat larger in  $g$  and  $B$  compared to  $i$  and  $I$ , and that the radii,  $r[\text{Max}(\Delta\mu)]$ , where these maxima occur are not necessarily the same for each filter, although many are similar. Figure 18 shows that  $r[\text{Max}(\Delta\mu(i, I))]$  correlates well with the bar radii listed in Tables 6 and 7.

Figure 19, left, shows a graph similar to Figure 6 of Kim

**Table 15.** Inner rings in (r) dark-spacer galaxies. Col. 1: galaxy name; cl. 2: type of feature (r=inner ring, rs=inner pseudoring; cols. 3,4: deprojected major and minor axis ring dimensions, respectively, in arcseconds; cols. 5-6: ratios of ring dimensions to the inner 4:1 resonance radius; col. 7: feature minor-to-major axis ratio; col. 8: relative deprojected angle between the bar major axis and the deprojected major axis position angle of the feature.

| Name       | Feature | $a$  | $b$  | $a/r_{I4R}$ | $b/r_{I4R}$ | $q_0$ | $ \theta_{Bf} $ |
|------------|---------|------|------|-------------|-------------|-------|-----------------|
| 1          | 2       | 3    | 4    | 5           | 6           | 7     | 8               |
| NGC4608    | r       | 51.0 | 49.3 | 2.14        | 2.07        | 0.97  | 17.1            |
| NGC5335    | rs      | 27.2 | 24.3 | 2.46        | 2.20        | 0.89  | 81.7            |
| NGC5686    | r       | 6.4  | 5.7  | 2.09        | 1.88        | 0.90  | 85.9            |
| UGC05380   | r       | 15.3 | 14.4 | 2.79        | 2.62        | 0.94  | 39.2            |
| means      |         | .... | .... | 2.37        | 2.19        | 0.92  | 56.0            |
| mean error |         | .... | .... | 0.16        | 0.16        | 0.02  | 16.7            |
| $\sigma_1$ |         | .... | .... | 0.32        | 0.31        | 0.04  | 33.4            |
| $N$        |         | .... | .... | 4           | 4           | 4     | 4               |

**Table 16.** Mean relative Fourier intensity amplitudes for (rR) dark-spacers as compared with (r) dark-spacers, from data in Table 5. Col. 1: Type of dark-spacer; cols. 2-4: mean  $m = 2, 4$ , and 6 amplitudes (with mean error followed by standard deviation in parentheses); col. 5: number of galaxies in averages.

| Morphology | $\langle A_2 \rangle$ | $\langle A_4 \rangle$ | $\langle A_6 \rangle$ | $N$ |
|------------|-----------------------|-----------------------|-----------------------|-----|
| 1          | 2                     | 3                     | 4                     | 5   |
| (rR)       | 0.69±0.04 (0.25)      | 0.29±0.02 (0.17)      | 0.15±0.02 (0.16)      | 50  |
|            |                       | 0.39±0.08 (0.16)      | 0.24±0.05 (0.10)      | 4   |

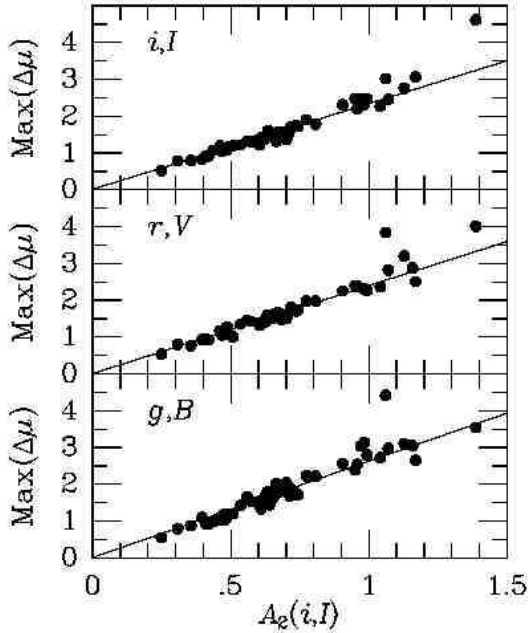


**Figure 17.** Graphs showing how well the parameter  $\text{Max}(\Delta\mu)$  ( $\text{mag arcsec}^{-2}$ ) correlates with the maximum relative  $m=2$  Fourier intensity amplitude  $A_2$  which is based only on the infrared band images. The lines are least squares fits that have been forced to pass through the origin. These lines are after two cycles of 2 $\sigma$  rejection.

et al. (2016), except that here the bar radius is normalized to the effective (half-power) radius  $a_e(i, I)$  in the infrared bands, rather than an isophotal radius. These radii were derived from the integrated luminosity distributions and the

total magnitudes and colours listed in Tables 3 and 4. The values of  $a_e(i, I)$  as well as  $a_e(g, B)$  and  $a_e(r, V)$  in arcseconds are listed in Table 18. The points for (rR) dark-spacers in Figure 19 are indicated by filled circles while those for the four (r) dark-spacers are indicated by open circles. In this graph, a clear correlation is seen, although it is not as strong as that found by Kim et al. The Spearman rank correlation coefficient is  $\rho = 0.41$  with a statistical significance of 0.001. In this graph, the (r) dark-spacers blend with the (rR) dark-spacers and do not stand out. In Figure 19, right, however, which plots  $\text{Max}[\Delta\mu(i, I)]$  versus the mean gap radius  $r_{gp}$  (listed as  $r_{CR}$  in Table 6) normalized to  $a_e(i, I)$  shows a poorer correlation and that the (r) dark-spacers stand out relative to the (rR) dark-spacers.

In the context of ring shapes, both manifold theory (Athanasoulas et al. 2009b) and resonance theory (Schwarz 1984b; Salo et al. 1999) predict that the intrinsic axis ratios of inner rings and outer  $R_1$ ,  $R'_1$  rings in barred and oval galaxies should depend significantly on bar strength. Figure 20 shows graphs of the deprojected axis ratios  $q_0$  versus  $\text{Max}(\Delta\mu)$  for these ring types in the GZ2/CSRG sample. In the inner ring graphs, (r) dark-spacers are distinguished from (rR) dark-spacers using open circles. If  $\text{Max}(\Delta\mu)$  is taken as an indicator of bar strength, then inner ring shapes show a significant correlation with bar strength (see also Grouchy et al. 2010). The Spearman rank correlation coefficients are  $\rho(g, B) = -0.646$  ( $P < 10^{-6}$ ),  $\rho(r, V) = -0.588$  ( $P = 3 \times 10^{-6}$ ),  $\rho(i, I) = -0.588$  ( $P = 2.5 \times 10^{-6}$ ), for  $N = 53, 51$ , and 52 inner rings, respectively, from Tables 10 and 15.

In contrast, the present sample shows little dependence of  $R_1$ ,  $R'_1$  intrinsic ring shapes on  $\text{Max}(\Delta\mu)$ . Restricting to the best-defined cases as depicted in Figure 13, the Spearman rank correlation coefficients are  $\rho(g, B) = -0.166$  ( $P = 0.225$ ),  $\rho(r, V) = -0.220$  ( $P = 0.170$ ), and  $\rho(i, I) = -0.139$

**Table 17.** Maximum values of  $\Delta\mu = \mu(\text{bar minor axis}) - \mu(\text{bar major axis})$  for full sample. (a)  $\text{Max}(\Delta\mu)$  values in  $\text{mag arcsec}^{-2}$ ; (b):  $r[\text{Max}(\Delta\mu)]$  in arcseconds. Col. 1: galaxy name; col. 2: values in  $g$ -band (GZ2) or  $B$ -band (non-GZ2); col. 3: values in  $r$ -band (GZ2) or  $V$ -band (non-GZ2); col. 4: values in  $i$ -band (GZ2) or  $I$ -band (non-GZ2)

| Galaxy                         | $g,B$ | $r,V$ | $i,I$ | Galaxy      | $g,B$ | $r,V$ | $i,I$ | Galaxy      | $g,B$ | $r,V$ | $i,I$ |
|--------------------------------|-------|-------|-------|-------------|-------|-------|-------|-------------|-------|-------|-------|
| 1                              | 2     | 3     | 4     | 1           | 2     | 3     | 4     | 1           | 2     | 3     | 4     |
| (a) $\text{Max}(\Delta\mu)$    |       |       |       |             |       |       |       |             |       |       |       |
| CGCG 8-10                      | 2.04  | 1.50  | 1.37  | IC 4214     | 1.74  | 1.53  | 1.45  | NGC 5211    | 0.94  | 0.95  | 0.91  |
| CGCG 13-75                     | 1.43  | 1.35  | 1.22  | MCG 6-32-24 | 1.54  | 1.32  | 1.22  | NGC 5335    | 2.39  | 2.38  | 2.46  |
| CGCG 65-2                      | 1.67  | 1.40  | 1.39  | MCG 7-18-40 | 1.17  | 1.09  | 1.09  | NGC 5370    | 1.44  | 1.51  | 1.45  |
| CGCG 67-4                      | 3.14  | 2.30  | 2.33  | NGC 210     | 1.18  | ....  | ....  | NGC 5686    | 0.79  | 0.81  | 0.79  |
| CGCG 73-53                     | 0.92  | 0.92  | 0.92  | NGC 1079    | 1.62  | 1.52  | 1.52  | NGC 5701    | 1.21  | 1.23  | 1.16  |
| CGCG 185-14                    | 0.56  | 0.54  | 0.53  | NGC 1291    | 1.05  | 1.12  | 1.10  | NGC 6782    | 1.80  | 1.61  | 1.60  |
| CGCG 263-22                    | 1.67  | 1.47  | 1.33  | NGC 1326    | 1.47  | 1.44  | 1.42  | NGC 7098    | 1.91  | 1.48  | 1.57  |
| ESO 325-28                     | 2.23  | 1.98  | 1.90  | NGC 1398    | 1.09  | 1.17  | 1.19  | PGC 54897   | 2.54  | 2.38  | 2.19  |
| ESO 365-35                     | 1.20  | 1.01  | 1.19  | NGC 1433    | 3.04  | ....  | 2.48  | PGC 1857116 | 2.79  | 2.26  | 2.46  |
| ESO 426-2                      | 1.75  | 1.71  | 1.76  | NGC 2665    | 4.42  | 3.84  | 3.02  | PGC 2570478 | 1.02  | 1.05  | 1.05  |
| ESO 437-33                     | 1.52  | 1.39  | 1.35  | NGC 2766    | 1.10  | 0.93  | 0.82  | UGC 4596    | 2.03  | 1.65  | 1.32  |
| ESO 437-67                     | 2.66  | 2.51  | 3.07  | NGC 3081    | 1.91  | ....  | 1.57  | UGC 4771    | 1.79  | 1.66  | 1.53  |
| ESO 566-24                     | 1.33  | 1.34  | 1.42  | NGC 3380    | 2.22  | 1.98  | 1.79  | UGC 5380    | 1.72  | 1.75  | 1.72  |
| ESO 575-47                     | 2.56  | 2.25  | 2.31  | NGC 4113    | 3.54  | 4.01  | 4.61  | UGC 5885    | 3.10  | 3.21  | 2.75  |
| IC 1223                        | 1.19  | 1.07  | 1.08  | NGC 4608    | 1.69  | 1.70  | 1.70  | UGC 9418    | 1.89  | 1.81  | 1.65  |
| IC 1438                        | 1.93  | 1.64  | 1.55  | NGC 4736    | 0.98  | 1.07  | 0.00  | UGC 10168   | 1.08  | 1.27  | 1.09  |
| IC 2473                        | 2.72  | 2.36  | 2.28  | NGC 4935    | 1.53  | 1.43  | 1.30  | UGC 10712   | 1.85  | 1.63  | 1.51  |
| IC 2628                        | 0.88  | 0.76  | 0.80  | NGC 5132    | 2.98  | 2.81  | 2.45  | UGC 12646   | 3.05  | 2.88  | ....  |
| (b) $r[\text{Max}(\Delta\mu)]$ |       |       |       |             |       |       |       |             |       |       |       |
| CGCG 8-10                      | 21.2  | 12.8  | 12.8  | IC 4214     | 29.1  | 29.7  | 29.7  | NGC 5211    | 17.2  | 18.0  | 18.4  |
| CGCG 13-75                     | 8.4   | 8.4   | 9.2   | MCG 6-32-24 | 8.8   | 8.4   | 8.4   | NGC 5335    | 16.0  | 15.2  | 15.2  |
| CGCG 65-2                      | 10.8  | 10.0  | 5.2   | MCG 7-18-40 | 6.4   | 5.2   | 4.8   | NGC 5370    | 11.6  | 11.2  | 12.0  |
| CGCG 67-4                      | 8.8   | 9.2   | 10.0  | NGC 210     | 40.9  | 17.0  | 17.0  | NGC 5686    | 4.4   | 4.8   | 4.4   |
| CGCG 73-53                     | 6.8   | 7.2   | 6.8   | NGC 1079    | 42.7  | 42.2  | 40.0  | NGC 5701    | 33.2  | 33.2  | 32.8  |
| CGCG 185-14                    | 7.6   | 7.2   | 7.6   | NGC 1291    | 88.9  | 95.6  | 87.4  | NGC 6782    | 26.5  | 27.2  | 29.1  |
| CGCG 263-22                    | 21.2  | 22.4  | 21.0  | NGC 1326    | 38.0  | 38.2  | 39.0  | NGC 7098    | 86.8  | 87.6  | 85.6  |
| ESO 325-28                     | 13.2  | 12.7  | 12.7  | NGC 1398    | 45.7  | 45.5  | 43.9  | PGC 54897   | 10.0  | 9.6   | 9.2   |
| ESO 365-35                     | 15.9  | 14.3  | 13.8  | NGC 1433    | 110.5 | ....  | 111.8 | PGC 1857116 | 12.6  | 11.4  | 11.8  |
| ESO 426-2                      | 18.7  | 15.9  | 15.9  | NGC 2665    | 33.4  | 33.9  | 33.9  | PGC 2570478 | 7.6   | 6.8   | 6.8   |
| ESO 437-33                     | 15.4  | 14.8  | 23.6  | NGC 2766    | 16.0  | 15.4  | 15.4  | UGC 4596    | 15.6  | 16.0  | 14.8  |
| ESO 437-67                     | 39.0  | 39.6  | 44.0  | NGC 3081    | 36.4  | ....  | 36.4  | UGC 4771    | 11.6  | 11.2  | 10.8  |
| ESO 566-24                     | 22.0  | 9.9   | 10.4  | NGC 3380    | 20.0  | 19.6  | 21.6  | UGC 5380    | 7.6   | 7.6   | 8.0   |
| ESO 575-47                     | 31.4  | 29.7  | 25.9  | NGC 4113    | 19.2  | 20.0  | 20.8  | UGC 5885    | 21.2  | 21.6  | 21.2  |
| IC 1223                        | 20.4  | 9.0   | 9.2   | NGC 4608    | 34.0  | 30.4  | 31.6  | UGC 9418    | 10.4  | 9.6   | 9.6   |
| IC 1438                        | 22.6  | 21.8  | 21.0  | NGC 4736    | 216.8 | 234.0 | 71.2  | UGC 10168   | 16.8  | 23.2  | 16.4  |
| IC 2473                        | 29.2  | 29.2  | 33.2  | NGC 4935    | 10.4  | 10.0  | 10.0  | UGC 10712   | 8.0   | 7.6   | 7.6   |
| IC 2628                        | 8.0   | 5.2   | 5.2   | NGC 5132    | 35.2  | 36.4  | 33.2  | UGC 12646   | 23.2  | 22.5  | ....  |

( $P=0.268$ ), for  $N=23$ , 21, and 22 rings, respectively, from Table 8.

## 11 SUMMARY

This paper has developed the “gap method” of locating the radius of the corotation resonance in mainly early-to-intermediate type barred and oval disk galaxies. The study was motivated by the extreme dark spaces noticed in some galaxies in the GZ2 ring sample (paper I), specifically UGC 4596 and NGC 5335. These represent two types of “dark-spacer” morphologies:

- (rR) dark-spacers, where gaps of low surface brightness are found between inner and outer ring features, the latter

often including features classified as  $R_1$ ,  $R'_1$ ,  $R'_2$ , and  $R_1R'_2$ , outer rings and pseudorings; and

- (r) dark-spacers, where dark zones lie inside an inner ring crossed by a conspicuous bar.

The paper makes the assumption that the gaps in these galaxies are linked to the  $L_4$  and  $L_5$  Lagrangian points that would exist in a bar field. Two approaches have been used to derive the gap radius  $r_{gp}$ : direct parabolic fits to the gap surface brightnesses (when these are deep) and parabolic fits to residual intensities after subtraction of a heavily median-smoothed background (when the gap surface brightnesses are shallow). Taking the corotation radius  $r_{CR} = r_{gp}$ , usually based on an average of three filters, this paper has shown that



**Table 18.** Effective radii for full sample. Col. 1: galaxy name; col. 2: effective radii in  $g$ -band (GZ2) or  $B$ -band (non-GZ2); col. 3: effective radii in  $r$ -band (GZ2) or  $V$ -band (non-GZ2); col. 4: effective radii in  $i$ -band (GZ2) or  $I$ -band (non-GZ2). All values in arcseconds.

| Galaxy<br>1 | $a_e(g,B)$<br>2 | $a_e(r,V)$<br>3 | $a_e(i,I)$<br>4 | Galaxy<br>1 | $a_e(g,B)$<br>2 | $a_e(r,V)$<br>3 | $a_e(i,I)$<br>4 | Galaxy<br>1 | $a_e(g,B)$<br>2 | $a_e(r,V)$<br>3 | $a_e(i,I)$<br>4 |
|-------------|-----------------|-----------------|-----------------|-------------|-----------------|-----------------|-----------------|-------------|-----------------|-----------------|-----------------|
| CGCG 8-10   | 8.5             | 7.2             | 7.4             | IC 4214     | 26.9            | 25.8            | 22.7            | NGC 5211    | 18.3            | 15.5            | 14.2            |
| CGCG 13-75  | 7.8             | 6.4             | 6.2             | MCG 6-32-24 | 6.6             | 6.4             | 6.5             | NGC 5335    | 30.5            | 26.6            | 24.9            |
| CGCG 65-2   | 6.9             | 6.2             | 6.0             | MCG 7-18-40 | 8.8             | 8.0             | 7.8             | NGC 5370    | 11.8            | 10.9            | 10.9            |
| CGCG 67-4   | 6.0             | 5.8             | 5.8             | NGC 210     | ....            | 37.1            | ....            | NGC 5686    | 6.1             | 6.0             | 6.2             |
| CGCG 73-53  | 5.2             | 4.8             | 5.0             | NGC 1079    | 34.8            | 33.6            | 31.1            | NGC 5701    | 39.3            | 33.6            | 32.9            |
| CGCG 185-14 | 8.9             | 7.8             | 7.6             | NGC 1291    | 89.0            | 78.8            | 71.2            | NGC 6782    | 19.7            | 19.3            | 18.2            |
| CGCG 263-22 | 11.4            | 10.7            | 10.6            | NGC 1326    | 30.8            | 30.2            | 29.2            | NGC 7098    | 49.1            | 45.4            | 38.2            |
| ESO 325-28  | 12.6            | 11.8            | 9.9             | NGC 1398    | 63.0            | 58.4            | 60.2            | PGC 54897   | 7.0             | 6.5             | 6.4             |
| ESO 365-35  | 10.4            | 9.5             | 8.2             | NGC 1433    | 82.1            | ....            | 71.1            | PGC 1857116 | 8.0             | 7.5             | 7.2             |
| ESO 426-2   | 14.3            | 12.1            | 10.8            | NGC 2665    | 22.6            | 21.0            | 19.7            | PGC 2570478 | 7.5             | 7.3             | 7.2             |
| ESO 437-33  | 10.1            | 9.3             | 7.7             | NGC 2766    | 13.9            | 12.7            | 12.4            | UGC 4596    | 12.1            | 10.3            | 9.8             |
| ESO 437-67  | 30.1            | 26.5            | 22.7            | NGC 3081    | 27.0            | ....            | 24.5            | UGC 4771    | 14.3            | 12.2            | 11.9            |
| ESO 566-24  | 19.6            | 17.6            | 16.4            | NGC 3380    | 15.0            | 14.8            | 15.2            | UGC 5380    | 13.2            | 12.1            | 11.9            |
| ESO 575-47  | 23.2            | 21.3            | 19.4            | NGC 4113    | 8.2             | 7.4             | 7.3             | UGC 5885    | 14.6            | 12.7            | 12.4            |
| IC 1223     | 9.1             | 8.8             | 8.9             | NGC 4608    | 33.8            | 31.9            | 30.4            | UGC 9418    | 10.8            | 8.8             | 8.4             |
| IC 1438     | 19.8            | 18.5            | 16.8            | NGC 4736    | 61.2            | ....            | 58.7            | UGC 10168   | 13.4            | 12.1            | 12.2            |
| IC 2473     | 17.9            | 16.2            | 15.6            | NGC 4935    | 12.7            | 10.7            | 10.3            | UGC 10712   | 10.9            | 7.8             | 7.6             |
| IC 2628     | 10.3            | 7.8             | 7.3             | NGC 5132    | 16.9            | 16.9            | 17.2            | UGC 12646   | 17.6            | 16.0            | ....            |

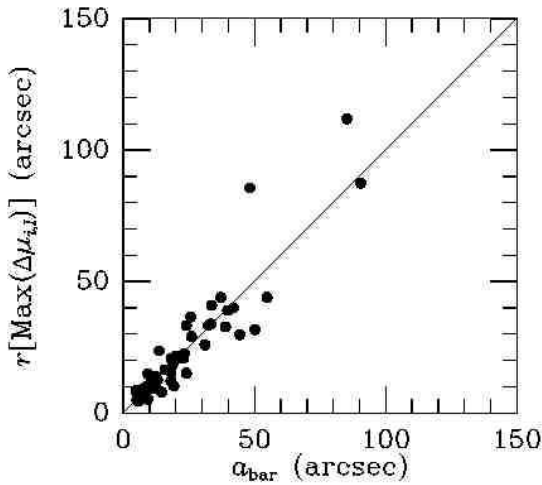


**Figure 18.** Graph showing that the radius of  $\text{Max}[\Delta\mu(i,I)]$  correlates well with the estimated bar radius from Tables 6 and 7. The line is not based on a least squares fit but is shown to guide the eye.

- Most  $R_1$  and  $R'_1$  outer rings and pseudorings are likely associated with the outer 4:1 resonance, not the OLR as was originally suggested by Schwarz (1981). Only 1 out of the 36 cases analyzed have  $a/r_{OLR} \approx 1$  as predicted by Schwarz (1981). Some support for an association with  $r_{O4R}$  in general comes from numerical simulation studies of NGC 1433 (Treuthardt et al. 2008), ESO 566–24 (Rautiainen et al. 2004) and NGC 6782 (Lin et al. 2008), where the best-fitting pattern speeds place an  $R'_1$  ring closer to  $r_{O4R}$  than to  $r_{OLR}$ .

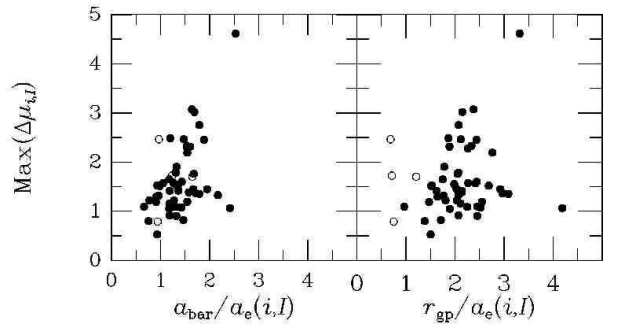


**Figure 19.** Graph showing  $\text{Max}[\Delta\mu(i,I)]$  ( $\text{mag arcsec}^{-2}$ ) versus (left) the bar radius and (right) the gap radius relative to the effective radius  $a_e$  in infrared light.

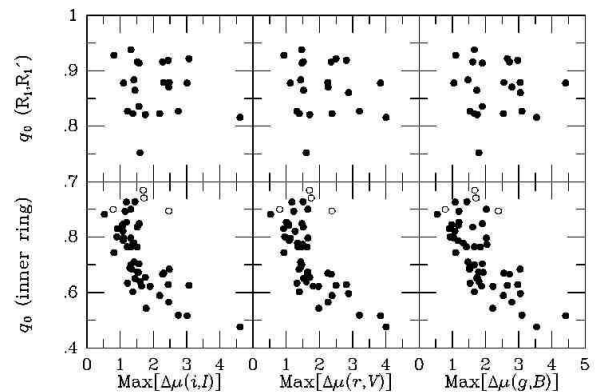


**Figure 20.** Graphs showing intrinsic axis ratios versus  $\text{Max}[\Delta\mu(i,I)]$  ( $\text{mag arcsec}^{-2}$ ) for inner rings and related features (lower frames) and outer  $R_1$  and  $R'_1$  outer rings (upper frames). Filled circles are for rings in (rR) dark-spacers, open circles are for rings in (r) dark-spacers.

$R_1$  and  $R'_1$  rings are approximately aligned perpendicular to the bar in our sample.

- The gap method links  $R'_2$  outer pseudorings to the OLR. The predictions from Schwarz (1981) are confirmed for these features.

The revised interpretation of  $R_1$  and  $R'_1$  rings means that the combined category,  $R_1R'_2$ , is actually a two-resonance ring morphology rather than both being associated with the OLR. Since all of these ring types are completely outside the CR radius (no visual mapping led to any of these features significantly crossing this radius), then a better way to describe them is as “outer resonant subclasses.”

- Virtually all of the inner features in the (rR) dark-spacer sample are placed very close to or straddling the inner 4:1 resonance. In no case does an inner feature significantly cross the CR radius. This association is consistent with Schwarz (1984a) and Simkin, Su, & Schwarz (1980).

- With few exceptions, the bars identified in the (rR) sample appear to extend to the I4R; some come close to  $r_{CR}$ . The average value  $\langle \mathcal{R} \rangle = 1.58 \pm 0.04$  (standard deviation 0.28) is large compared to previous studies, but cannot be dismissed completely because many of the bars in the sample of galaxies studied here lie inside an inner ring or related feature. If inner rings are linked to the inner 4:1 resonance as has been strongly suggested by the models of Schwarz (1984a) and Simkin, Su, & Schwarz (1980), then the bars within such rings cannot extend much beyond the I4R. Debbattista & Sellwood (2000) classified a bar as slow if  $\mathcal{R} > 1.4$  and “fast” if  $\mathcal{R} < 1.4$ . The analysis in this paper places these galaxies into the slow bar domain for the estimated bar radii.

The situation for (r) dark-spacers is less certain. If the dark regions in these galaxies also trace the  $L_4$  and  $L_5$  points, then the bars would exceed their corotation resonance radii, violating the Contopoulos (1980) rule. This paper has shown that (r) dark-spacers have rounder inner rings, stronger high-order relative Fourier intensity amplitudes, and lower values of  $r_{gp}$  relative to the near-infrared effective radii of the galaxies as compared to (rR) dark-spacers. Because the azimuthally-averaged colours are uniform across the bar-gap region in NGC 5335, it seems most likely that bar evolution is responsible for (r) dark-spacers in the sense that the bar depletes the old disk stars and grows stronger with time, probably by the mechanism highlighted by Kim et al. (2016). Indeed, on the basis of the uniform average colours across the gap, Buta (2014) had already noted: “Dust may not be an issue, because the spaces [in NGC 5335] are still dark even in the  $2.1\mu\text{m}$   $K_s$ -band (Buta et al. 2009). Could this imply that the bar in NGC 5335 has recently assembled itself from the old disk stellar population?”

- Analysis of (rR) gap colours and the colours of points along the bar axis at the same radius shows that dark gaps are redder than the bar axis points by  $\approx 0.1$  mag on average in all colours used. Although the trends are roughly parallel to the reddening lines in colour-colour diagrams, it is most likely that the colour differences are due to a stellar population difference, rather than higher internal extinction in the gaps. Gaps have average  $BVI$  and  $ugri$  colours comparable to the integrated colours of Sa galaxies, while the bar axis points have average colours similar to the integrated colours of Sb galaxies. Because (rR) dark-spacer gaps are not necessarily the same colour as the bar axis points, ow-

ing to the frequent presence of star-formation around the ends of the bars or ovals of these galaxies, it is likely that these gaps are not simply a question of evolutionary state of the bar and therefore just part of a continuum with (r) dark-spacers. Instead, the  $L_4$ ,  $L_5$  points and their stability provide the most reasonable interpretation of the dark gaps seen in (rR) dark-spacers.

Finally, several important issues remain:

(1) Although many galaxies in the GZ2/CSRG sample show the characteristic (rR) dark spaces, many, if not more, early-type disk galaxies do not show these features, even cases with an apparently strong bar. Do such cases imply that the  $L_4$ ,  $L_5$  Lagrangian points are stable, thus preventing the expected depletion of material around the points, or that these points are located so far out that the surface brightness is too low to see them? Why should these points be consequential in some barred and oval galaxies, and largely inconsequential in others?

(2) Even though a single pattern speed can account for much of the structure of galaxies showing  $R_1$ ,  $R'_1$ ,  $R'_2$ , and  $R_1R'_2$  outer rings and pseudorings, and that numerical simulation surveys (e.g., Rautiainen et al. 2008; Treuthardt et al. 2012) have shown that single pattern speed models can effectively reproduce structure even in galaxies without these features, other methods used to locate corotation resonances in galaxies have nevertheless strongly favoured the idea of multiple pattern speeds (e.g., Corsini et al. 2003; Buta & Zhang 2009; Font et al. 2011, 2014). This idea has also found some support from theory (e.g., Sellwood & Sparke 1988; Pfenniger & Norman 1990; Rautiainen & Salo 2000). These issues will be furthered examined in later papers in this series.

(3) Although flat rotation curves have been assumed for the analysis in this paper, the shape of the rotation curve could have a bearing on whether a galaxy might be seen to be an (rR) dark-spacer or an (r) dark-spacer. The referee has noted that some galaxies in the sample (e.g., NGC 1433 and NGC 3081) could be interpreted as having both types of dark spaces. The referee suggests that a slowly rising rotation curve might place the outer resonances so far out that only an inner ring would be seen. However, it is noteworthy that cases like NGC 1433 and NGC 3081 have extremely oval inner rings unlike the typical (r) dark-spacers highlighted in this paper.

I thank the anonymous referee for many helpful comments that substantially improved this paper. This work was supported in part by a grant from the Research Grants Committee, University of Alabama. The development of Galaxy Zoo was supported in part by the Alfred P. Sloan Foundation and by the Leverhulme Trust. I thank K. L. Masters and Arfon Smith for sending the links to the images of the sample of GZ2 ringed galaxies. This research has made use of the NASA/IPAC Extragalactic Database (NED) which is operated by the Jet Propulsion Laboratory, California Institute of Technology, under contract with the National Aeronautics and Space Administration. Funding for the creation and distribution of the SDSS Archive has been provided by the Alfred P. Sloan Foundation, the Participating Institutions, NASA, NSF, the U. S. Department of Energy, the Japanese Monbukagakusho, and the Max Planck Society. IRAF is written and supported by the National Optical Astronomy Observatories (NOAO) in Tucson, Arizona. NOAO is operated by the Association of Universities for Research

in Astronomy (AURA), Inc., under cooperative agreement with the National Science Foundation.

## 12 APPENDIX: AZIMUTHALLY-AVERAGED, RELATIVE FOURIER INTENSITY, AND BAR MINOR AXIS PROFILES OF 52 RINGED GALAXIES

The azimuthally-averaged profiles of the 31 GZ2 and 21 non-GZ2 ringed galaxies in the sample (excluding UGC 4596 and NGC 5335 which were described separately in section 5) are shown in Figure 21. These were obtained in each case by averaging the luminosity distribution over fixed ellipses having a shape and position angle equal to the disk axis ratio and major axis position angle listed in Table 2. These profiles were extrapolated to get total magnitudes and colours by fitting exponentials to the outer points. In most cases the slope was freely-fitted, but for the  $u$ -band it was generally necessary to force the slope to be the same as found for the  $g$ -band.

The relative Fourier intensity profiles for the same galaxies are shown in Figure 22. (The profiles for UGC 4596 and NGC 5335 are shown in Figures 6 and 11, respectively.) These are based only on the deprojected images in the  $i$ -band. Since no decompositions were performed, a few of the galaxies (e.g., NGC 2766 and CGCG 185-14) show inner amplitudes due to significant bulge deprojection stretch. The relative intensity profiles are shown only for the  $m = 2$ , 4, and 6 components, while the phase is shown only for the  $m = 2$  component in each case.

Figure 23 shows the bar minor profiles and how they were fitted to derive  $\langle r_{gp} \rangle$ . Those cases where the surface brightness profiles were fitted directly show only one panel analogous to Figures 7 and 12 for UGC 4596 and NGC 5335, respectively. These cases are indicated as “gri” or “BVI” in Table 2. For cases where residual intensities were fitted instead, the left panel shows three graphs of the residual intensity profiles and the parabolic fits used to get  $r_{gp}$  in each filter, while the right panel shows the minor axis bar profiles and the adopted value of  $\langle r_{gp} \rangle$  superposed as vertical lines. These cases are indicated as, for example, “intgri” or “intBVI” in Table 2 and are based on fits to images after subtraction of a heavily median-smoothed version of the same image. The smoothing box ranged from  $51 \times 51$  to  $161 \times 161$  pixels, depending roughly on the size of the galaxy.

## REFERENCES

- Abazajian K. N., et al., 2009, ApJS, 182, 543  
 Athanassoula E., 1992, MNRAS, 259, 328  
 Athanassoula E., Bosma A., Creze M., & Schwarz M. P., 1982, A&A, 107, 101  
 Athanassoula E., Romero-Gómez M., Masdemont J. J., 2009a, MNRAS, 394, 67  
 Athanassoula E., Romero-Gómez M., Bosma A., Masdemont J. J., 2009b, MNRAS, 400, 1706  
 Athanassoula E., Romero-Gómez M., Bosma A., Masdemont J. J., 2010, MNRAS, 407, 1433  
 Athanassoula E., Romero-Gómez M., Masdemont J. J., 2011, MSAIS, 18, 97  
 Baillard A. et al., 2011, A&A, 532, 74

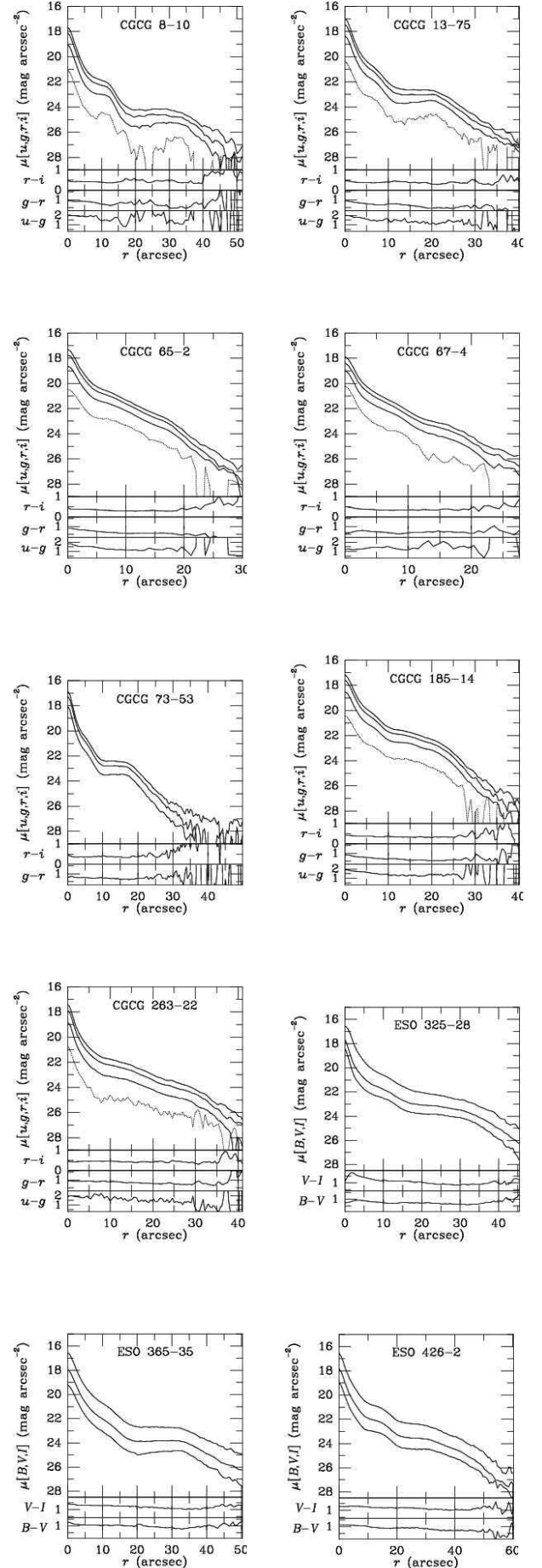


Figure 21.



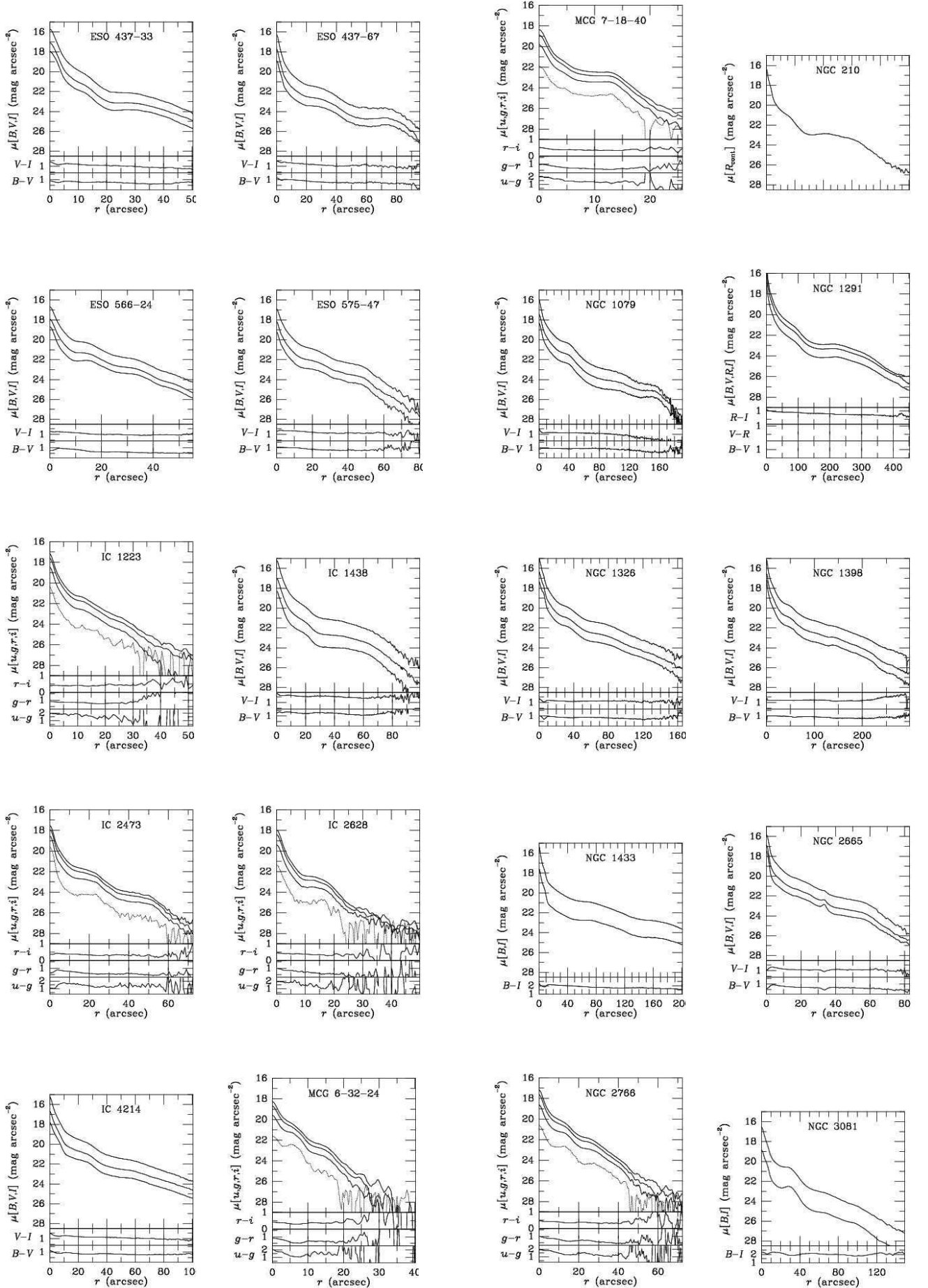


Figure 21. (cont.)

Figure 21. (cont.)

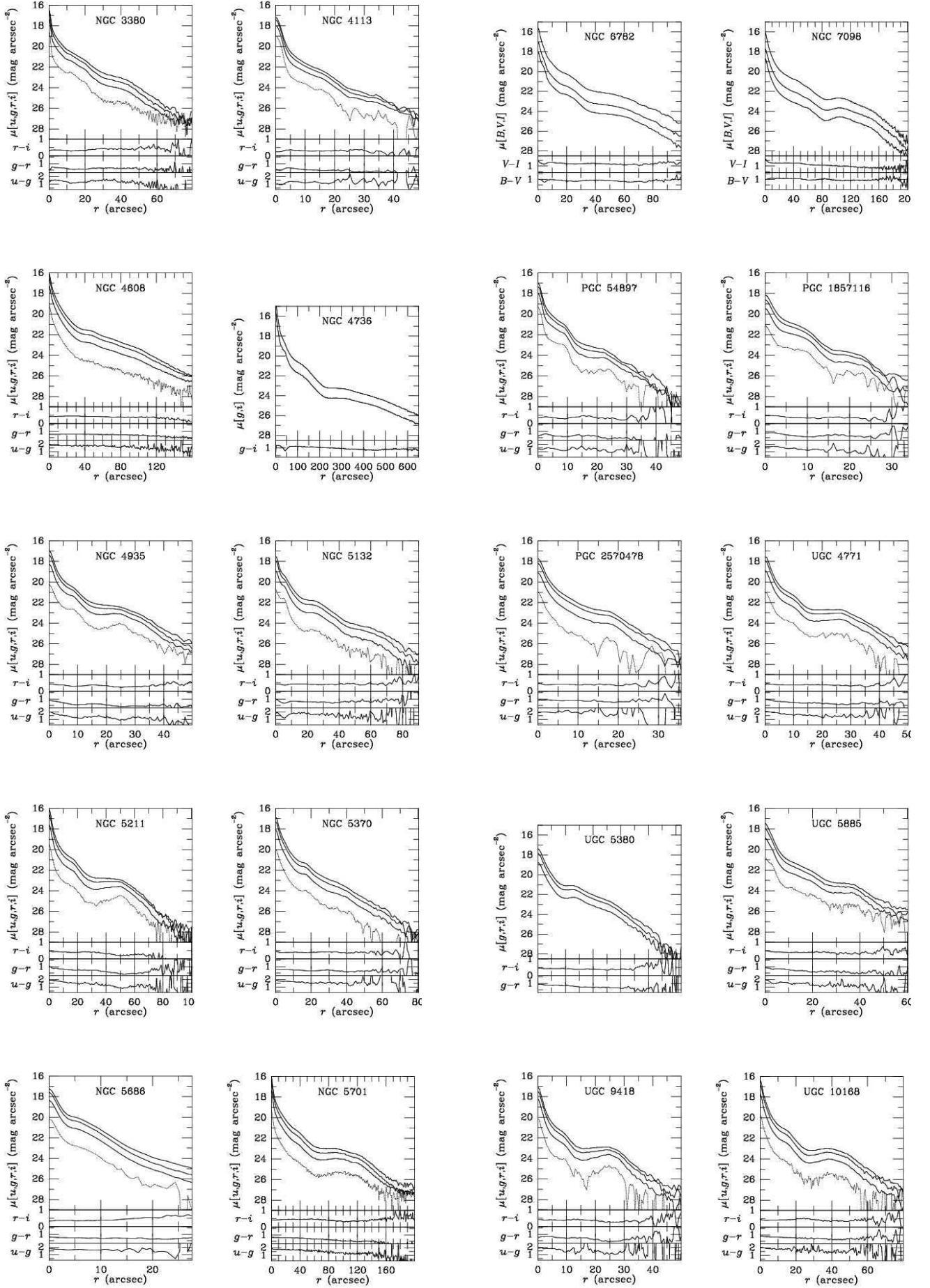
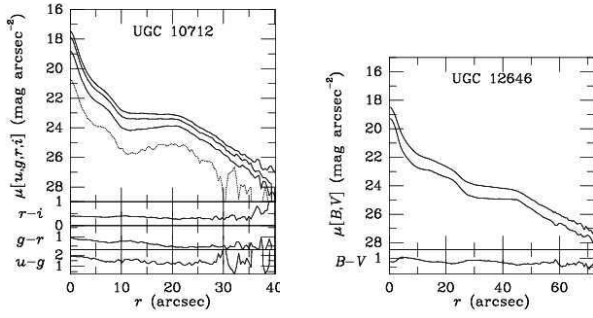


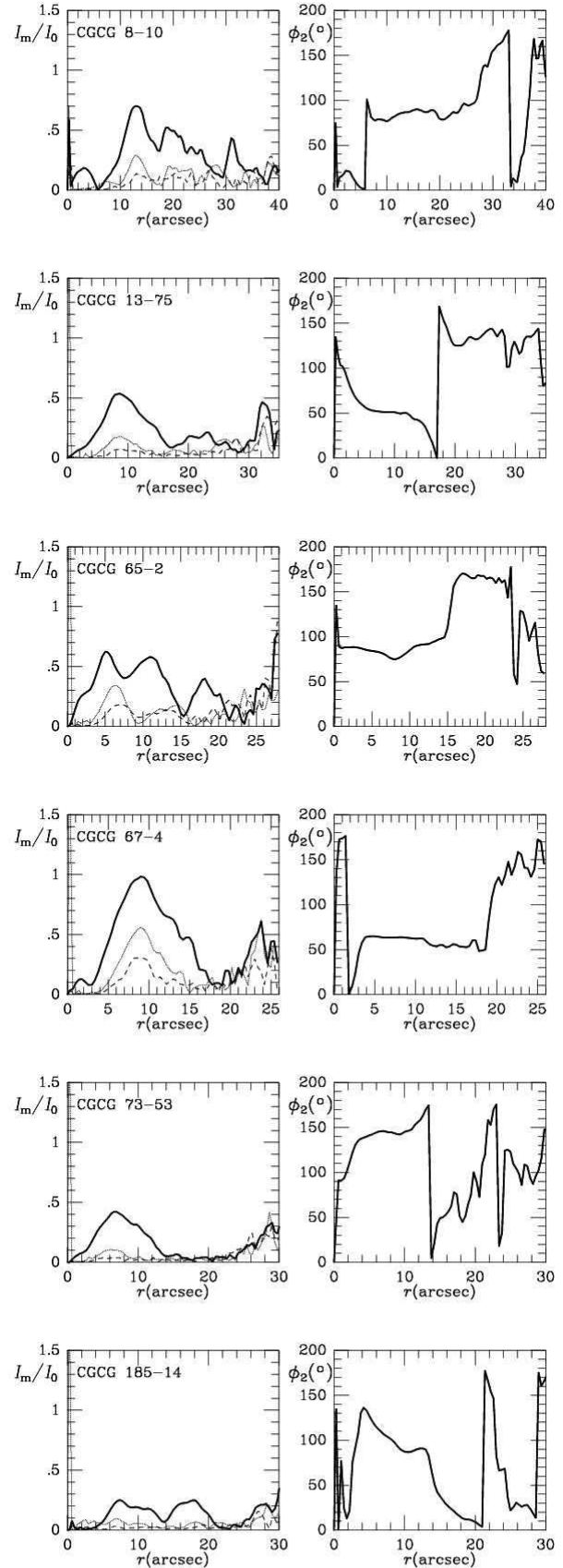
Figure 21. (cont.)

Figure 21. (cont.)



**Figure 21.** Azimuthally-averaged surface brightness profiles of 31 GZ2 and 21 non-GZ2 ringed galaxies. The profiles use the orientation parameters listed in Table 2. For GZ2 galaxies, the profiles from bottom to top are  $u$ ,  $g$ ,  $r$ , and  $i$ . For non-GZ2 galaxies, the profiles from bottom to top are  $B$ ,  $V$ , and  $I$ . A few non-GZ2 sample galaxies have only  $B$  and  $V$ ,  $B$  and  $I$ ,  $R$ , and (in one case)  $g$  and  $i$ .

Binney J., Tremaine S., 1987, *Galactic Dynamics*, Princeton University Press  
 Binney J., Tremaine S. 2008, *Galactic Dynamics*, Princeton University Press (2nd ed.)  
 Buta R., 1984, *Publ. Astr. Soc. Australia*, 5, 472  
 Buta R., 1995, *ApJS*, 96, 39  
 Buta R., 2012, in *Secular Evolution of Galaxies*, J. Falcón-Barroso & J. H. Knapen, eds., Cambridge, Cambridge University Press, p. 1  
 Buta R., 2013, in *Planets, Stars, and Stellar Systems*, Vol. 6: Extragalactic Astronomy and Cosmology, T. D. Oswalt & W. C. Keel, eds., New York, Springer, p. 1  
 Buta R., 2014, in *Structure and Dynamics of Disk Galaxies*, M. S. Seigar & P. Treuthardt, eds., ASP Conference Series, 480, 53  
 Buta R., 2017, submitted to *MNRAS* (paper I)  
 Buta R., Byrd G., Freeman T., 2004, *AJ*, 127, 1982  
 Buta R., Combes F., 1996, *Galactic Rings*, *Fund. of Cosmic Physics*, 17, 95 (BC96)  
 Buta R., Crocker D. A., 1991, *AJ*, 102, 1715 (BC91)  
 Buta R., Crocker D. A., 1992, *AJ*, 103, 1804  
 Buta R., Purcell G. B., 1998, *AJ*, 115, 484  
 Buta R., Williams K. L., 1995, *AJ*, 109, 543  
 Buta R., Zhang X., 2009, *ApJS*, 182, 559  
 Buta R., Corwin H., Odewahn S., 2007, *The de Vaucouleurs Atlas of Galaxies*, Cambridge, Cambridge University Press (deVA)  
 Buta R., Corwin H., de Vaucouleurs G., de Vaucouleurs A., Longo G., 1995, *AJ*, 109, 517  
 Buta R., Knapen J. H., Elmegreen B. G., Salo H., Laurikainen E., Elmegreen D. M., Puerari I., Block D. L., 2009, *AJ*, 137, 4487  
 Buta R., Laurikainen E., Salo H., Block D. L., Knapen J. H., 2006, *AJ*, 132, 1859  
 Buta R., Mitra S., de Vaucouleurs G., Corwin H. G., 1994, *AJ*, 107, 118  
 Buta R., Purcell G. B., Cobb M. L., Crocker D. A., Rautiainen P., Salo H. 1999, *AJ*, 117, 778  
 Buta R., Ryder S. D., Madsen G. J., Wesson K., Crocker D. A., Combes F. 2001, *AJ*, 121, 225  
 Buta R. et al., 2015, *ApJS*, 217, 32  
 Byrd G. G., Rautiainen P., Salo H., Buta R., Crocker D. A., 1994, *AJ*, 108, 476  
 Canzian B., 1993, *ApJ*, 414, 487  
 Comerón S. et al., 2014, *A & A*, 562, 121  
 Contopoulos G., 1980, *A&A*, 81, 198



**Figure 22.**



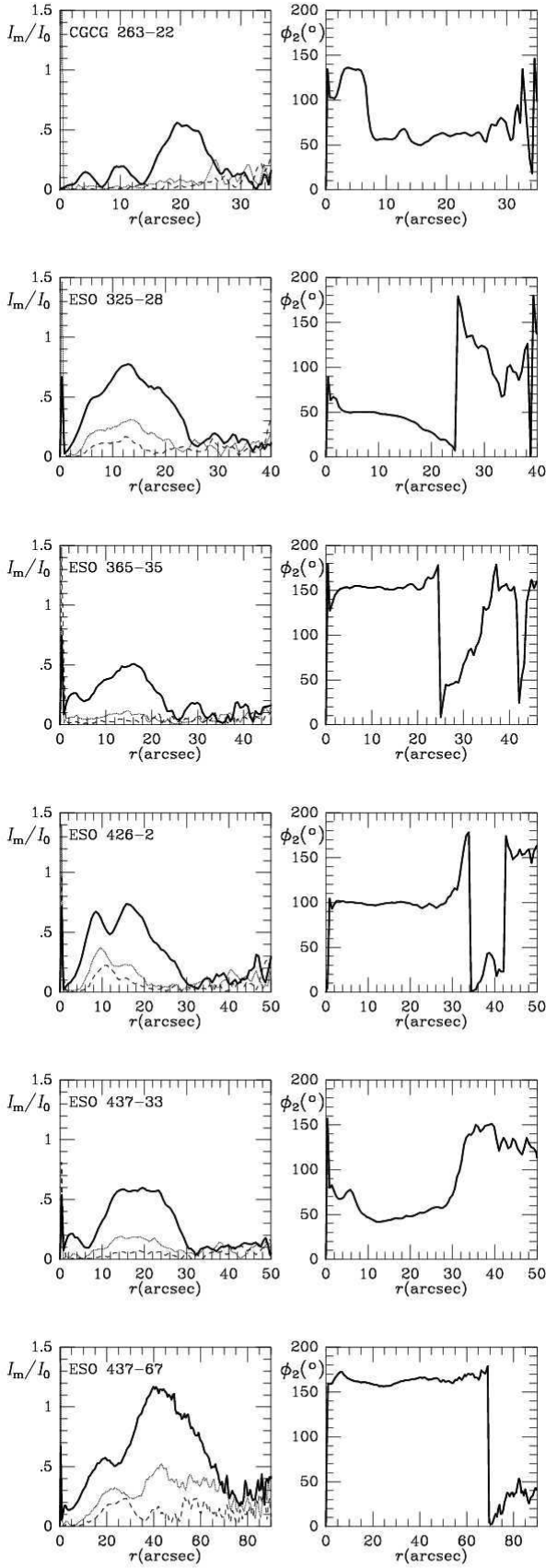


Figure 22. (cont.)

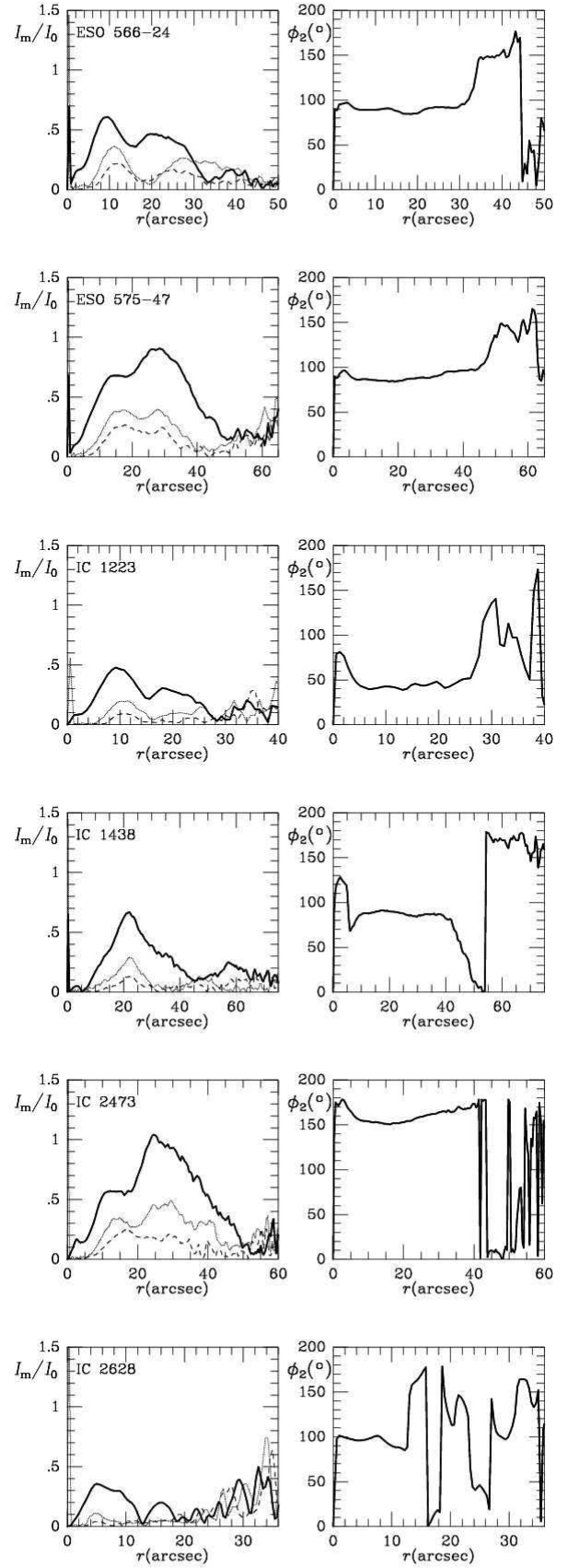


Figure 22. (cont.)



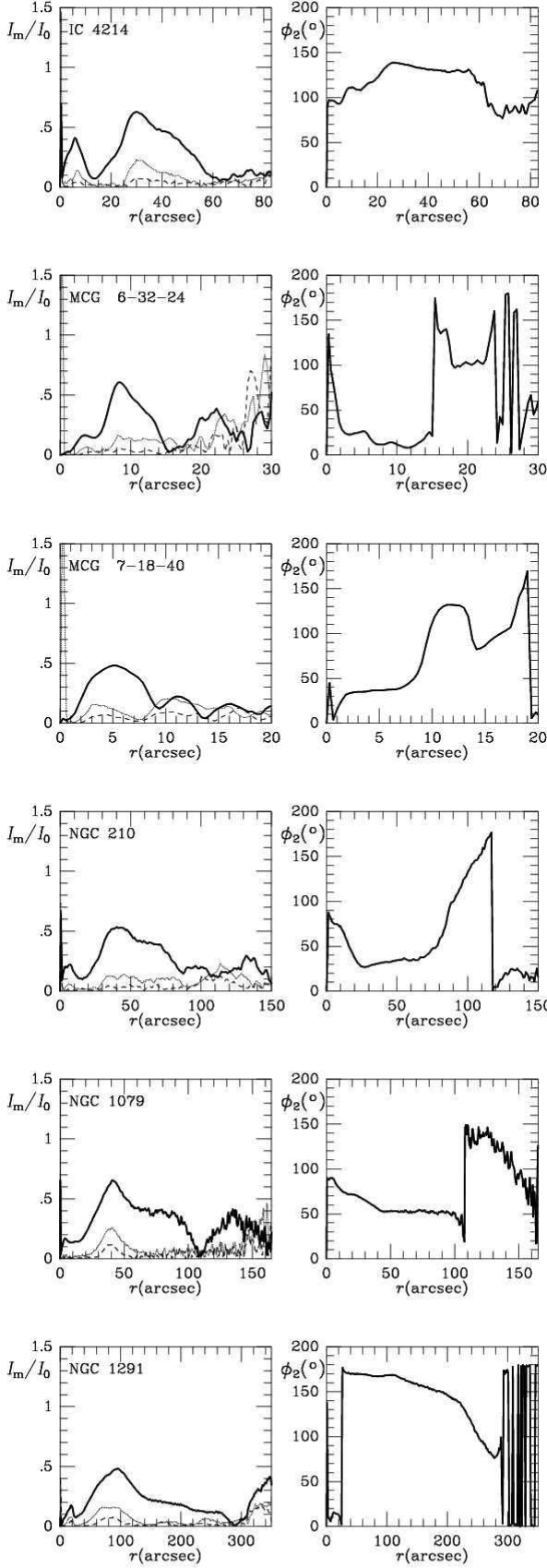


Figure 22. (cont.)

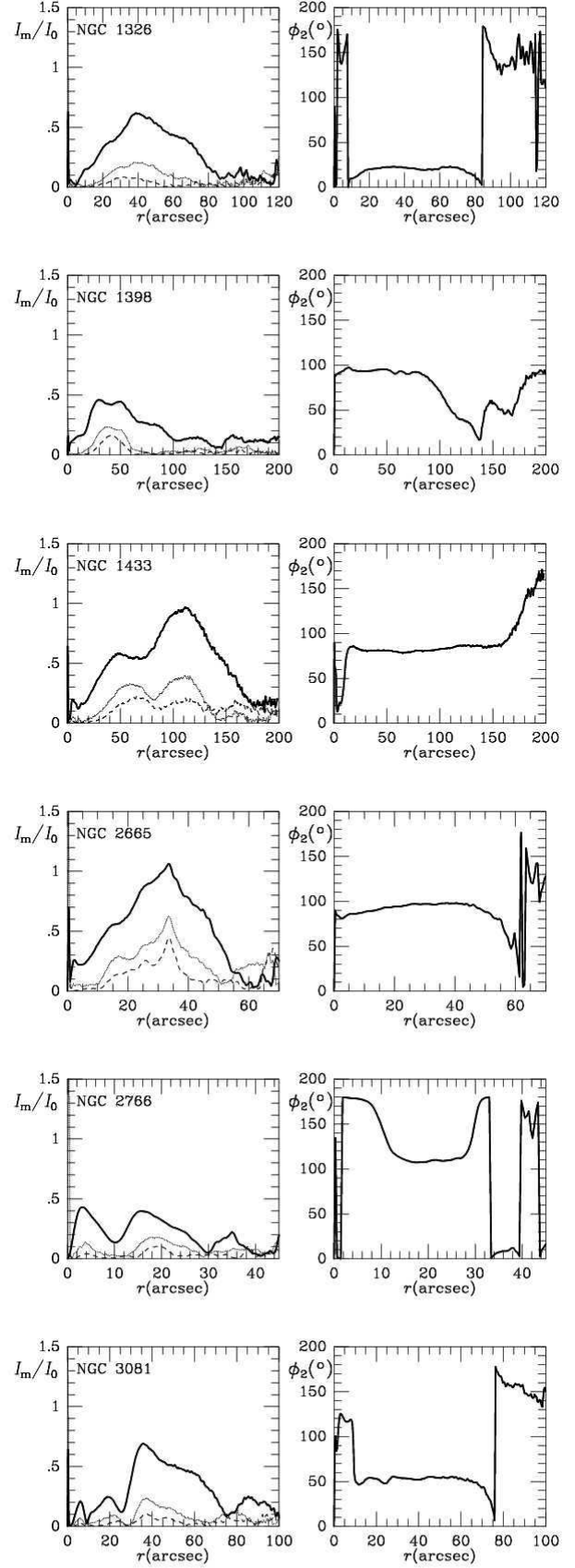


Figure 22. (cont.)

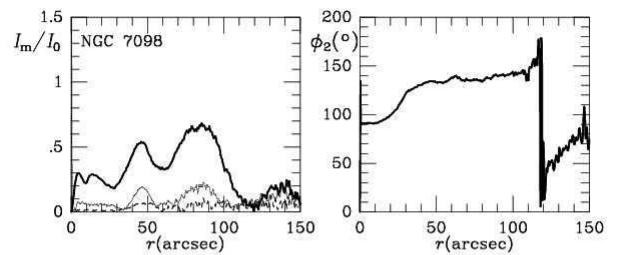
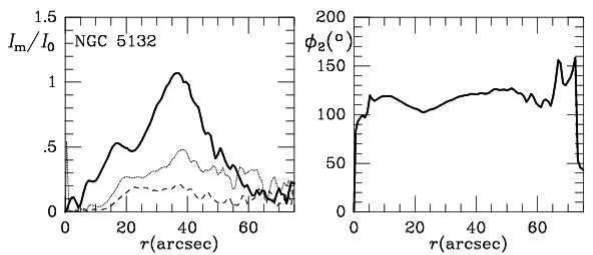
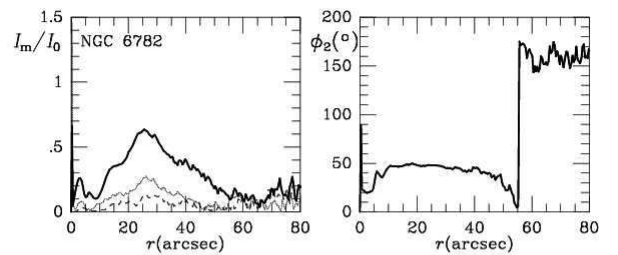
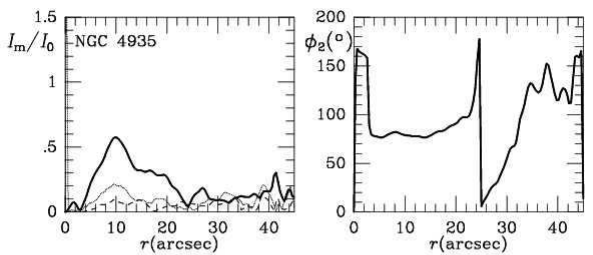
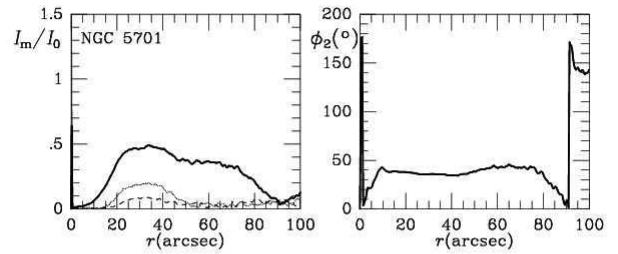
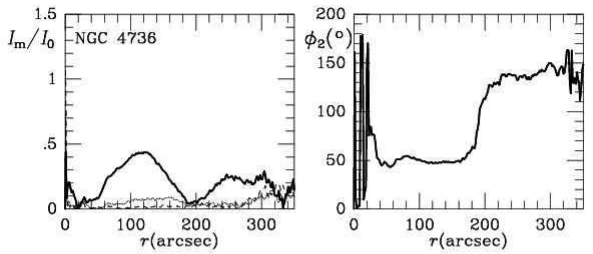
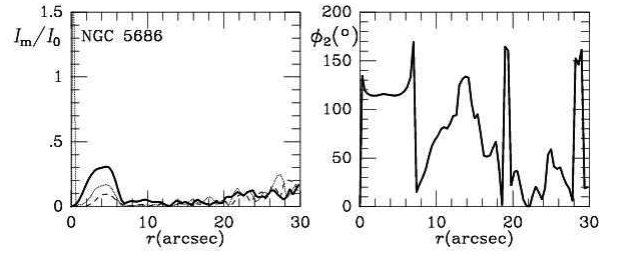
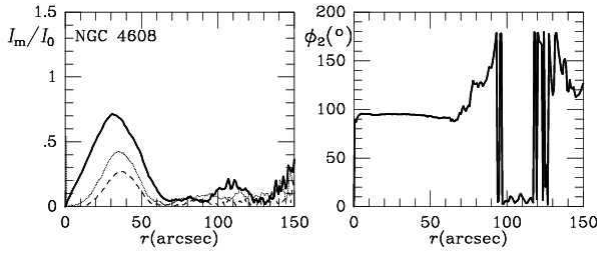
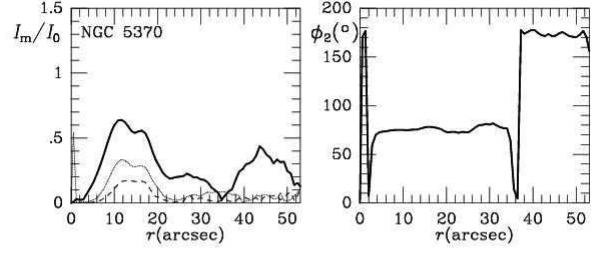
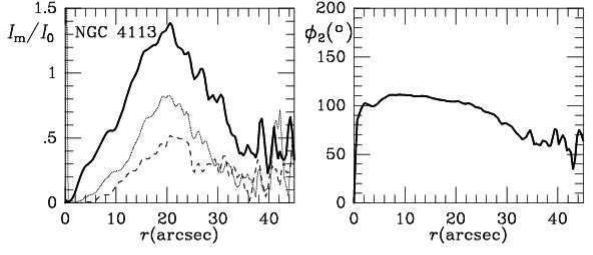
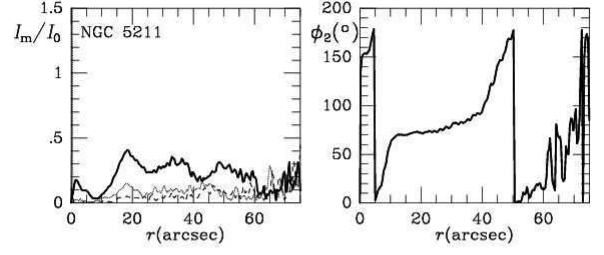
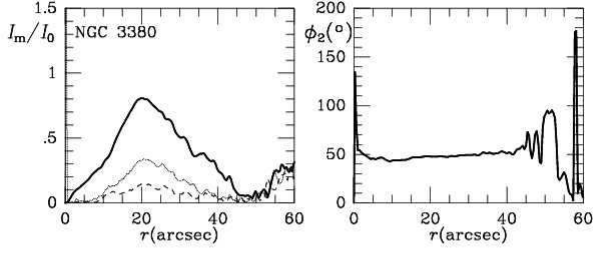


Figure 22. (cont.)

Figure 22. (cont.)

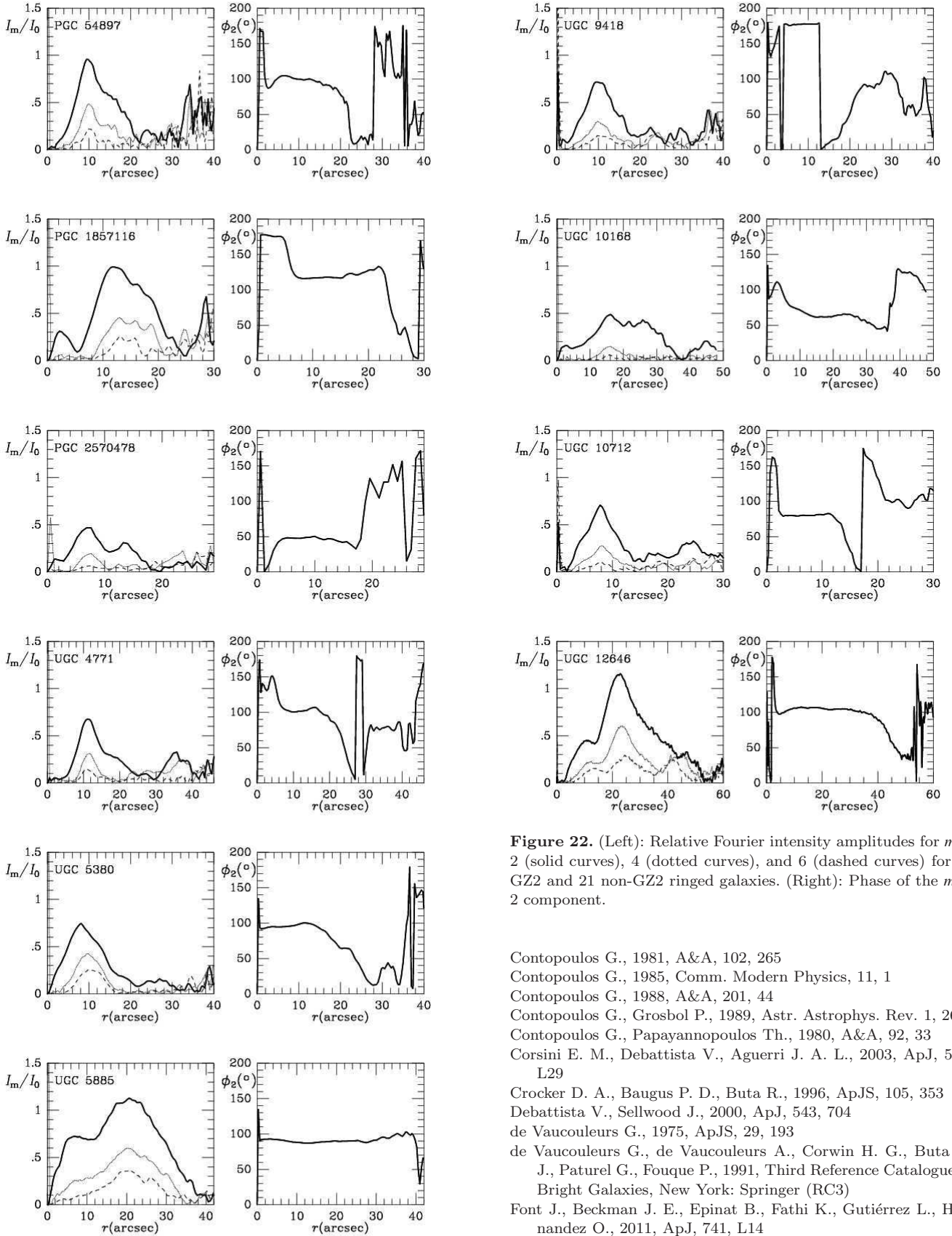


Figure 22. (cont.)

**Figure 22.** (Left): Relative Fourier intensity amplitudes for  $m = 2$  (solid curves), 4 (dotted curves), and 6 (dashed curves) for 31 GZ2 and 21 non-GZ2 ringed galaxies. (Right): Phase of the  $m = 2$  component.

- Contopoulos G., 1981, A&A, 102, 265  
 Contopoulos G., 1985, Comm. Modern Physics, 11, 1  
 Contopoulos G., 1988, A&A, 201, 44  
 Contopoulos G., Grosbol P., 1989, Astr. Astrophys. Rev. 1, 261  
 Contopoulos G., Papayannopoulos Th., 1980, A&A, 92, 33  
 Corsini E. M., Debattista V., Aguerri J. A. L., 2003, ApJ, 599, L29  
 Crocker D. A., Baugus P. D., Buta R., 1996, ApJS, 105, 353  
 Debattista V., Sellwood J., 2000, ApJ, 543, 704  
 de Vaucouleurs G., 1975, ApJS, 29, 193  
 de Vaucouleurs G., de Vaucouleurs A., Corwin H. G., Buta R. J., Paturel G., Fouque P., 1991, Third Reference Catalogue of Bright Galaxies, New York: Springer (RC3)  
 Font J., Beckman J. E., Epinat B., Fathi K., Gutiérrez L., Hernandez O., 2011, ApJ, 741, L14  
 Font J., Beckman J. E., Querejeta M., Epinat B., James P. A., Blasco-Herrera J., Erroz-Ferrer S., Pérez I., 2014, ApJS, 210, 2

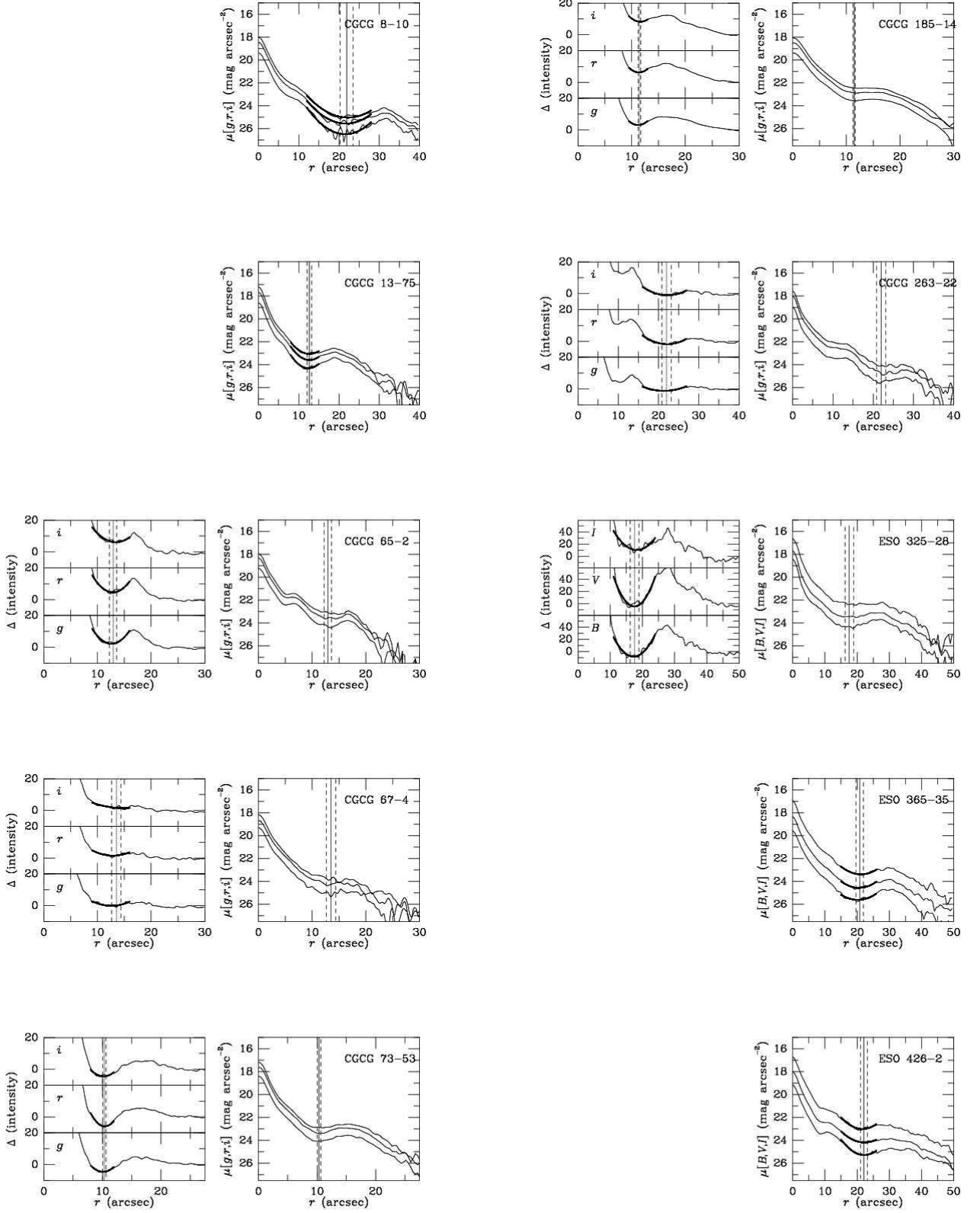


Figure 23.

Figure 23. (cont.)



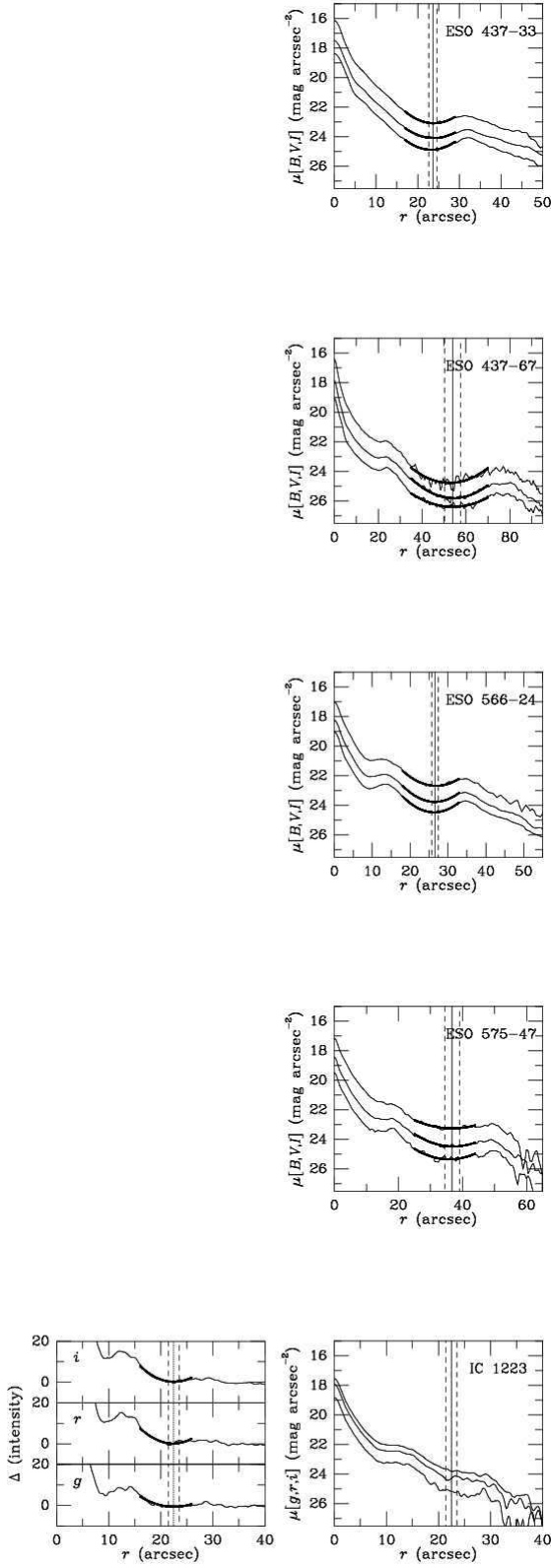


Figure 23. (cont.)

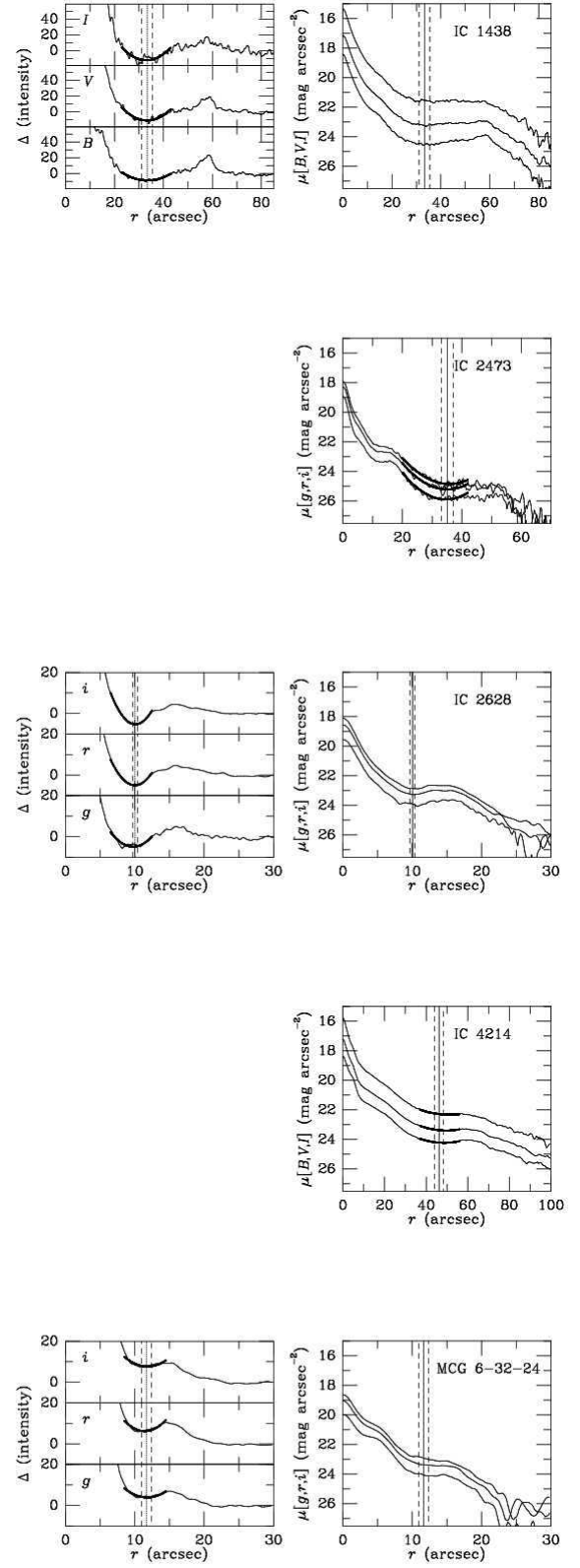


Figure 23. (cont.)

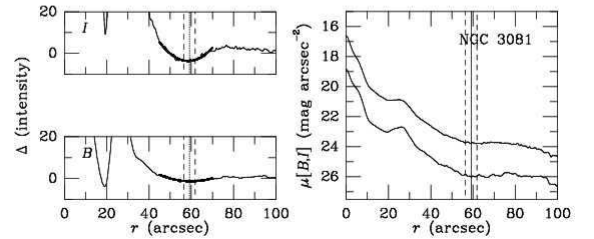
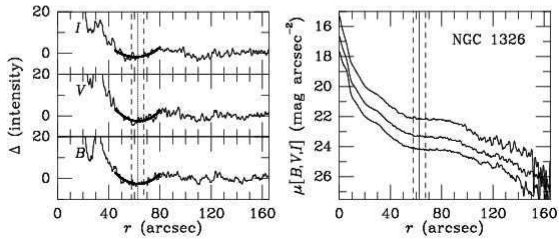
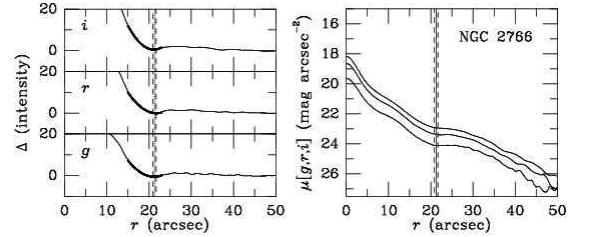
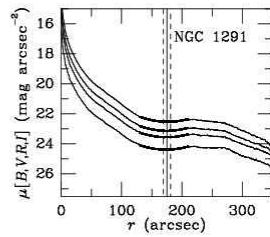
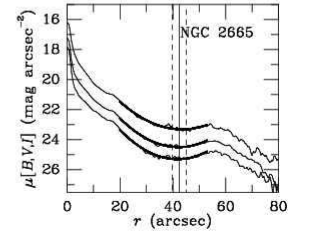
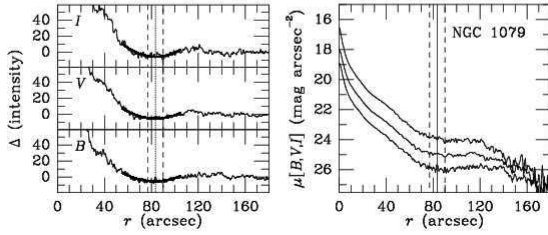
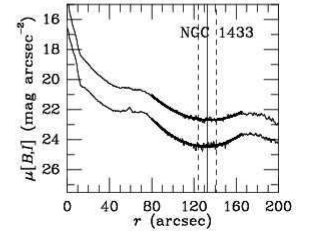
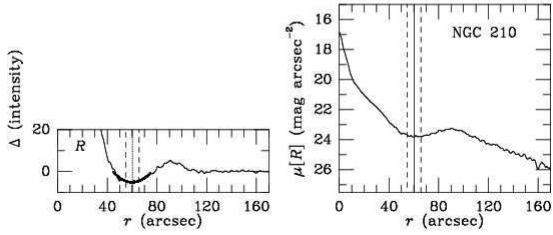
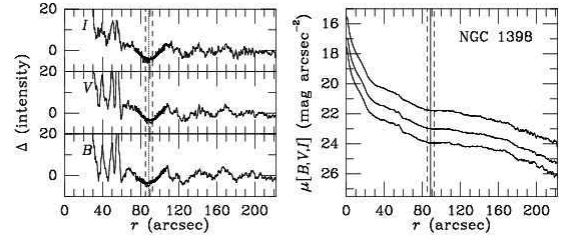
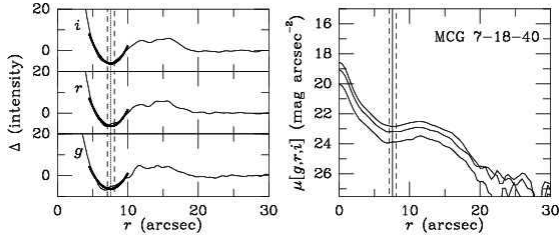


Figure 23. (cont.)

Figure 23. (cont.)

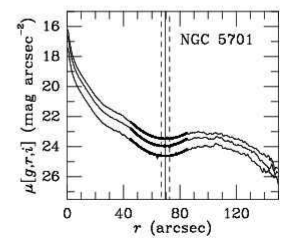
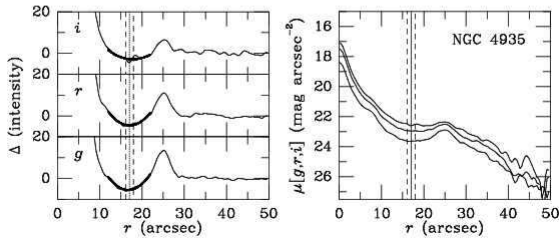
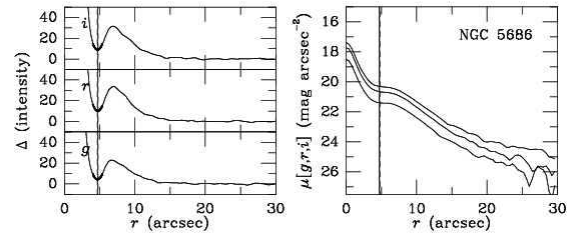
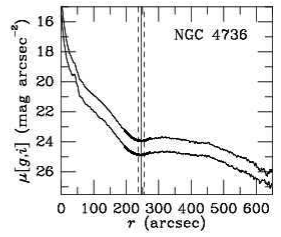
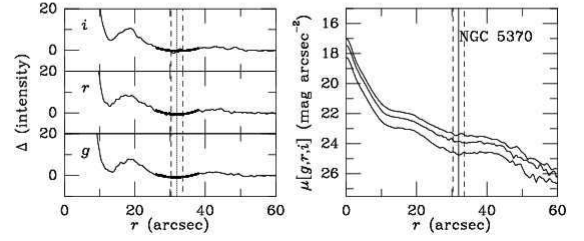
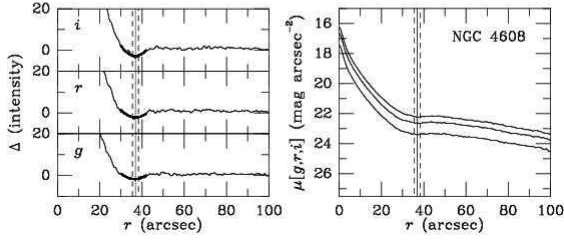
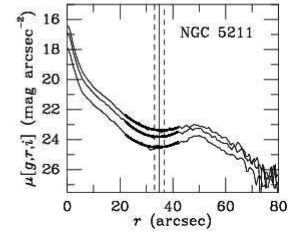
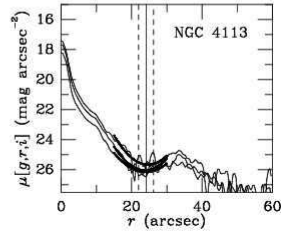
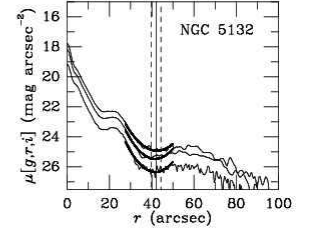
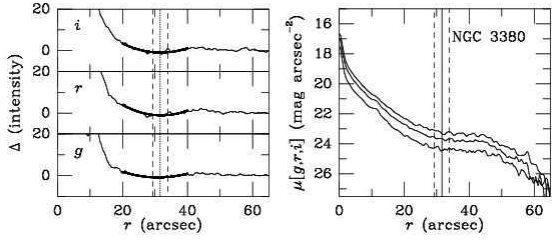


Figure 23. (cont.)

Figure 23. (cont.)

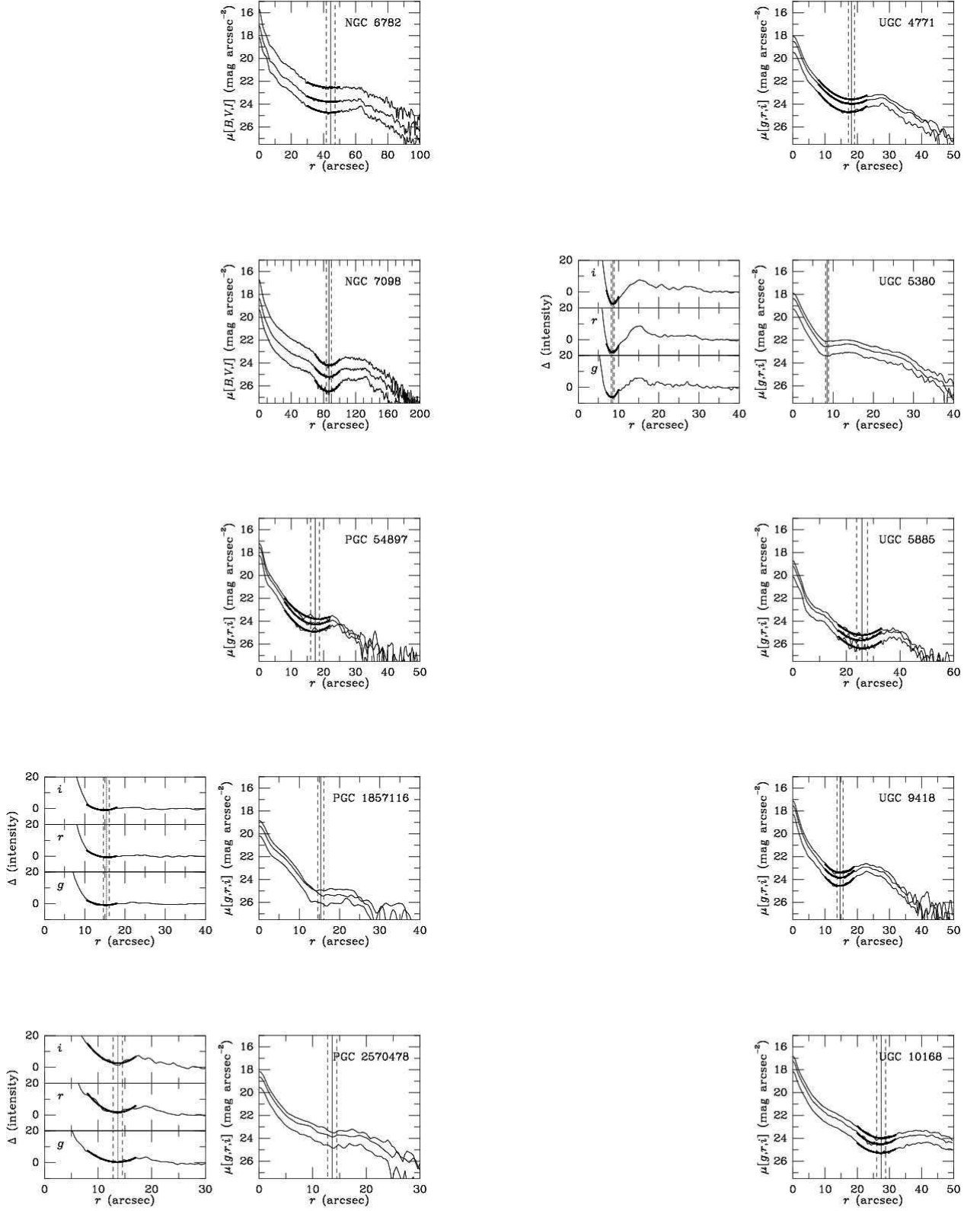
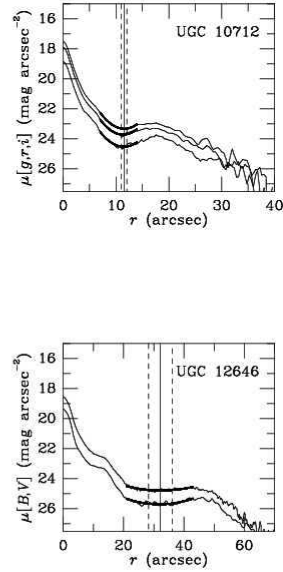


Figure 23. (cont.)

Figure 23. (cont.)





**Figure 23.** The derivation of  $r_{gp}$  for each sample galaxy. Those cases where  $r_{gp}$  is based on parabolic fits to residual intensities  $\Delta$  (as for CGCG 65-2) include up to three plots in a left panel with a darker line showing the fits. In these cases, the right panel shows the bar minor axis profiles and the vertical lines indicate the mean value of  $r_{gp}$  from the three filters and its estimated uncertainty. Those cases where  $r_{gp}$  is instead derived from parabolic fits to the surface brightness ( $\mu$ ) profiles (as for UGC 4596 and NGC 5335 in section 5) have only a single panel with a darker line showing the fits and vertical lines showing  $\langle r_{gp} \rangle$  and its estimated uncertainty.

Gadotti D., de Souza R. E., 2003, *ApJ*, 583, L75  
 Grouchy R. D., Buta R. J., Salo H., Laurikainen E., 2010, *AJ*, 139, 2465  
 Gunn J.E., Carr M., Rockosi C. et al., 1998, *AJ*, 116, 3040  
 Kennicutt R. C., Tamblin P., Congdon C. W., 1994, *ApJ*, 435, 22  
 Kim T., Gadotti D., Athanassoula E., Bosma A., Sheth K., Lee M. G., 2016, *MNRAS*, 462, 3430  
 Knapen J. H., 2010, in *Galaxies and Their Masks*, D. L. Block, K. C. Freeman, & I. Puerari, eds., New York, Springer, p. 201  
 Kormendy J., 1979, *ApJ*, 227, 714  
 Kormendy J., 2012, in *Secular Evolution of Galaxies*, J. Falcón-Barroso & J. H. Knapen, eds., Cambridge, Cambridge University Press, p. 1  
 Laurikainen E., Salo H., Buta R., Knapen J. H., 2011, *MNRAS*, 418, 1452  
 Laurikainen E., Salo H., Athanassoula E., Bosma A., Buta R., Janz J., 2013, *MNRAS*, 430, 3489  
 Lin C. C., 1970, *IAUS*, 38, 377  
 Lin C. C., Shu F. H., 1964, *ApJ*, 140, 646  
 Lin C. C., Yuan C., Shu, F., 1969, *ApJ*, 155, 721  
 Lin L.-H., Yuan C., Buta R., 2008, *ApJ*, 684, 1048  
 Lindblad B., 1941, *Stockholm Observatory Annals*, 13, 10  
 Lindblad B., 1955, *Stockholm Observatory Annals*, 18, 6  
 Lindblad B., Lindblad P. O., 1958, *IAUS*, 5, 8  
 Lindblad P. O., 1960, *Stockholm Observatory Annals*, 21, 4  
 Lintott C. et al., 2008, *MNRAS*, 389, 1179  
 Nair P. B., Abraham R. G. 2010, *ApJS*, 186, 427  
 Pfenniger D., 1990, *A&A*, 230, 55  
 Pfenniger D., Norman C., 1990, *ApJ*, 363, 391

Rautiainen P., Salo H., 2000, *A&A*, 362, 465  
 Rautiainen P., Salo H., Buta R., 2004, *MNRAS*, 349, 933  
 Rautiainen P., Salo H., Laurikainen E., 2008, *MNRAS*, 388, 1803  
 Romero-Gómez M., 2012, *A&AT*, 27, 303  
 Romero-Gómez M., Masdemont J. J., Athanassoula E., García-Gómez C., 2006, *A&A*, 453, 39  
 Romero-Gómez M., Athanassoula E., Masdemont J. J., García-Gómez C., 2007, *A&A*, 472, 63  
 Salo H., Rautiainen P., Buta R., Purcell G. B., Cobb M. L., Crocker D. A., Laurikainen E., 1999, *AJ*, 117, 792  
 Schlafly E. F., Finkbeiner D. P., 2011, *ApJ*, 737, 103  
 Schommer R. A., Sullivan W. T., 1976, *ApL*, 17, 191  
 Schwarz M. P., 1981, *ApJ*, 247, 77  
 Schwarz M. P., 1984a, *MNRAS*, 209, 93  
 Schwarz M. P., 1984b, *PASAu*, 5, 464  
 Sellwood J. A., Sparke L. S., 1988, *MNRAS*, 231, 25  
 Sheth K. et al., 2010, *PASP*, 122, 1397  
 Shimasaku K. et al., 2001, *AJ*, 122, 1238  
 Simkin S. M., Su H. J., Schwarz M. P., 1980, *ApJ*, 237, 404  
 Stoughton, C., et al., 2002, *AJ*, 123, 485  
 Tremaine S., Weinberg M., 1984, *ApJ*, 282, L5  
 Treuthardt P., Salo H., Rautiainen P., Buta R., 2008, *AJ*, 136, 300  
 Treuthardt P., Seigar M., Sierra A., Al-Baidhany I., Salo H., Kennefick D., Kennefick J., Lacy, C., 2012, *MNRAS*, 423, 3118  
 Willett K. et al., 2013, *MNRAS*, 435, 2835  
 York D.G., Adelman J., Anderson J.E. et al., 2000, *AJ*, 120, 1579  
 Zhang X., Buta R., 2007, *AJ*, 133, 2584